

Copyright  
by  
Eva Noyola  
2006

The Dissertation Committee for Eva Noyola  
certifies that this is the approved version of the following dissertation:

## Central Dynamics of Globular Clusters

Committee:

---

Karl Gebhardt, Supervisor

---

Shardha Jogee

---

John Kormendy

---

Paul Shapiro

---

Donald Winget

---

Tim de Zeeuw

**Central Dynamics of Globular Clusters**

by

**Eva Noyola, Física**

**DISSERTATION**

Presented to the Faculty of the Graduate School of  
The University of Texas at Austin  
in Partial Fulfillment  
of the Requirements  
for the Degree of

**DOCTOR OF PHILOSOPHY**

THE UNIVERSITY OF TEXAS AT AUSTIN

December 2006

To my parents, the best educators

## Acknowledgments

I would like to acknowledge the vast generosity and patience of my advisor, Dr. Karl Gebhardt. Thank you for showing me the entrance to the dynamical road. I also want to thank all members of my committee: Dr. John Kormendy, for his fantastic classes and the many valuable pieces of advice he gave me through the years. Dr. Paul Shapiro, for bringing me to Texas on the first place. Dr. Don Winget, for bringing the very needed external views. Dr. Shardha Jogee, for always keeping tabs on me. Dr. Tim de Zeeuw, for being a very generous collaborator and the facilitator of many fun times. Dr. Greg Shields, for being so generous as to serve in my committee during the first few years and then kindly opening a seat on it. Finally, I want to thank Dr. Marcel Bergmann for being a fun and helpful collaborator for part of my work.

This thesis is dedicated to my parents Martha and Antonio, they have always been very enthusiastic sponsors of my education, even when it took me far from their fields of knowledge and far away from them. Together with my wise brother Julio, they form a wonderful, supportive, geographically scattered family. I love you very much. My family in Austin is complete with Niv, my very loving and kind partner in life. His support has been a key ingredient for the completion of this program. Thank you my love.

I want to thank the huge amount of fun and knowledge that I got from all the astronomy department folks. First of all, to Claudia, my acquired astronomy sister. It has been great sharing the happiness and the tears with

you. Thanks to all my classmates, it has been a privilege to share this years with such a wonderful set of people. Thanks to my teachers (inside and outside the classrooms). And finally, thanks to all those individuals with whom I have shared all those beer afternoons, dinners, movies, concerts, parties and every other occasion that allowed me to vent and go on doing astronomy.

# Central Dynamics of Globular Clusters

Publication No. \_\_\_\_\_

Eva Noyola, Ph.D.

The University of Texas at Austin, 2006

Supervisor: Karl Gebhardt

This dissertation explores some aspects of the central dynamics of globular clusters. Surface brightness profiles are measured with a newly developed technique that yields accurate, high resolution density profiles. The technique uses integrated light measured with a robust statistical estimator, and it is applied to images obtained by the *Hubble Space Telescope*. Surface brightness profiles are presented for 39 globular clusters belonging to the Milky Way, 21 to the LMC, 5 to the SMC and 4 to the Fornax dwarf galaxy. Results show that the central structure of some globular clusters departs from the predictions made by classic dynamical models. When the distribution of central logarithmic slopes is analyzed, instead of finding a bimodal distribution between flat cores and steep cusps (as expected for post core-collapse clusters), a continuous distribution of central slopes is observed. A new sub-class of objects is found that have intermediate slopes between flat cores and the expected post-core collapse central slope. In total, 45% of the sample is not consistent with having King-type profiles in the center. Omega Centauri, the largest Galactic globular cluster, is one of the objects that deviates from a flat

core, having a central logarithmic slope clearly different than zero. In order to further explore the dynamical state of this cluster, central kinematic measurements are obtained. Spectroscopic measurements come from the GMOS-IFU on the Gemini-south telescope. Line-of-sight velocity dispersions from integrated spectra are measured in an area of  $5 \times 5$  arcseconds around the center and also 14 arcseconds away. A clear rise in dispersion from  $18.5$  to  $23 \text{ km s}^{-1}$  is observed between the outer and the central fields. The observed velocity dispersion profile is compared with dynamical models containing central black holes of various masses. Observations are best explained by the presence of an intermediate-mass black hole of  $4 \times 10^4 M_{\odot}$  at the center. It is crucial to investigate the central regions of globular clusters in great detail in order to find the causes for the observed photometric and kinematic peculiarities.



# Table of Contents

<b>Acknowledgments</b>	<b>v</b>
<b>Abstract</b>	<b>vii</b>
<b>List of Tables</b>	<b>xii</b>
<b>List of Figures</b>	<b>xiii</b>
<b>Chapter 1. Introduction</b>	<b>1</b>
1.1 History . . . . .	2
1.2 Dynamical Evolution . . . . .	3
1.3 Black holes . . . . .	9
1.4 Outline . . . . .	12
<b>Chapter 2. Surface Brightness Profiles for a sample of Galactic                 globular clusters</b>	<b>13</b>
2.1 Introduction . . . . .	13
2.1.1 Non-parametric Models . . . . .	16
2.2 Simulations . . . . .	17
2.2.1 Image Construction . . . . .	18
2.2.2 Center Determination . . . . .	19
2.2.3 Surface Brightness Profile . . . . .	20
2.2.4 Uncertainties in the Simulations . . . . .	31
2.3 Data acquisition and analysis . . . . .	32
2.3.1 Sample . . . . .	32
2.3.2 Image Processing . . . . .	34
2.3.3 Cluster Center Determination . . . . .	35
2.3.4 Surface Brightness Profiles . . . . .	36
2.3.5 Uncertainties for the Data . . . . .	43

2.4	Results and Discussion . . . . .	45
2.4.1	Surface Brightness and Luminosity Density Profiles . . .	45
2.4.2	Slopes Distribution and Correlations . . . . .	54
2.4.3	Individual objects . . . . .	62
2.4.3.1	NGC 6397 . . . . .	62
2.4.3.2	NGC 6535 . . . . .	62
2.4.3.3	NGC 6652 . . . . .	63
2.4.3.4	NGC 6752 . . . . .	63
2.4.3.5	M15 . . . . .	63
2.5	Summary . . . . .	66

**Chapter 3. Surface brightness Profiles for a sample of LMC, SMC and Fornax Dwarf galaxy Globular Clusters 72**

3.1	Introduction . . . . .	72
3.2	Simulations . . . . .	75
3.2.1	Image Construction . . . . .	75
3.2.2	Center Determination . . . . .	77
3.2.3	Surface Brightness Profiles . . . . .	77
3.2.4	Uncertainties . . . . .	84
3.3	Data and Analysis . . . . .	86
3.3.1	Sample . . . . .	86
3.3.2	Image Processing . . . . .	88
3.3.3	Center . . . . .	89
3.3.4	Surface Brightness Profiles . . . . .	89
3.3.5	Data Uncertainties . . . . .	93
3.4	Results and Discussion . . . . .	94
3.4.1	Surface Brightness . . . . .	94
3.4.2	R136 . . . . .	101
3.4.3	Combining Two Samples . . . . .	103
3.5	Summary . . . . .	106

<b>Chapter 4. Possible Intermediate Mass Black Hole in Omega Centauri</b>	<b>113</b>
4.1 Introduction . . . . .	113
4.2 Surface Brightness Profile . . . . .	115
4.3 Kinematic Measurements . . . . .	118
4.4 Models . . . . .	125
4.5 Discussion . . . . .	129
4.6 Summary . . . . .	132
<b>Chapter 5. Discussion and Conclusions</b>	<b>133</b>
5.1 Core-collapse . . . . .	133
5.2 Black Holes . . . . .	136
5.3 Stability . . . . .	138
5.4 Rotation . . . . .	139
5.5 Individual objects . . . . .	140
5.5.1 G1 . . . . .	140
5.5.2 M15 . . . . .	141
5.5.3 NGC 6752 . . . . .	142
5.6 Discussion and Summary . . . . .	143
<b>Bibliography</b>	<b>148</b>
<b>Vita</b>	<b>156</b>

## List of Tables

2.1	Milky Way Sample. . . . .	67
2.1	Milky Way Sample. . . . .	68
2.2	Measured parameters . . . . .	69
2.2	Measured parameters . . . . .	70
2.2	Measured parameters . . . . .	71
3.1	Simulations input. . . . .	108
3.2	LMC, SMC and Fornax Sample. . . . .	109
3.2	LMC, SMC and Fornax Sample. . . . .	110
3.3	Results . . . . .	111
3.3	Results . . . . .	112

## List of Figures

2.1	Center determination results for simulated datasets . . . . .	21
2.2	Surface brightness results for simulated datasets . . . . .	25
2.3	Second set of surface brightness results for simulated datasets	26
2.4	Input vs. measured slope for simulated datasets . . . . .	29
2.5	Surface brightness profiles for M54. Comparison of ground-based vs. space-based results . . . . .	38
2.6	Surface brightness profiles for M80. Comparison of profiles obtained from different filters . . . . .	40
2.7	Surface brightness profiles for the entire sample . . . . .	47
2.8	SB results continued . . . . .	48
2.9	SB results continued . . . . .	49
2.10	SB results continued . . . . .	50
2.11	SB results continued . . . . .	51
2.12	Comparison of King fits vs. smooth fits . . . . .	52
2.13	histogram of SB logarithmic central slopes . . . . .	55
2.14	Histogram of LD logarithmic central slopes . . . . .	56
2.15	SB central slopes vs. various physical quantities . . . . .	59
2.16	LD slopes vs. various physical quantities . . . . .	60
2.17	Normalized SB profiles for the entire sample . . . . .	61
2.18	Surface brightness profiles for the central region of M15 . . . .	65
3.1	Center measurement results for the simulated datasets . . . .	78
3.2	Surface brightness results for simulated dataset . . . . .	82
3.3	More SB results for simulated datasets . . . . .	83
3.4	Input vs. measured central slopes for the simulated datasets .	85
3.5	SB profiles for the LMC globular clusters . . . . .	96
3.6	SB for LMC continued . . . . .	97
3.7	SB for LMC continued . . . . .	98

3.8	SB profiles for SMC globular clusters . . . . .	99
3.9	SB profiles for the Fornax dwarf galaxy globular clusters . . .	100
3.10	Histograms of central logarithmic SB and LF slopes . . . . .	102
3.11	Various physical quantities plotted against each other . . . . .	104
4.1	Surface brightness profiles for $\omega$ Centauri . . . . .	117
4.2	Central field observed with ACS and GMOS . . . . .	122
4.3	Same as fig 2 for the field 14'' away. . . . .	123
4.4	Line of sight velocity dispersion profile plotted against various dynamical models . . . . .	127
4.5	$\chi^2$ vs. black hole mass . . . . .	128
4.6	Black hole mass vs. velocity dispersion . . . . .	131

# Chapter 1

## Introduction

Globular clusters orbiting the the Milky Way galaxy are old, nearly spherical stellar systems that populate the Galactic halo. They appear to have been formed on a single burst of star formation at the time when the first structures appeared in the universe. The distribution of globular clusters around the galaxy is spherical and concentrated toward the galactic center. The masses of globular clusters range three orders of magnitude from  $10^3$  to  $10^6 M_{\odot}$ . Most of the globular clusters orbiting the Milky Way are older than 10 Gyr, but clusters as young as 3 Myr are known to exist orbiting other galaxies in the local group. The fact that they are numerous ( $\sim 150$  in our Galaxy) and nearby (few kpc) self-gravitating stellar systems makes them unique objects for the study of stellar dynamics since we can, in principle, follow the motions of each individual star and compare it to predictions by dynamical models.

There are fundamental connections between globular clusters and their host galaxies. It is thought that globular clusters are among the first structures to have been formed in the universe and that they are part of the building blocks of the galaxies we see today, particularly of the central bulge and the halo. The study of the globular cluster systems around different galaxies has provided important constraints for galaxy assembly models. It is crucial to understand their dynamical evolution in the context of interactions with their host galaxy since this can provide further knowledge about how mass has

assembled through the history of the universe. What we learn about globular clusters has generic implications for structure formation.

This dissertation presents surface brightness profiles for 69 globular clusters orbiting around our galaxy, the large Magellanic cloud, the small Magellanic cloud and the Fornax dwarf galaxy; as well as kinematic measurements for the globular cluster  $\omega$  Centauri. A brief historic review and a summary of classic results in dynamics of star clusters are presented in this chapter.

## 1.1 History

The famous catalog by Charles Messier (Messier, 1784), which contains the first systematic search for ‘nebulous’ celestial objects, contains 28 Galactic globular clusters that are visible from the northern hemisphere. William Herschel (Herschel, 1814) was the first person to identify these objects as large groups of stars. The first star counts for the two richest Galactic globular clusters,  $\omega$  Cen and 47 Tuc, were done from photographic plates in the 19th century Pickering et al. (1898). At the beginning of the 20th century, studies tried to estimate the density distribution of stars from the observed projected profile, while the important developments in the field of kinetic theory for gases had an impact on the theoretical study of small stellar systems. Jeans (1913) remarked the importance of stellar collisions in clusters, and Plummer (1915) tried to find the physical basis behind the stellar distribution inside these systems. Eddington (1916) combined the most detailed observations at the time in order to explore the theoretical basis for the observed stellar distributions. During the late 1930s and 1940s, fundamental theoretical studies were carried out by Ambartsumian (1938), Spitzer (1940) and Chandrasekhar (1942), who investigated the effect of stellar encounters in dense star clusters.



By the late 1950s and 1960s, more efficient contact between improved observational work and more sophisticated theoretical studies was established. M3 and  $\omega$  Cen, in particular, were the subjects of detailed studies combining improved observations and theoretical models (Oort & van Herk, 1959; Dickens & Woolley, 1967). King and Michie produced a burst of papers (some of which will be discussed in detail below) during this time that are still today the basis of many dynamical studies for globular clusters. It was at this time that the first N-body calculations with  $N=16$  stars started to be carried out (von Hoerner, 1960). Even with such a small number of particles, the N-body simulations already gave some important results like evaporation timescales and confirmation of analytical formulas for the relaxation time. This seminal work also helped to establish the fact that the evolution of N-body systems can be studied with a statistical approach, saving a lot on computing time. During that time, the fundamentals of dynamical theory and observations for globular clusters were established. Many of the results and techniques established during that time are being used nowadays.

## 1.2 Dynamical Evolution

Globular clusters are among the most dense stellar systems in the universe, this produces a large number of close gravitational encounters between its members stars. The timescale on which these close encounters affect the structure of the system is known as the relaxation time (discussed in detail below). The estimated relaxation times for many globular clusters are shorter than their estimated ages, which implies that interesting dynamical processes have occurred and can be studied in these systems. There are a number of issues under study today that affect dynamical evolution, like the nature of the

initial mass function as well as its dependence on metallicity, the way stellar evolution affects dynamical processes, and the content and dynamical effects of primordial binaries. Globular cluster dynamics is a field of astronomy that continues to be relevant through time.

The earliest dynamical effects in star clusters come from stellar evolution. There are various formation models for globular clusters, which are not discussed here, but independently of the way a cluster is originally assembled, once it is formed, the first important dynamical effect will occur when the most massive stars evolve away from the main sequence, they rapidly lose mass, which results in expansion of the cluster. Chernoff & Weinberg (1990) and Fukushige & Heggie (1995) model the evolution of clusters during this rapid mass loss period. They find that clusters with a flat mass function ( $\alpha < 1.5$ ; for  $dN/dM \propto m^{-\alpha}$ ) are destroyed during this process, while clusters with steeper mass functions can survive if they have a large initial concentration. Formation models suggest that the gaseous clouds from which globular clusters form have to be about two orders of magnitude more massive than the currently observed clusters in order for them to survive the evaporation process caused by stellar evolution and collisions with other clouds (Searle & Zinn, 1978). During this rapid mass loss period, there are important changes in the gravitational potential of the clusters, the orbits of stars change on a timescale of the order of the crossing time. This period is related to ‘violent relaxation’ (Lynden-Bell, 1962; Hénon, 1964).

The period after violent relaxation leads to a smooth mass distribution which is governed by dynamical relaxation due to weak gravitational interactions between stars. The interactions are small-angle deflections produced by the gravitational pull of nearby stars. The relevant timescale for this part of

the evolution is known as the ‘relaxation time’; it can be thought of as the amount of time it takes weak gravitational interactions to remove the history of a star’s original velocity. The relaxation time is estimated as

$$t_{rel} \simeq \frac{N}{8 \ln N} \frac{R}{v} ,$$

(Binney & Tremaine, 1987) where  $N$  is the number of stars,  $R$  is the size of the region and  $v$  is the average velocity of a star. Evidently, this quantity depends on the local density and velocity, so it is different for different radii. A global estimate of the relaxation time is the half-mass relaxation time, which is calculated as

$$t_{rh} = 0.138 \frac{M^{1/2} R_h^{3/2}}{\langle m \rangle G^{1/2} \ln N} ,$$

(Spitzer, 1987) where  $M$  is the total mass of the cluster,  $R_h$  is the half-mass radius,  $\langle m \rangle$  is the average stellar mass, and  $G$  is the gravitational constant. A globular cluster containing  $10^5$  stars has a global relaxation time of  $\sim 10^{10}$  yr, but if the relaxation time is calculated for the central density and velocity dispersion, it is considerably shorter. For this reason, the relaxation process is particularly important for the central regions of star clusters. A direct consequence of relaxation is kinetic energy equipartition, which affects stars of different masses in a different way. Heavier stars tend to lose kinetic energy and sink to the center, while lighter stars gain kinetic energy and go to the outskirts of the cluster. This process is known as ‘mass segregation’. Star clusters are expected to reach equipartition in the core much more quickly than in the outskirts.

Relaxed clusters are described by single-mass King models (King, 1966). These models describe a distribution of stars in which the central regions are isothermal and the outer regions are tidally truncated by the galaxy. King models provide an important theoretical base for the study of globular clusters. The family of models are described by three parameters: a central density, a radial scale, and a concentration. Single-mass King models are unable to fit the entire radial density distribution of some clusters; therefore a more sophisticated description known as King-Michie models has been developed. These models include multiple masses, a certain degree of anisotropy, and a more extended tidal radius.

Every gravitationally bound system has a negative heat capacity, which has very important consequences for its dynamical evolution. The kinetic energy of a cluster of stars is written as  $K = 1/2(mv^2) = 3/2(Nk_B T)$  where  $T$  is the temperature, and  $k_B$  is the Boltzmann constant. The total energy of the cluster is given by  $E = W + K = -K$  (where  $W$  is the potential energy) due to the Virial theorem. The specific heat is defined as  $C_s = \partial E / \partial T$  which is equal to  $-3/2(Nk_B)$ , always a negative number. The fact that stellar clusters have a negative specific heat implies that when energy is taken out of their core, the clusters increase their temperature (i.e. the velocity dispersion increases), and inversely, when energy is injected into the core, it cools the system down. When this fact is put together with the process of relaxation, the consequence is that energy is driven from the core to the outer halo of the cluster. After many relaxation times, and due to the negative heat capacity of the system, an increase in central density and central velocity dispersion takes place while the core radius decreases. The continuation of this process implies that the center reaches an infinite density on a finite amount of time. This is known

as the ‘gravothermal catastrophe’ or core collapse. Core collapse occurs in a timescale of  $\sim 16t_{rel}$  for a cluster formed by stars of the same mass (Heggie, 1979). If stars of various masses are present, mass segregation occurs; this drives energy from the core to the outer halo faster than the relaxation process for a single-mass component cluster does. The energy exchange increases the velocity dispersion in the core while it makes it contract, so the timescale for core collapse to occur is shorter for a cluster with different masses than for a cluster with stars of the same mass.

A number of simulations have been carried out to provide a detailed description of core collapse using both N-body codes (Makino, 1996) and numerical integrations of the multi mass Fokker-Planck equation (Cohn, 1980; Murphy et al., 1990; Chernoff & Weinberg, 1990; Cohn et al., 1989). They all show that the projected radial density of the cluster will have a shallower central slope for the lower mass stars compared with the high mass stars. Cohn (1985) calculate the precise slope for each stellar mass. The logarithmic slope depends on the mass of the heavy remnants dominating the core in the following way

$$\beta = -1.89 \frac{m_1}{m_2} + 0.35$$

where  $m_1$  is the observed mass group and  $m_2$  is the heaviest mass group dominating the core population. This slope obviously depends on the assumed mass function, the stage of core-collapse, and the spatial resolution of the measurements. The fact that  $\sim 20\%$  of the Galactic globular cluster population show central cusps instead of the flat King-type core has been taken as observational evidence that core collapse has occurred in these clusters (Trager et al., 1995; Meylan & Heggie, 1997).

The presence of binary systems in the core of globular clusters has important effects on core collapse evolution. The presence of primordial binaries has the effect of delaying core collapse, but even if there are no primordial binaries present in the cluster core, hard binaries are formed by three body encounters once core collapse begins. These binaries act as an energy source for the core, cooling it, this in turn reverses the contraction process and produces an expansion. Once the binaries have been depleted by ejection or by merging, the core contracts again and the whole process happens periodically, which results in what is known as ‘gravothermal oscillations’. At this stage, the cluster successively goes in and out of core collapse. (Breedem et al., 1994) perform Fokker-Planck simulations containing binaries and show that core-collapse occurs on a very short time scale. The core quickly re-expands and spends a longer time in a state similar to pre-collapse between the successive contractions, but with a much smaller core with radius of a few percent the half-mass radius.

Measuring surface brightness profiles is a first step when trying to characterize stellar systems. SB profiles are also a key ingredient of dynamical models. Today, most surface brightness profiles come from ground based data and the input to dynamical models are parametric fits to the observations instead of the observed profiles themselves. These data needs to be updated in order to perform dynamical models and to study the central parts of globular clusters. This dissertations aims to obtain surface brightness profiles with high spatial resolution in order to test the validity of different dynamical models and to explore possible connections of the profile with physical quantities related to formation and location in the galaxy.

### 1.3 Black holes

Another dynamical scenario that has been explored as part of the evolution of globular clusters is the possible presence of a central black hole. Silk & Arons (1975) suggested that central X-ray sources in clusters could be produced by gas fed into a  $100\text{-}1000M_{\odot}$  black hole. These X-ray sources were later proved to be comprised of multiple fainter individual sources, but the original observation inspired a number of theoretical calculations of the possible effects of a black hole at the center of star clusters.

Bahcall & Wolf (1976, 1977) calculate the effect on the stellar distribution for a cluster if a black hole is present in its center. They solve numerically the coupled time-dependent Boltzmann equation for a system containing two different masses. They predict the formation of a cusp near the center with a logarithmic slope of about  $-1.75$  for the most massive stars in the 3-dimensional density, while the limiting slope for least massive stars is about  $-1.5$ . The predicted slope of the surface brightness distribution is very close to that predicted for core-collapse for the dominant stellar components in the core, but the variation with mass is less dramatic than for the core-collapse case. Most observable mass groups would have a projected logarithmic slope of  $-0.7$  (Sosin & King, 1997). Later calculations (Shapiro, 1977; Lin & Tremaine, 1980) explore the mass loss of a star cluster due to scattering from the central black hole. They find that a possible fate for the cluster is the total destruction due to ejection by close encounters and tight binaries forming in the cusp around the black hole. Yuan & Zhong (1990) find a limit mass for a black hole such that if it is smaller, the cluster expands until evaporation, but if it is larger, the core contracts and forms a cusp around it. The mass of the black hole depends on the initial conditions of the cluster.

One of the reasons for the difficulty of detecting a black hole has to do with the size of its sphere of influence, which is the region where the presence of the black hole will affect the stellar distribution. The radius of the sphere of influence of a black hole can be calculated as

$$r_{BH} = \frac{GM_{BH}}{\sigma^2}.$$

where  $M_{BH}$  is the mass of the black hole and  $\sigma$  is the velocity dispersion of the stars around the black hole. Then,  $r_{BH} \simeq 1''$  for a globular cluster at 10 kpc distance containing a black hole mass of  $\sim 1000M_{\odot}$  and having a velocity dispersion of  $10 \text{ km s}^{-1}$ . This type of scale cannot be resolved with ordinary ground-based telescopes, but with *HST* or adaptive optics assisted observations, it is possible to resolve individual stars inside the sphere of influence if the mass of the black hole is  $\sim 10^3M_{\odot}$  or larger.

Several authors have explored the possible formation channels for an intermediate mass black hole in a star cluster. A possible avenue of formation for such a black hole is a series of runaway collisions and mergers of young stars on a very dense environment (Gürkan et al., 2004). One necessary condition for this to happen is that the core-collapse time has to be shorter than the evolution timescales for the most massive stars to explode as supernovae. A large number of simulations with varying initial conditions are carried out to estimate which are the adequate circumstances for a central intermediate black hole to form. They find that a number of clusters with realistic initial conditions did end up forming a black hole by a runaway process. They also find that the mass of the black hole is  $\sim 10^{-3}$  times the total mass of the cluster for all realistic initial conditions. Another explored avenue for the formation of an intermediate mass black hole in a star cluster is the collision



and merging of stellar-mass black holes (Miller & Hamilton, 2002). Mouri & Taniguchi (2002) estimate that such merging has to occur in a runaway fashion since stellar-mass black holes present in the cluster will sink to the center due to mass segregation, and they will therefore have a larger density than other stars. If the stellar mass function in a cluster is very shallow, a third avenue of formation can occur, the accretion of gas by a stellar-mass black hole (Kawakatu & Umemura, 2004).

We know that supermassive black holes (SMBHs) are located at the center of some elliptical galaxies and bulges. It is still unknown how those black holes formed and grew to the sizes observed today. For any formation scenario, an intermediate mass black hole is needed as a seed to form supermassive black holes. If globular clusters contain intermediate mass black holes (IMBHs), they could be a crucial ingredient in finding the formation process of SMBH. They could also be important sources for gravitational wave detectors. Finally, if clusters contain IMBHs, these will have important effects in the dynamical evolution of the cluster, in particular for the central regions. It is important to find out if and which globular clusters contain IMBHs in them. If intermediate mass black holes are present in relatively high numbers, then it is easy to invoke merger process that could drive these black holes to the galactic centers. In the local universe, globular clusters are the best place to look for an IMBH. They have high central densities and are at the low mass end of isolated self gravitating systems. In this dissertation, we obtain kinematical measurements for the largest globular cluster in the galaxy in order to find out if there is a black hole present at its center.

## 1.4 Outline

During the last decade, improved instrumental capabilities like the *Hubble* and *Chandra* space telescopes and various 10-meter class telescopes have allowed the field of globular clusters dynamics to gain a new fresh look. The improved spatial resolution of space-based images, from visual to x-ray wavelengths, and the improved spectral resolution of large ground-based telescopes, have unveiled a whole set of new issues to investigate. The present work makes use of new technology in order to explore the central regions of globular clusters in the local group with the aim of better understanding the dynamical processes taking place there. In chapter 2, surface brightness profiles obtained measuring integrated light from *HST* images for a sample of 38 Galactic globular clusters are presented. Chapter 3 contains similar measurements for a sample of 30 clusters belonging to the LMC, SMC and Fornax dwarf galaxy. Chapter 4 presents photometric and kinematic measurements for  $\omega$  Centauri that suggest the presence of an intermediate mass black hole at the center of the cluster. Chapter 5 presents a discussion of the results in the context of recent results for globular cluster dynamics.

## Chapter 2

# Surface Brightness Profiles for a sample of Galactic globular clusters

*Lo que irradia esta noche es especial  
sobre el lago resplandece  
esperaba una tenue aparición  
nebulosa como siempre  
una crema de estrellas parece cubrirlo todo  
en mi constelación*

G. Cerati

### 2.1 Introduction

Globular clusters (GC) are nearby, isolated, and relaxed systems, which makes them good laboratories to study stellar dynamical processes. As a first step for any dynamical model, we require a measure of the surface brightness profile. Dynamical processes such as core-collapse, influence of a central black hole, and the physics of the initial collapse (Bahcall & Wolf, 1977; Cohn, 1980; Gnedin et al., 1999) will influence the central surface brightness profile, while tidal influences and evaporation leave noticeable effects at larger radius. The standard view is to assume that the central regions are isothermal and the outer regions are tidally truncated by the galaxy. King models (King, 1966; Meylan & Heggie, 1997) provide a theoretical base for their study. However,  $\sim 20\%$  of the galactic globular clusters show deviations from King models by

having steeper central surface brightness profiles (Djorgovski, 1995). These clusters have historically been called post-core collapse since this steeping of the central profile is the expected behavior during core-collapse (Cohn, 1980). Given the large amount of data collected from the *Hubble Space Telescope* (*HST*), our goal here is to characterize the central profile in a non-parametric way, thereby testing whether the cores are in fact isothermal or consistent with the expected post-core collapse morphology.

The surface brightness (SB) profile provides a fairly simple way to obtain the mass distribution through deprojection; therefore, reliable SB profiles of any stellar system are necessary for detailed dynamical modeling. In the case of globular clusters, most dynamical studies use parameters such as central surface brightness and half light radius obtained from King model fits to the observed SB. Trager et al. (1995) provide the most complete catalog for GC radial profiles. This catalog contains profiles constructed from ground-based images using a combination of star counts and integrated light; they also provide King model fits to determine core radius ( $r_c$ ), concentration ( $c = \log(r_t/r_c)$ ; where  $r_t$  is the tidal radius) and central surface brightness ( $\mu_0$ ). It is worth noting that the concentration is the only parameter they obtain directly from the King model fit; the other two parameters are obtained from a Chebychev polynomial fit to the photometric points. They report uncertainties from a variety of sources, some are relevant to the outer part of the profiles like sky brightness determination, while others are particularly important for the inner parts of the profile such as center determination and crowding correction for star counts. They report a seeing of  $2'' - 3''$  for the observations. While this catalog is extremely useful for analyzing the outer parts of the SB profile, it is necessary to update the data for the innermost regions using *HST*'s resolu-

tion. Another study using ground-based images in the  $U$  filter is performed by Lugger et al. (1995) on 15 core-collapse clusters. They fit pure power-law and modified power-law (which allows the existence of a core) to the central surface brightness of these objects. They find that nine have unresolved cores, three have marginally resolved cores, and three have clearly resolved cores. The average slope of the power-law fits is  $\sim -0.8$ . They conclude that clusters in their sample, with the exception of one object (NGC 6752), have cores consistent with expectations for a post-collapse bounce.

Some specific clusters have been studied in more detail. Particularly, M15 has been the subject of many studies trying to obtain a reliable radial profile (either in light or in star counts) near the center. Lauer et al. (1991), using WFPC, claimed to see a core of  $1.1''$ ; later analysis by Guhathakurta et al. (1996) using WFPC2 found a steep cusp into the smallest resolution element with a slope of  $-0.7$ . This result is similar to that of Sosin & King (1997) using FOC images. Our results agree with those of Guhathakurta et al. (1996), as discussed in Section. 2.4.3.5 Less detailed studies have obtained SB profiles from *HST* images for M30 (Yanny et al., 1994; Sosin, 1997), NGC 6397 (King et al., 1995) and NGC 6752 (Ferraro et al., 2003).

Baumgardt et al. (2004) perform extensive simulations of star clusters containing an intermediate mass black hole (IMBH). They find that the presence of the black hole induces the formation of a cusp whose 3-dimensional density profile has a  $-1.55$  slope. In projection the slope of the cusp is much shallower, yet different than zero. Recently, there have been two claims for the presence of a medium size black hole at the center of two globular clusters. One is for M15 (Gebhardt et al., 2000a; Gerssen et al., 2002, 2003) and the other one is for the giant globular cluster G1 in M31 (Gebhardt et al., 2002).

Although this is still a very controversial subject (Baumgardt et al., 2003b,c), it is crucial to be able to differentiate between the two possible dynamical states (i.e. core-collapse vs. intermediate mass black hole). Having reliable SB profiles near the center of GCs will be a key part of future dynamical modeling.

### 2.1.1 Non-parametric Models

The way in which light profiles are characterized has important consequences for dynamical analysis. The advantage of using parametric models lies in the fact that they provide a smooth profile even for sparsely sampled data, and that they have an analytical deprojection. However, the quality of the data is now good enough that it is not necessary to use a parametric profile. Furthermore, small differences or biases between the parametric fits and the data will be greatly amplified during deprojection, causing the luminosity density to be possibly poorly represented by King models. Parametric fits have a side effect of underestimating the confidence intervals for three dimensional distributions, since the range of possible solutions is always larger for non-parametric analysis than for a parametric one. The draw-back of not forcing a functional form to the distribution is that the data always have some amount of noise. Deprojection involves a derivative of the surface brightness profile; therefore, any amount of noise will be greatly amplified during the deprojection. Thus, non-parametric algorithms require some degree of smoothing, and the reliability of the result depends on the technique and the amount of smoothing used. Ultimately, there is a problem of assessing whether the fluctuations in the data are real or not. This is particularly important when the focus of the study is the inner parts of globular clusters. In this work, we use a

non-parametric approach to analyze our data, similar to that used for galaxies in Gebhardt et al. (1996).

## 2.2 Simulations

There have been a variety of techniques used in the literature to measure radial profiles for globular clusters, both with star counts and integrated light. We performed extensive simulations in order to test the reliability of different methods for obtaining accurate surface brightness profiles, which we describe below.

The two most complete studies to date base results on star counts and both correct for completeness. Sosin & King (1997) use artificial star tests in order to obtain a SB profile for M15. They add synthetic stars over their image of M15 and measure the recovery rate of their photometry software. A problem in this case is that it is hard to know the effect of the underlying stellar distribution on the results, since the true stellar distribution is not known. Guhathakurta et al. (1996) perform simulations over a blank image, controlling all the input variables. They compare the photometry of input and output stars one by one, calculate a completeness factor for the number of stars in a given annulus and construct the SB profile from star counts using those correction factors. This is a standard procedure that has been tested by many authors, but it does not test for degeneracy that could arise from different underlying profiles yielding the same final result. Since our goal is to provide a general prescription by studying the full range of profile slopes, our method should not depend on the type of profile for each cluster (i.e. cusp vs. core). We perform simulations over blank images, thus having control over the input parameters such as the stellar profile, luminosity function and total number

of stars. Below we outline each step. We argue that using integrated light is superior for measuring an unbiased SB profile (compared to star counts) if the cluster contains a large enough number of stars.

### 2.2.1 Image Construction

In order to test alternative methods for measuring surface density profiles, our goal is to create images that resemble those obtained by the PC chip as closely as possible. The first step toward creating images is to produce an input list of stars. We start with a luminosity function for M5 (Jimenez & Padoan, 1998) and a desired surface brightness profile. The effect of mass segregation is not included in these simulations. From the functional form of the luminosity function and the SB profile, we construct a probability distribution for a star having a certain magnitude (from the luminosity function) and radial distribution (from the surface brightness profile). Stars are generated randomly around a given center from those probability distributions. By performing star counts in magnitude bins we confirm that our resulting star list represents the supplied luminosity function. The same test is performed in radial bins for surface brightness. With this method, we create various master lists of stars of a given surface brightness profile. Results with fainter and brighter versions of the luminosity function are discussed below. We use five different power-law profiles  $\Sigma(r) = r^{-\beta}$ , with  $\beta$  of 0.1, 0.3, 0.5, 0.7 and 1.0 as the supplied functions for the surface brightness. We also create images for a King profile with a core radii of 90 pixels. The images have 200,000, 50,000, 10,000, and 1,500 input stars within a 200 pixel radius ( $20''$  for WFPC2 pixel scale). Five individual realizations are created for each pair of input number of stars and profile shape with the goal of performing statistical analysis.



The images are created using the DAOPHOT (Stetson, 1987) routine “ADDSTAR”. For a base image, we use an actual WFPC2 image containing very few stars that are cleanly subtracted. This process results in a realistic background including cosmic rays and bad pixels. The routine adds Poisson noise and read out noise as well. The supplied point spread function (PSF) is constructed from the base *HST* image. We do not include spatial variation of the PSF. The PSF radius defined for DAOPHOT when building these images is 9 pixels.

### 2.2.2 Center Determination

Having a good estimate of the center position of a cluster is crucial to obtain an accurate surface brightness profile. Using the wrong center typically produces a shallower inner profile. We design a technique to measure the center that assumes the cluster is symmetric. A guess center and a radius from that center are chosen. The circle defined by the guess center and the chosen radius is divided into eight segments where we count stars and then we calculate the standard deviation of the eight number counts. This same calculation is performed for various center coordinates distributed around the initial guess center with the same defined radius. The grid of the centers consists of every five pixels near the center in all directions and every ten pixels further away from it. This produces a map of coordinates with a standard deviation value associated to them. If the cluster is symmetric, the standard deviation of the eight segments should reach a minimum value at the center of the cluster and have larger values anywhere else. We fit a surface to this map using a two-dimensional spline smoothing technique developed by Wahba (1980) and Bates et al. (1986). The minimum point in the surface is our chosen center.

The method can be used iteratively until the minimum lies in the finely spaced part of the grid.

All the simulated images have the center in the same position right in the middle of the chip. The size of the circle we use for our octants method is 170 pixels, which is slightly smaller than the radial extent of the simulated clusters. We calculate the distance between the measured and the real center (in  $x$  and  $y$  positions separately) for each of the five individual images in a given setup, then calculate the average and the standard deviation. Figure 2.1 shows the accuracy of the center measurements for all input power-law and King profiles. Results are shown for both the  $x$  and  $y$  coordinates in the case where we input 10,000 stars. We observe that the largest deviation is equivalent to 5 pixels for this group of simulations ( $0.5''$  on the pixel scale of WFPC2). The center estimation improves with the degree of concentration of the cluster and with increasing number of stars. Similarly, the quality of the estimation decreases with decreasing number of stars and degree of concentration. As expected, this method works best when the SB distribution is not flat in the entire image.

### 2.2.3 Surface Brightness Profile

We test several different ways to obtain radial profiles on the simulated images. The profiles are obtained by measuring both integrated light and star counts. We note that both techniques have their advantages and disadvantages; for example, star counts can measure different radial profiles due to mass segregation while integrated light cannot. However, we argue that star counts are significantly less reliable compared to integrated light when trying to measure the global radial profile. When measuring integrated light, we use

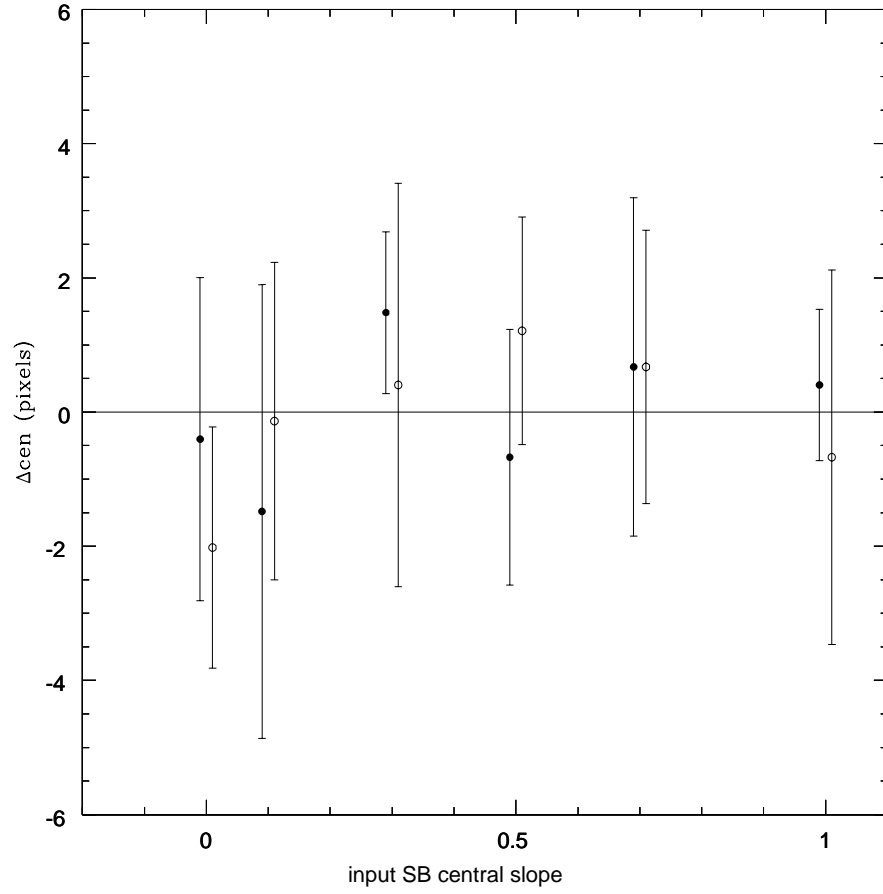


Figure 2.1 Comparison between the measured and input center for various sets of simulations with 10000 input stars. Zero slope is for the King profile case and the rest are for power laws. The average distance between the actual and measured center is shown for the  $x$  (solid points) and  $y$  (open points) coordinates in pixels. A small horizontal offset is introduced for clarity. Error bars are the standard deviation of the five individual measurements for each case. Each WFPC2 pixel is  $0.1''$ .

two different statistical estimators—the average and the biweight (Beers et al., 1990)—to get counts per pixel in a given annulus. Although the average is an optimally efficient estimator for central location when dealing with Gaussian distributions, it can be very biased when the underlying distribution is not Gaussian (i.e. having outliers). The biweight provides a robust estimate of the central location (i.e., mean) even when including a significant number of outliers because it is a robust estimator that de-weights the data points that lie far away from the mean. Since our images are made from discrete sources, there are a large number of ‘background’ pixels and a large number of ‘star’ pixels in each annulus, so the distribution is certainly not Gaussian. It is important to explore the effect of using a robust estimator versus using the average.

To measure star counts, we have to first measure the locations and brightness of all stars using DAOPHOT. We perform PSF fitting star subtraction on the images using the ALLSTAR routine with the same PSF we used to construct the image. This does not make the subtraction perfect since we introduced Poisson noise when constructing the images. Crowding and read noise have an important effect on DAOPHOT’s abilities to find stars. We observe this by comparing the number of input versus found stars in each simulated frame. For the 200,000 input stars case,  $\sim 3800$  are found, while for the 50,000 input stars case,  $\sim 3000$ . To avoid confusion in the following we refer to the groups of simulated images by number of input stars instead of number of detected stars. We now can measure integrated light in two different images, the original one with all the stars included (from now on called ‘full image’) and the one with stars subtracted, which includes only the background light and it is smoother (from now on called ‘subtracted image’). We use two sets

of annuli to measure SB from integrated light; one has steps of three pixels from 1 to 20 pixels radius and the other has steps of twenty pixels between 10 and 200 pixels radius. The sizes of these annuli are a compromise between measuring at the smallest possible resolution and providing a smooth curve. The radius associated to each annulus is the midpoint between the outer and inner radii, while the surface brightness value is the number of counts per pixel divided by the number of pixels in a given annulus. We find that when using the average estimator, the profile obtained for integrated light is slightly biased and is very noisy, while the biweight estimator yields much smoother profiles with very little bias. The measurements on the subtracted image always yields a smoother profile than that obtained from the full one. Figures 2.2 and 2.3 show the input profiles together with the five individual measured profiles for various simulations with 50,000 input stars. We show a King profile, and the 0.5 and 1.0 power laws. In the cases of concentrated profiles and large number of input stars, both estimators produce shallower profiles toward the center for the subtracted images. The reason for this bias appears to be an over-subtraction near the center of the cluster stars where the crowding problems are worse. The program subtracts part of the background starlight as part of the stars which in turn produces a flatter looking profile near the center of the cluster. We also observe that the profiles obtained from the full image tend to look steeper than the input profile for the steepest power laws (inner slopes in the range  $0.5 - 1.0$ ) as it can be seen in the leftmost panel of Figures 2.2 and 2.3. This is likely due to the contribution of the brightest stars near the center where integrated light is being divided into very few pixels, so the proportional contribution from the presence of a bright star is much larger near the center than in the outskirts. This effect can potentially be even larger for real clusters since they are known to have a degree of mass segregation (Howell

et al., 2000), and therefore they have a larger relative number of bright stars near the center.

Since our goal is to obtain an unbiased smooth profile, we attempt alternative ways to measure integrated light profiles. One is to subtract only a percentage of the found stars, just enough to remove noise, but not so many that we get over-subtraction problems. We test for different percentages and compare them with a histogram of found stars in order to assess which stars are contributing to the observed bias. After extensive testing, we conclude that subtracting the 10% brightest stars is optimal. This normally subtracts the giant and horizontal branch stars leaving most of the main sequence. Another approach consists of masking a smaller percentage of bright stars. We choose a masking radius of 5 pixels; this takes care of a large portion of the light in each star, but it is small enough to avoid having too few pixels to sample in the central regions. In this case we obtain profiles with some amount of noise, but we eliminate the over subtraction problem. By eye inspection of the profiles (Figs. 2.2 and 2.3), it appears that the subtracted or the partially subtracted profiles are the least biased and/or least noisy way to recover the input profile for the shallower power-laws, while the masked profile is optimal to recover the higher power-laws. We qualitatively test the quality of measurements from these profiles below.

We test the effect of changing the faint end of the luminosity function for the steepest power-law case by decreasing the number of faint stars. Our goal is to explore the effect of a change in background light on the final profile. We normally use a luminosity function that rises all the way to stars 6 magnitudes fainter than turnoff stars ( $\sim 18$  mag). We change this to a flat distribution for the faint end (21 – 24 magnitudes), therefore having a lower contribution from

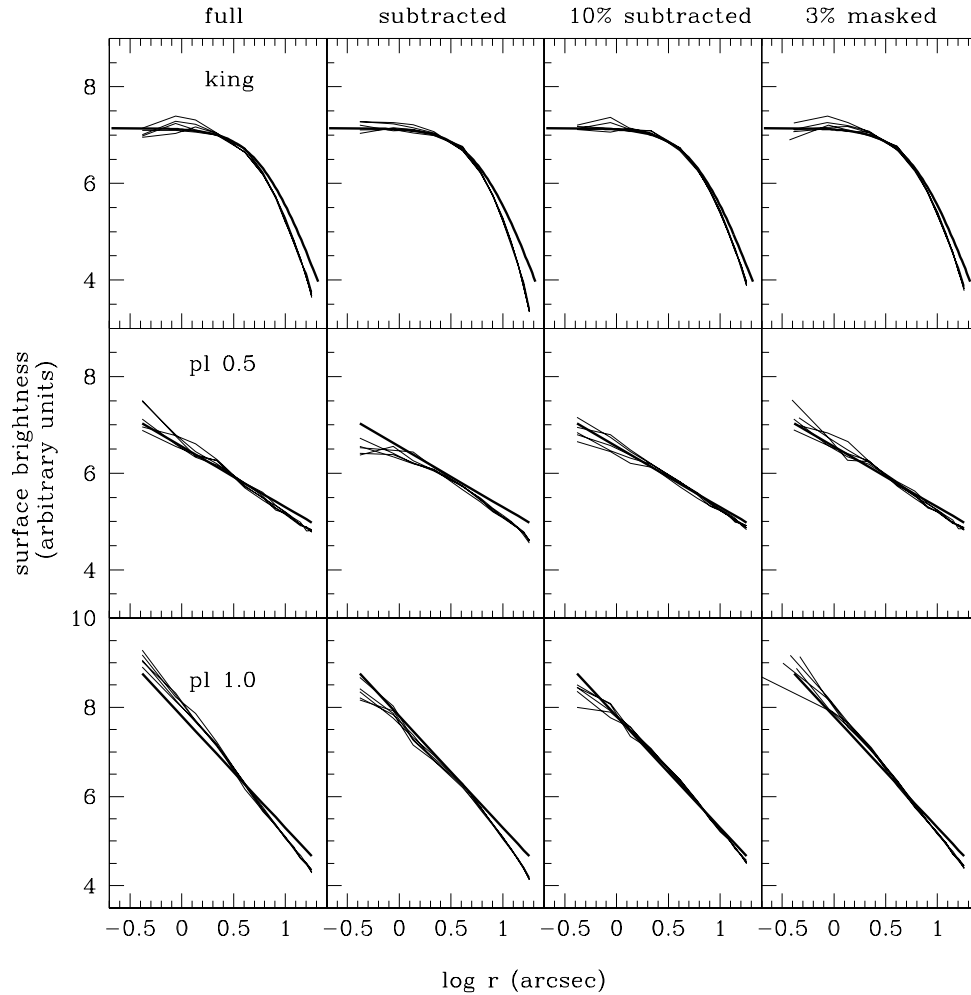


Figure 2.2 Surface brightness profiles for three groups of simulations with 50,000 input stars. For each case (King profile, 0.5 power-law, and 1.0 power-law) five individual measurements (thin lines) are plotted against the input profile (thick solid line). The profiles are measured from four different images: full, subtracted, 10% brightest stars subtracted and 3% brightest stars masked. The vertical axis is on an arbitrary magnitude scale.

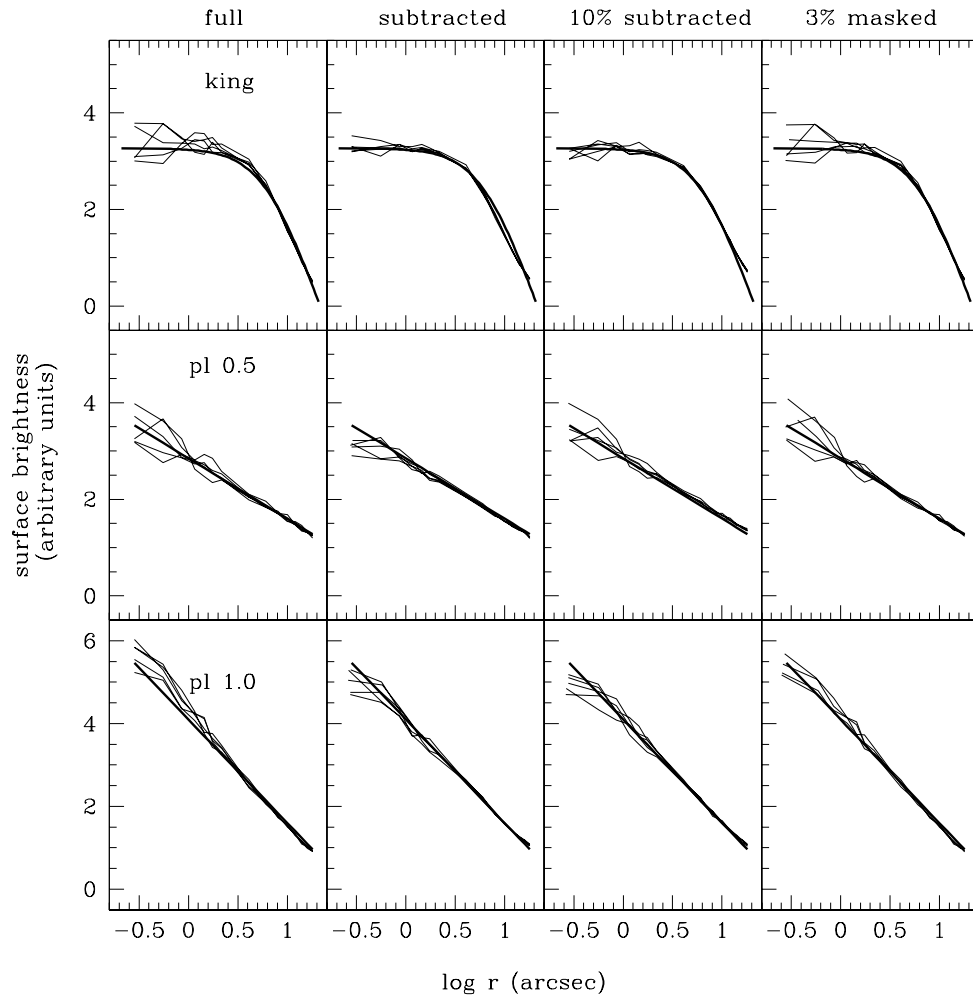


Figure 2.3 Same as previous figure but for simulations of fainter clusters. The groups of simulations were constructed by decreasing the brightness of stars by two magnitudes.



background light. We find that the effect is negligible on the final profile; the shape of the measured SB profiles was not affected by this change. Therefore, we conclude that the background light from very faint stars is not an important contributor to the SB profile when measuring integrated light. This result implies that the possible effects of mass segregation are reduced when we measure the profile from integrated light, since the contribution to the profile comes from stars with very similar masses. Therefore, the variations in the radial profile between the masses of those stars contributing to the integrated light are minimal. We also test for the effect of distance by using the same input lists for all cases, but making the stars two magnitudes brighter in one case and two magnitudes fainter in another. We obtain smoother profiles for the brighter case and a noticeable bias at large radii, where the profile is slightly underestimated. For the fainter case the profiles are noisier, but the bias at large radius seems to disappear (Fig 2.3). The over-subtraction related to crowding is amplified for the brighter case and smaller for the fainter case. M5 (the source of our luminosity function) has one of the brightest apparent magnitude horizontal branches in the galactic globular cluster system, so most of the actual observations will be better represented by the simulated images created with the original and fainter star lists.

Star counts profiles are obtained in the same sets of annuli we use for integrated light. Due to crowding near the center of the images, only a fraction of the faintest stars are detected there. If we include those stars in the star counts, they tend to flatten the overall profile, particularly for the steep profiles and large number of input stars. As a consequence, we decide to use only the 50% brightest stars to construct this profile, since this is the limit where the shape of the input profile is recovered. In general, the star

counts profile, as we construct it, can be used only as a comparison tool since it is too noisy to provide a robust result. It is worth clarifying that we do not apply any correction to star counts due to crowding, which is the normal procedure used by other authors to obtain star counts profiles in these type of fields. At large radii, star counts are probably the only way to obtain a surface density profile. They are certainly the only way to measure the variation in profiles between different stellar groups within a cluster, which is something that cannot be measured with integrated light. However, at small radii, crowding effects severely limit the usefulness of star counts since they require a significant correction.

Surface brightness profiles obtained from integrated light can be noisy for some cases (least concentrated objects, lower signal-to-noise). Therefore, in order to measure inner slopes, we have to apply some kind of smoothing and check whether that smoothing biases our measurements. The smoothing technique is the one-dimensional version of spline smoothing mentioned in Section 2.2.2. It is based on the work by Wahba & Wang (1990) and described in detail in Gebhardt et al. (1996). We choose to apply a fixed amount of smoothing to every profile obtained in order to be consistent. The central slope is calculated by taking the derivative of the smooth profile on the few innermost points, which is equivalent to measuring at a radius of 3 pixels (0.3'' with the WFPC2 scale). Results are shown in Figure 2.4 for the 50,000 and the 10,000 input star cases. We plot input versus the average slope measured for the five realizations. The error bars represent the standard deviation of these measurements. Results confirm what the eye inspection of the profiles suggest. The subtracted and partially subtracted images yield a more reliable inner slope measurement than the full and masked image for the shallow slope

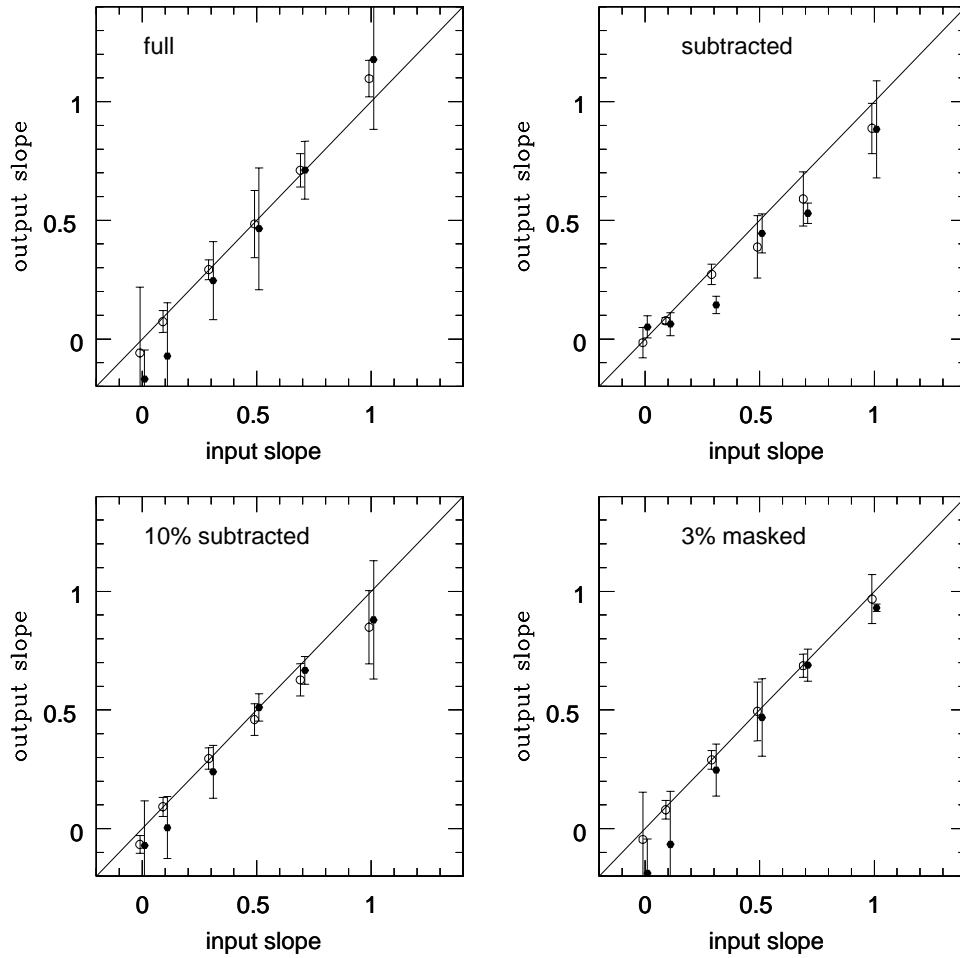


Figure 2.4 Input versus measured surface brightness slope for two groups of simulations. The open points show results for 10,000 input stars, the solid points show those for 50,000 input stars. A small horizontal offset is introduced for clarity. We show the average measured slope of the five individual profiles for each case. Error bars represent one standard deviation for the five measurements.

cases ( $\beta < 0.3$ ), which seem to have larger error bars, particularly for the 50,000 input stars case. We confirm that using the masked profile for those with steep slopes is more reliable; subtracted and partially subtracted cases tend to underestimate the slope. In order to further estimate the scatter, we created twenty images using 50,000 input stars and 0.7 power law. These twenty cases do not include the five cases already analyzed. The standard deviation of the slope is slightly smaller for the twenty cases as for the five images, so the error bars calculated for the five simulations case are an upper limit.

Besides measuring the core radius (radius where the luminosity drops by half the central value) we are interested in measuring the turnover radius (radius of maximum curvature) of the profiles. We do this by finding the minimum of the second derivative for the smooth profile. We created groups of simulations with small flat cores to test if we could detect such turnovers. Our results show that we can detect cores as small as  $1''$  with our spatial sampling.

Given these results, we use the same four images (full, subtracted, partially subtracted, and masked) for the real data. If the four profiles obtained from these images are consistent we take the smoothest version (in general, this is the masked case). If they differ near the center (as it is expected for concentrated cases) then we take the profile produced from the masked image since that is the one that traces the cusps best. As a general rule we do not use the profiles obtained from the full image and from star counts because they appear to be biased for some cases and generally noisier than the rest.

### 2.2.4 Uncertainties in the Simulations

The uncertainties in the surface brightness are due to two sources when using integrated light: the photon noise and the shot noise from having a limited number of stars (i.e., surface brightness fluctuations). Thus, in order to get the real uncertainties, we have to estimate the shot noise from stars. Star counts, on the other hand, directly recover the appropriate noise, but at the expense of higher uncertainties due to the difficulties in measuring the individual stars (i.e., completeness due to crowding).

For the simulations, we have the knowledge of the actual shot noise since we know the input number of stars. In order to determine how to include shot noise, we run simulations with the same input parameters but a different star list. The scatter from these different realizations then provides the actual uncertainties including both photon noise and shot noise from the stars. However, with real data we do not have the luxury of running different star lists; therefore we have to find a way to determine the shot noise directly. We use a biweight estimate of the scatter and then apply a correction factor. The biweight scatter is determined from the scatter in the photon counts in the pixels for a given annulus. We then compare the biweight scatter with the scatter of the photometric points between the five different realizations. The ratio of the real scatter to the biweight scatter is larger for the simulations with smaller numbers of stars. Thus, we have to correct the biweight scatter by the appropriate amount. When using the data, we do not necessarily know the underlying stellar surface density, making it difficult to determine the appropriate scaling for the biweight scatter. However, we use an alternative method that relies on assuming a smooth radial profile. We discuss this method for real data in Section 2.3.5. Both methods give the same range in

scalings, implying we have an robust estimate of the true uncertainties.

Alternatively, we could run proper completeness corrections and determine the corrected star counts. The standard technique would be to apply this as a function of magnitude and radius in order to determine the underlying luminosity function. With that in hand, one can straightforwardly measure the additional uncertainty due to shot noise alone. However, this will create an additional source of uncertainty due to the estimate of the completeness corrections themselves (the correction factors depend on the underlying distribution of stars which is precisely what is being measured, thereby causing a possible degeneracy). Another source of uncertainty is that star counts will always miss the contribution from the unresolved stars, which is not an issue for integrated light measurements. Therefore, we rely on the above approach, and the one outlined in Section 2.3.5, where we calibrate the uncertainty estimates for the actual data with the simulations presented here. Since the simulations demonstrate that we recover the central shape accurately, our adopted approach is reliable.

## **2.3 Data acquisition and analysis**

### **2.3.1 Sample**

*HST* has imaged a large fraction of all globular clusters in our galaxy. Piotto et al. (2002) obtained color magnitude diagrams for 74 galactic GCs from WFPC2 images. In addition, Mackey & Gilmore (2003b,a) obtained surface brightness for clusters in the LMC (53 objects), SMC (10 objects), and Fornax dwarf galaxy (5 objects), which we analyze in Chapter 3. Based on our simulations only a subset of the Piotto snapshot observations will provide a reliable SB profile since a minimum number of counts are needed in the

frame. Given the distribution of concentration, total magnitude, and apparent magnitude of the horizontal branch only a fraction of the imaged clusters are useful. The requirement is to have enough total counts in the frame. This can be achieved by the cluster being near (bright horizontal branch), containing a large number of stars, or being very concentrated (but not dominated by one star). In general, detecting stars six magnitudes fainter than the horizontal branch with a signal to noise of 20 is a minimum requirement for low concentration clusters. The criteria can be relaxed for highly concentrated clusters ( $c > 2.0$ ) and those with a large number of stars ( $M_V < -7.5$ ). Using these criteria we gather from the *HST* archive a sample of 38 GC imaged with WFPC2. It is ideal to perform the study with images in U-band (F336W) since giant stars contribute the same amount of light as main sequence stars at this wavelength, thus minimizing shot noise. Unfortunately, there are few images available with enough signal in U-band. Our selection criteria is using images observed in either V (F555W), R (F666W), or I (F814W) filters and to have an exposure time of at least 100 seconds, although most of the images have exposure times over 500 seconds (see Table 2.1). After testing for consistency between filters (details below), we realize we can also include images in the U filter with long enough exposure times ( $> 1000$  sec). The field of WFPC2 is  $2.6'$  in size, which is adequate to measure out to  $\sim 2.5$  half-light radius of most clusters but not out to the tidal radius. The scale of the CCD is  $0.1''/\text{pixel}$  for the WF chips and  $0.046''/\text{pixel}$  for the PC chip.

We use the WFPC2 associations from the Canadian Astronomy Data Center website<sup>1</sup>. These images are spatial associations of WFPC2 images from a given target, normally coming from a single program. The individual

---

<sup>1</sup><http://cadwww.dao.nrc.ca/>

raw data are processed through the standard calibration pipeline, grouped in associations and combined. The available data are multi-group image with the images for the three WF and the PC chips.

### 2.3.2 Image Processing

We analyze the WFPC2 images using the same method applied to simulated images described in the previous section. Once we have an individual image for each chip, we trim the edges due to increased noise there. We use the “FIND” task on DAOPHOT to obtain a list of stars, followed by the task “PHOT” to perform preliminary aperture photometry. We construct a PSF for each of the four chips. After extensive testing for methods to automatize this process, we conclude that the best way to obtain a reliable PSF subtraction is to choose PSF stars by hand. A single bad PSF star has an important effect on the quality of the subtracted image. Once we have the list of PSF stars, we use an iterative procedure where a preliminary PSF is constructed, neighbors to the PSF stars subtracted, and recalculate the PSF. We also test constructing a PSF with spatial variations but in the end this does not have an effect on the quality of the measured profiles, so we construct a constant PSF for all images and chips. In the end we have an image for each chip with all the stars subtracted and only background light remaining. We also produce images with only 10% of the brightest stars subtracted, and 3% of the stars masked as described in Section 2.2.3. A geometrical transformation of the individual images produces a mosaic image. We end up with four mosaic images for each cluster; one with all stars included, all stars subtracted, 10% of the stars subtracted, and with 3% brightest stars masked.



### 2.3.3 Cluster Center Determination

To determine the cluster center, we first transform all found stars to a combined coordinate list. We use transformations identical to those applied when making the mosaiced frame. With this master list we calculate both the center and radial density profile from star counts. The center is obtained with the method described in Section 2.2.2. The first guess center is made by visual inspection of the image when possible, then iterated until we find the best center. For the least concentrated cases ( $\sim 30\%$  of the clusters) we have to make our initial guess using Digital Sky Survey images with a larger field. The radius for our method is chosen so that all the stars counted would lie within the chip containing the center of the cluster and it is always larger than the core radius. For two of the clusters (NGC 6624 and M69), the center is too close to the edge of one of the chips, so we had to use stars on the adjacent chip to find the center. For another case (M13) the core is larger than the chip so we also had to use stars in the adjacent chips. Three of the clusters have too big and sparse cores for this method to work (NGC 5897, M10, NGC 6712). For these cases we used the center indicated in the Harris catalog (Harris, 1996); these cases are marked in Table 2.1 with an asterisk. It is worth mentioning that the sky coordinates reported in our table come directly from the WCS information contained on the header of the images, so they should be used only in the context of that specific image. We have noticed that the sky coordinates of a specific star can change by as much as  $1.8''$  in two images with different headers due to *HST* pointing uncertainties. The differences between our center coordinates and those contained in Harris' catalog are discussed in Section 2.4.1.

### 2.3.4 Surface Brightness Profiles

With the center from the star counts data, we obtain a surface brightness profile from the integrated light in each of the four images. We do this by measuring a biweight (see Section 2.2.3) of counts per pixel on a given annulus, and then dividing that over the total number of pixels on the annulus. We use a different set of annuli for each object. Our goal is to obtain the best possible spatial resolution, while keeping the noise as low as possible. For each case there is a trade off between these two quantities. We also bin in order to have a good sampling around the ‘turnover radius’. In the end we define three sets of concentric annuli: 3 – 7 pixels steps at 1 – 20 radius, 6 – 15 pixels steps at 15 – 35 radius, and 30 – 60 pixels steps extending the radial coverage to 800 pixels.

When we calculate the star count profile, as the analysis in Section 2.2.3 suggest, we cut the PSF subtracted star list to keep only the 50% brightest stars when we construct the profile. Stars are counted in the same annuli as the integrated light measurements and divided by the number of pixels in each annulus. In the end we obtain five profiles for each cluster from the full, subtracted, partially subtracted, masked images, and star counts. For most clusters the SB profile obtained from the full image or from the star counts are noisier compared to the others, so we never use them as the final profile. For the cases with steep cusps, there is always a difference near the center between the masked, partially subtracted, and completely subtracted profile, as observed for the simulations. In this case we always choose the result from the masked image since simulations show this is the least biased. For the cases where the masked, subtracted and partially subtracted profile have the same shape, we take the masked profile if it has the same amount of noise as the

rest; but for a few cases we take either the subtracted (M3, NGC 6287, M92, and NGC 6388) or the partially subtracted (47Tuc, M79, M5, M80, M62, M9, M69, and NGC 6712) because they are smoother. These are all cases where the central profile is nearly flat.

If a very bright or saturated star lies near the center of the cluster it can have an important effect on the final profile, either because the PSF subtraction is poor or because of the presence of diffraction spikes that are not included in the PSF. From tests where we mask bright stars near the center of a cluster, we determine that they only affect the shape of the final profile if they are within 1 arcsecond from the center. M70 is the only case where we had to mask a bright star located within this region. Since this is a saturated star, we also mask the diffraction spikes. This occurs at the cost of decreasing spatial resolution because we cannot use the inner 5 pixels for our measurements.

The profiles that we recover sometimes differ greatly from previous ground based data. In order to check that this is due to improved spatial resolution, we bin one of our high signal to noise WFPC2 images to the reported pixel scale (0.4'') of the data used in Trager's catalog (Djorgovski & King, 1986); we then convolve this image to account for the typical seeing reported for the observations in Trager's catalog ( $\sim 2''$ ). We compare the profile obtained from this binned-convolved image with that obtained from the *HST* image. Figure 2.5 shows that the effects of pixel scale and seeing can hide a shallow cusp that can be well measured with *HST* resolution. While this effect has been well demonstrated for galaxies (Lauer et al., 1995), it has not been appreciated for clusters. The profile obtained from binning and convolving the image lies on top of the Chebychev polynomial fit to Trager's photometric

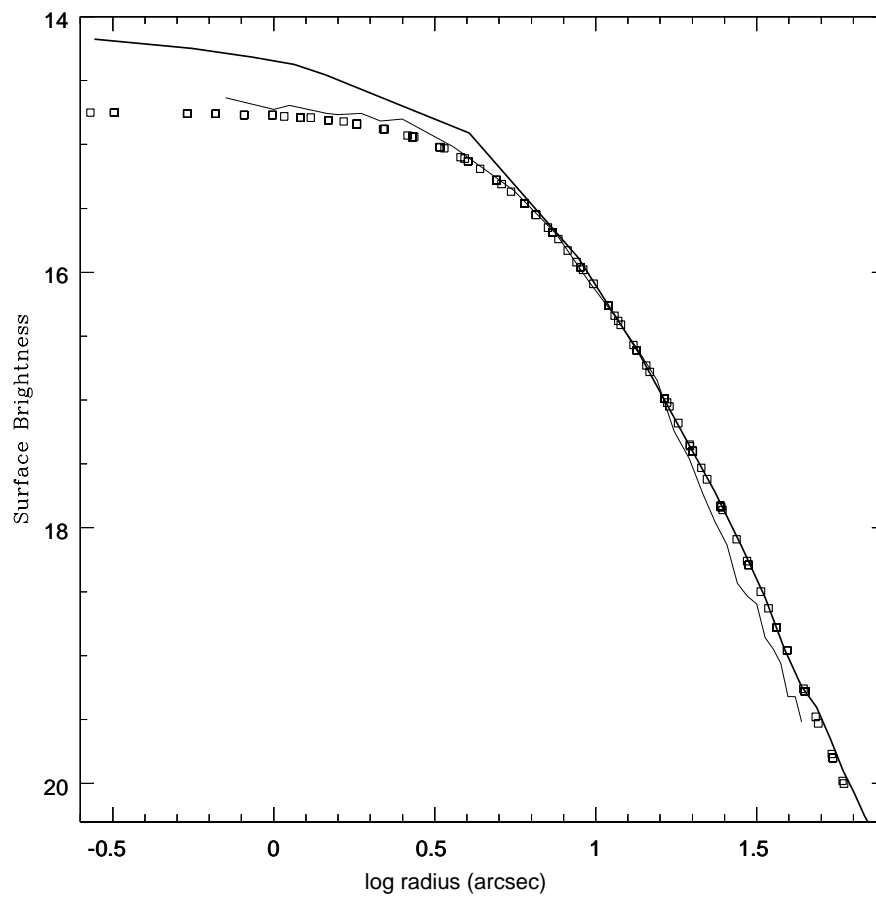


Figure 2.5 Surface brightness profiles for M54. The vertical axis shows a magnitude scale. The squares show the Chebychev polynomial fit from Trager's catalog. The thick line shows the profile obtained from a WFPC2 image with our method. The thin line shows the profile obtained from the same WFPC2 when it is binned and convolved to mimic a ground based image. The change in the central SB profile is due primarily to improved spatial resolution from *HST*.

points, while the *HST* profile is brighter near the center.

Another important test is to check for a possible filter dependence of the shape of the SB profile. M80 has observations available on F666W (780 sec), F555W (96 sec) and F336W (11,000 sec) filters. Figure 2.6 shows the SB profiles for each. We observe that the three profiles are consistent throughout the radial range, and they differ by the same amount from Trager’s Chebychev fit. Thus, we use results from various filters (F336, F439W, F555W, F675, and F814). We always choose the image with the highest signal to noise when images in multiple filters are available. 80% of the images we use are taken with the F555W filter. Obviously, color properties will cause some variations. Guhathakurta et al. (1998) report a  $\Delta B - V \sim 0.3$  mag from  $1''$  to  $10''$  for M30, which is the Galactic globular cluster with the largest measured radial color variation. Other clusters are expected to have smaller color gradients. Since our main objective is to obtain the central slopes, the small color gradients will have little effect.

We also require surface brightness profiles extending out to large radii. The WFPC2 camera only covers the central region, and we must rely on ground-based observations. For this, we use the Chebychev polynomial fit to the photometric points from Trager et al. (1995). We use our photometric points for the inner  $\sim 20''$  and the Chebychev fit for the outer region. In a few cases the agreement between the polynomial fits and our results is good throughout, but for many cases there are discrepancies. We normalize the *HST* surface brightness to the ground based data by matching the two enclosed light profiles, calculated by integrating the SB profiles. As expected, the enclosed light curves differ in shape at small radius, but for most clusters, the curves have the same shape at large radius. Regardless of which filter is

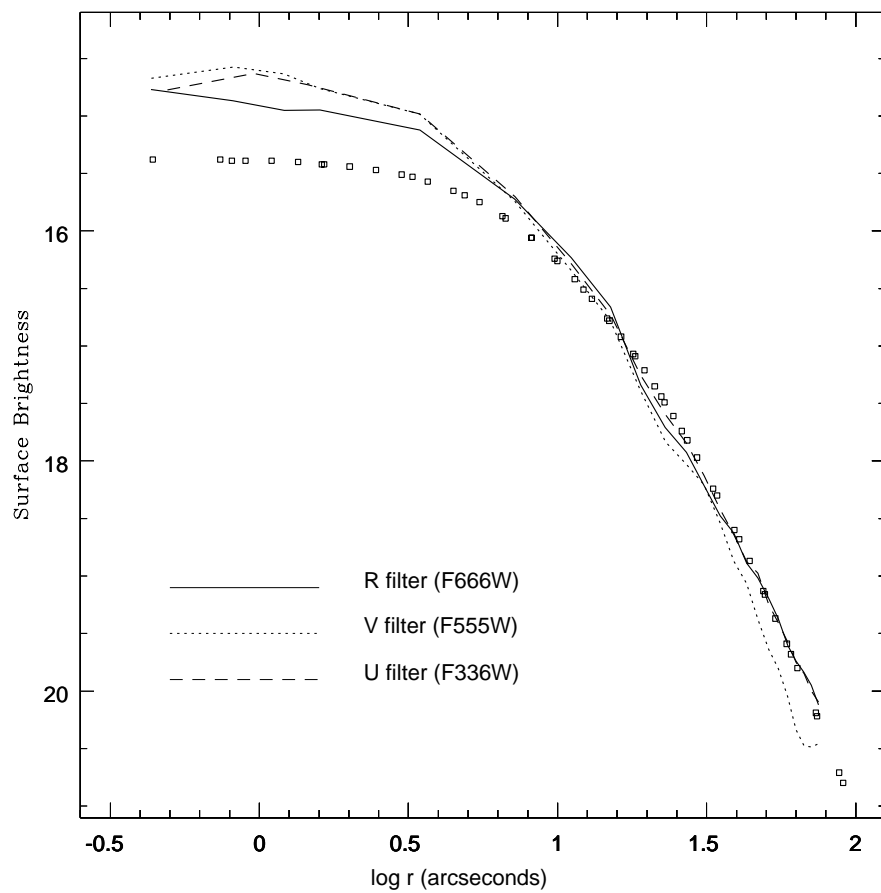


Figure 2.6 Surface brightness profiles for M80. The different lines show profiles in various filters (F336W, F555W and F665W). The vertical axis shows a magnitude scale. The squares show the Chebychev polynomial fit from Trager's catalog (measured in V band).

used to construct our profiles, the fact that they are all matched to photometric points in  $V$  and that the profiles are consistent between filters, brings all our photometric points to  $V$  magnitudes. There are a few clusters for which our normalization procedure is complicated (M70, NGC 6535, and M15). They all show a very steep profile through the entire radial range available in our images; since the ground based data show a core, the shape of the enclosed light profile obtained from *HST* doesn't quite match that of the ground-based case. Uncertainty in this normalization does not affect the shape of the inner profile, but it will affect the value of central surface brightness.

After normalizing, the final surface brightness profile is made from the combination of our photometric points in the center and Trager's Chebychev fits outside. Once we have a reliable surface brightness profile, we deproject it to obtain the luminosity density profile. This is done by numerically calculating the first Abel integral, as in Gebhardt et al. (1996). The Abel integral uses the derivative of these SB profile so any amount of noise in the profile is greatly amplified. Therefore, we have to apply some amount of smoothing before deprojecting it (as described in section 2.2.3). Some clusters, particularly the ones with shallow cores, yield very noisy profiles near the center, making the process of deprojection challenging. For these cases we apply a pre-smoothing process where we substitute the innermost three or four photometric points by the average between their two adjacent points. In this way we can apply a similar amount of spline-smoothing to every profile in the sample. For a few cases, even if we apply the pre-smoothing procedure, we obtain a surface brightness profile that decreases slightly near the center, which produces a luminosity density profile with a negative density in the center and we cannot achieve a proper deprojection. For these cases, we set the central luminosity

density slope to zero (marked with italics in Table 2.2).

We measure the central logarithmic slope of the smoothed surface brightness and luminosity density profiles by taking a first derivative with respect to the logarithmic radius. In the inner part of the profile, there is often a range where this derivative is constant, which implies that the profile has a constant slope in that region. We take the value of the derivative in this region as the inner slope for each cluster. The only exceptions are the objects which have steep cusps; for these cases, the slope changes through the entire radial range, so we take the value of the innermost points as the inner slope. Central slope measurements by other authors might be steeper for a given object, because they tend to fit a power-law in a more extended radial range (see example in section 2.4.3.5). For the cases where the SB logarithmic slope is slightly positive and we cannot achieve a deprojection, we just assign a zero value for the slope of the luminosity density. For these cases the values are written in italics on Table 2.2. We also measured the values of slopes in the region outside the core. In this case, since the values of the first derivative of the profile vary through this radial range we perform a least square fit to a line for the smooth profile.

Since we are re-deriving SB profiles, we need to measure core radius as well. Historically, the core radius has been considered as the radius where the value of the flux falls by half the central value. The radius often coincides with the radius where the profiles seem to turn over and change slope, which we call break radius. We distinguish these two radii for our profiles. The core radius is calculated by taking the central surface brightness and finding the radius where the flux falls by half this value. We should note that the central surface brightness is measured as the value for our innermost data



point, therefore, this value of core radius is resolution dependent for the non-zero slope cases. We also calculate a break radius by finding the radius that corresponds to the minimum of the second derivative of the smooth profile. This is the radius where the slope of the profile changes by the largest amount, so it can be seen as the turning point for the curve. Both radii are presented in Table 2.2. For the cases with slopes less steep than  $-0.5$ , where we can measure a break radius, we compute the ratio of the smallest resolution radius with break radius. For all cases this ratio is smaller than 0.15, which means that the break radius is at least 6 times larger than our smallest resolution radius. We plot this ratio versus the measured value of central SB slope and find no correlation. In this way we are confident that our reported values for central slopes in the weak cusps cases are well within the observed core of the clusters and the slope value is not due to lack of resolution.

### 2.3.5 Uncertainties for the Data

In Section 2.2.4, we describe how we estimate uncertainties for the simulations. our method is based on different realizations where we can include the shot noise from stars directly. Here we describe the method we used to calculate the uncertainties for real data and we calibrate these method against that used for the simulations. We assume that the underlying stellar radial profile is smooth, then the uncertainties of the photometric points should reflect deviations from a smooth curve in a statistically meaningful way (i.e., have a Gaussian distribution around the mean value). From the photometric points, the biweight yields an estimate for the central location and scale (scatter); this scale value is divided by the square root of the number of sampled pixels and used as the initial uncertainty for individual photometric points. We then

calculate the root mean square (RMS) difference between the smooth profile and the data points for the central region. The ratio of the biweight to the RMS should represent our lack of inclusion of shot noise from the stars. This ratio depends on the extent of the radial bins (i.e, the number of pixels used), therefore we use two different scalings for the different binning. The average scaling for the inner points is about 2 and about 7 for the outer points. This numbers are consistent with what we found in the simulations. Thus, we are effectively including shot noise from stars. The largest scalings occur for sparse clusters (NGC 6397, NGC 6535 and NGC 6752), as expected.

We calculate the uncertainties on slope measurements from a bootstrap technique and compare these with the values measured for simulated images. The bootstrap approach follows that in Gebhardt et al. (1996). From the initial smooth profile, we generate a new profile by generating random values from a Gaussian distribution with the mean given by the initial profile and the standard deviation from the photometric uncertainties. We generate a hundred profiles in this way and measure the 16–84% quartiles for the errors. Independently, each cluster is associated to one of the simulated cases according to its concentration and number of detected stars, and the standard deviation from Fig 2.4 is taken as the uncertainty. These two independent error measurements agree quite well, which gives us the confidence that the uncertainties calculated with the bootstrap method are reliable. Table 2.2 presents this results. The uncertainties for luminosity density slope measurements is also obtained from the bootstrap calculation. We do not estimate uncertainties in luminosity density slope for those cases where we cannot achieve a deprojection. We performed one more sanity check on our slope uncertainties by measuring the effect of increasing the uncertainties on photometric points by a factor of two.

From the bootstrap method, we find that the slope uncertainties increased by a modest factor, less than two, for most clusters. Thus, the slope uncertainties are not too sensitive to individual photometric errors.

## 2.4 Results and Discussion

### 2.4.1 Surface Brightness and Luminosity Density Profiles

We compare our measured centers (Table 2.1) with those listed in Harris' catalog (Harris, 1996). For 66% of the sample the difference is less than five arcseconds, 24% of the objects have a difference between 5'' and 10'' and only 10% have a difference larger than 10'' (NGC 1851, M3, NGC 6541 and M2). As mentioned before in Section 2.3.4, for three of the clusters (NGC 5897, M10 and NGC 6712) we used the center listed in the catalog as our center. For the most concentrated clusters, even a one arcsecond miscalculation of the center can flatten the central part of the profiles; so this might be another cause for missing weak cusps in previous measurements.

The SB profiles for the whole sample are shown in Figures 2.7 to 2.11. For each cluster we show the SB values measured from the image, the smooth profile, and the Chebychev polynomial fit obtained by Trager et al for comparison. We warn the reader that, as explained in detail on section 2.3.4, the photometric points beyond  $\sim 20''$  do not participate in the fitting of the smooth curve, instead, the Chebychev fit is used in this region. For most objects the agreement between the ground based data and ours is very good at large radii ( $> 10''$ ). There are a few cases that show disagreement between the two profiles; these clusters tend to show a steep inner profile (NGC 6284, NGC 6535, M70, M15), with the largest discrepancies in the inner 10 arcseconds. As we already discussed (Section 2.3.4) these differences may be due

to PSF effects. We observe that for 70% of the sample the central photometric points are brighter than the polynomial fit obtained from ground based photometry, sometimes changing the shape of the previously measured central surface brightness (i.e, making it steeper). The remaining 30% agree with previous measurements or have fainter photometric points near the center. For the extreme cases, the difference between the central SB value with previous reports is larger than 1.7 magnitudes (NGC 6284, NGC 6535, NGC 6652 and M15).

In order to check for any potential biases from our smoothing in the central regions, we compare with single-mass King profiles (King, 1966) fitted to the combination of our photometric points and Trager’s Chebychev fit. For these fits we keep the value of the tidal radius fixed (from Trager’s values) since our data is only in the central regions. Figure 2.12 shows representative fits for three clusters, 47Tuc, NGC 2808, and NGC 6293. For 50% of the sample, our smooth profile and the King fit are equally good fits to the data, as in the case of 47Tuc. For the other 50%, we obtain either a small departure from a flat core, as in the case of NGC 2808, or a clear large departure as in the case of NGC 6293. These departures are always in the same sense, i.e., the photometric points are brighter than the King fit towards the center and the deviation increases as radius decreases. We also performed power-law plus core fits with the functional form used by Lugger et al. (1995). We only performed these fits for the cases that depart from a King profile. The fits are performed using only the data points for the central arcminute, since we do not expect the outer part of the profiles to be described by a power-law. For most cases, the power-law plus core fit follows the same trend as the King fits, but NGC 6397 and NGC 6652 these fits are as good as our non-parametric

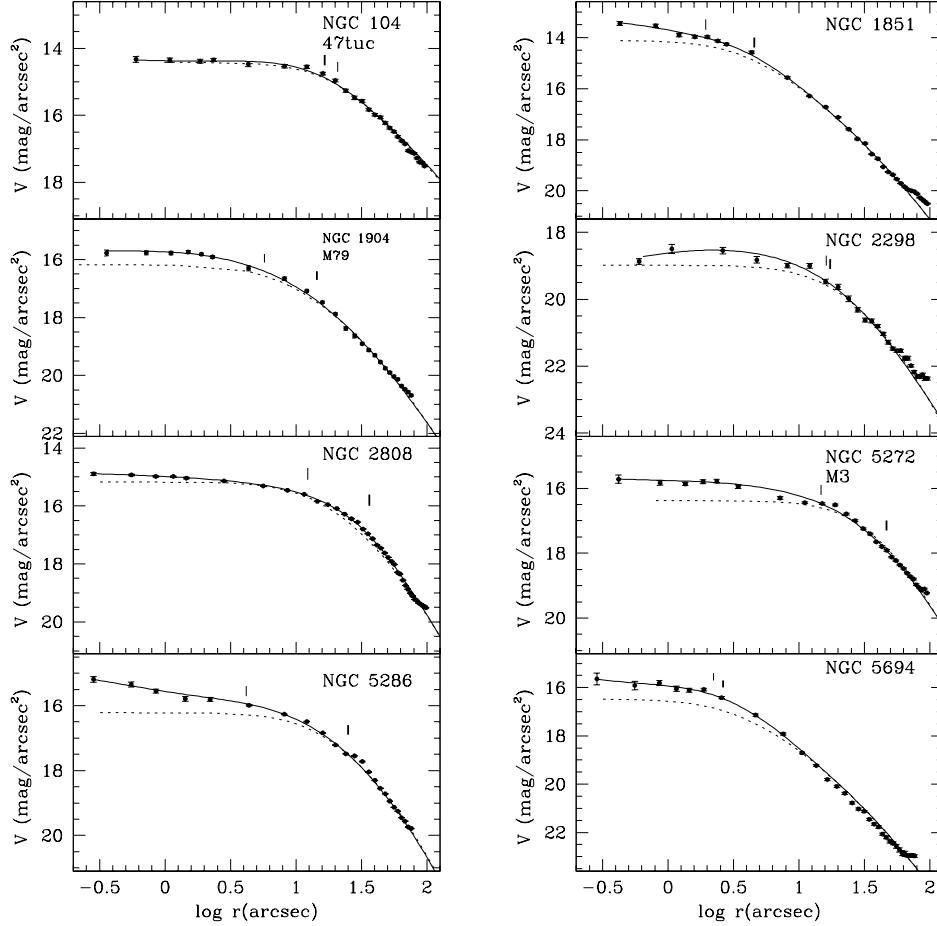


Figure 2.7 Surface brightness profiles for the entire sample. For each cluster we show our photometric measurements (solid points), our smooth profile (solid line), and Trager’s Chebychev polynomial fit (dotted line). The smooth profile comes from a fit to our photometric points inside  $\sim 20''$  and the Chebychev fit outside that region. For every panel the SB units are  $V \text{ mag/arcsec}^2$ . We mark the location of the core (thin vertical line) and break (thick vertical line) radii. The core radius is where the central flux falls by half its value and the break radius is where the second derivative of surface brightness with respect to radius reaches a minimum.

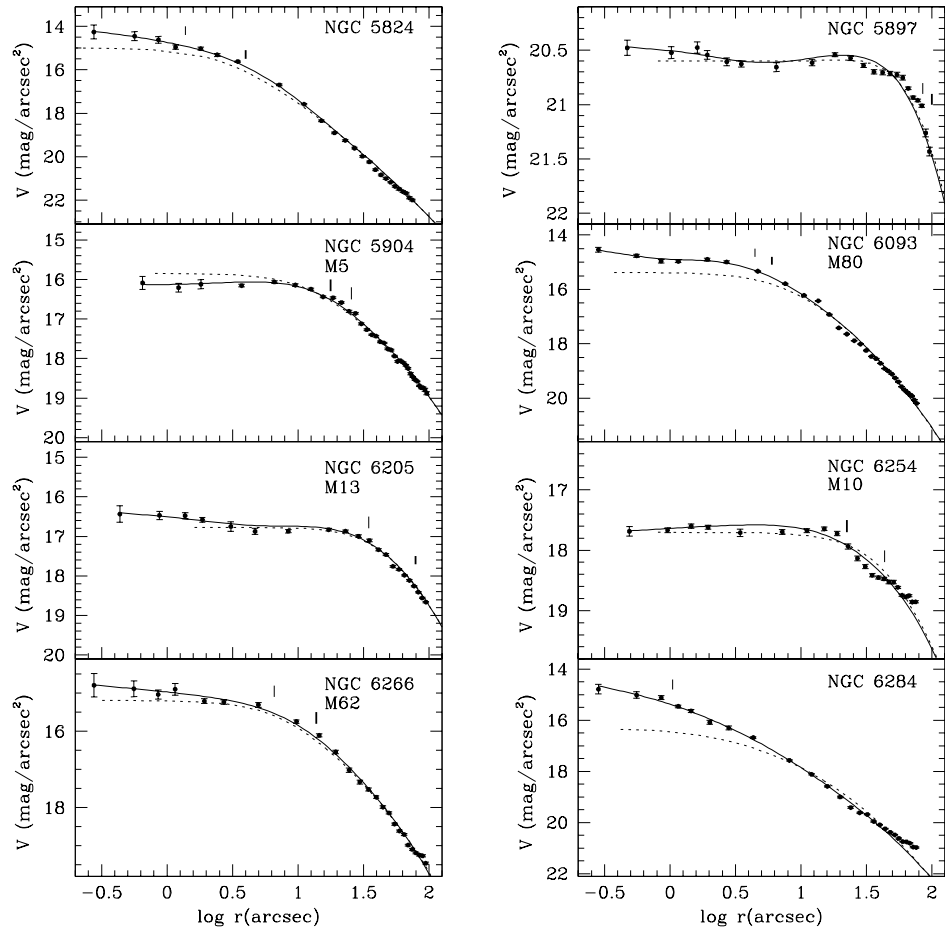


Figure 2.8 SB results continued

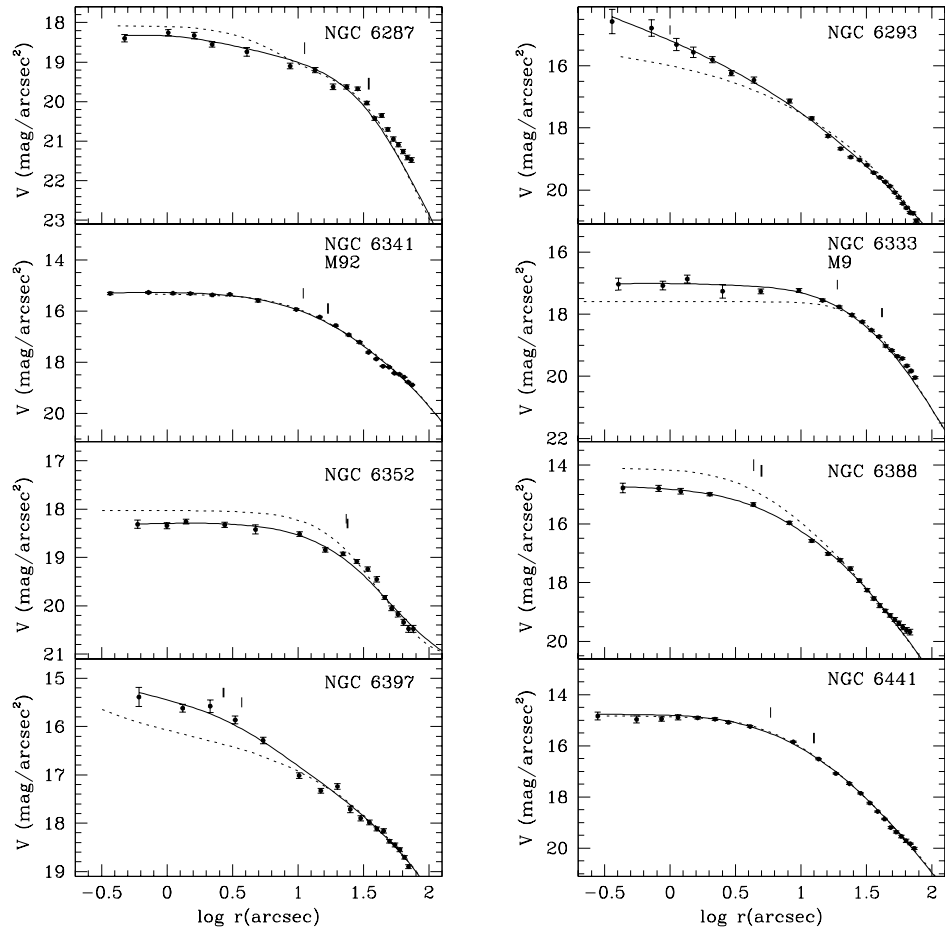


Figure 2.9 SB results continued

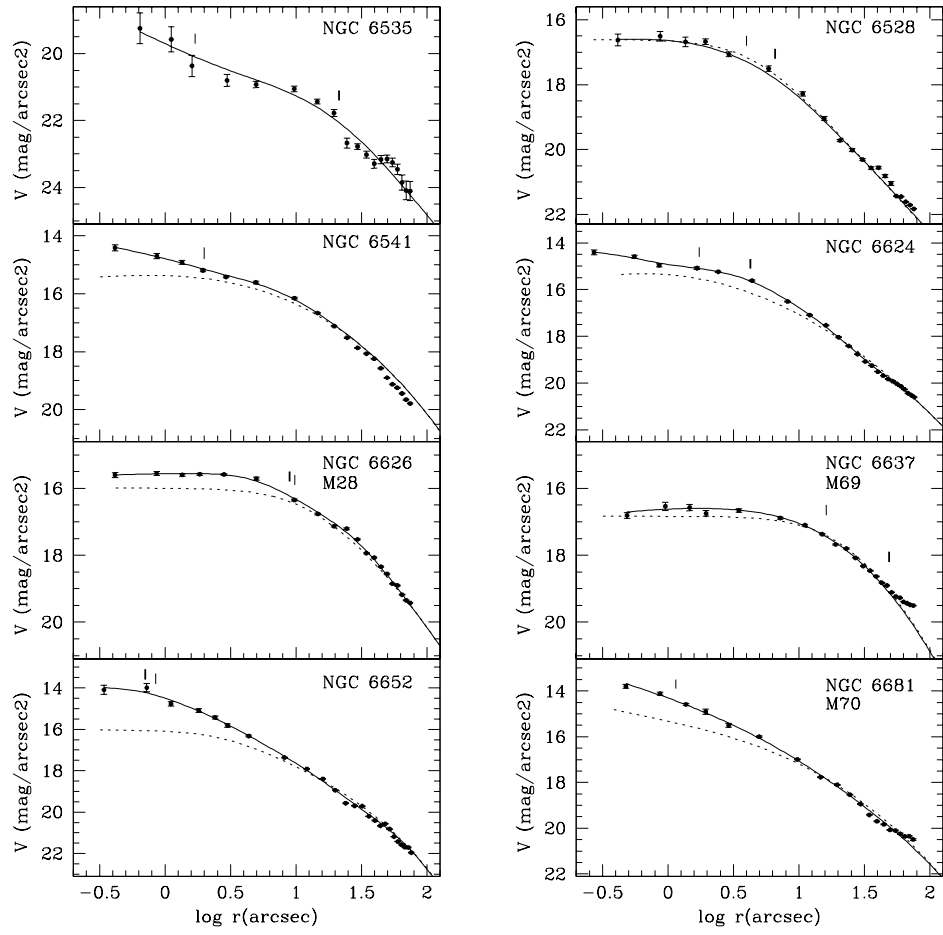


Figure 2.10 SB results continued



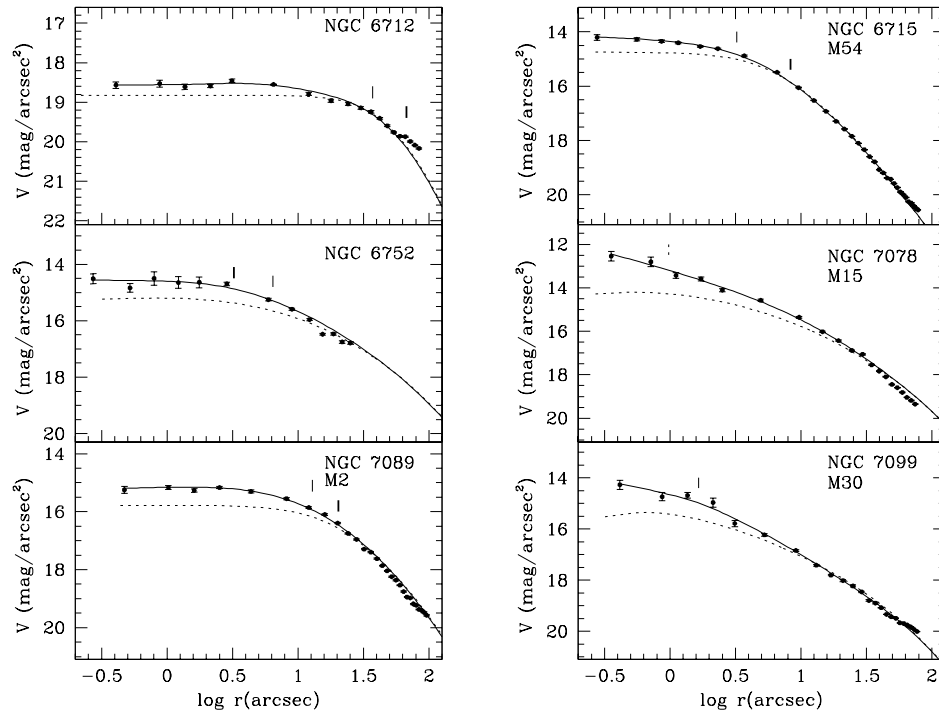


Figure 2.11 SB results continued

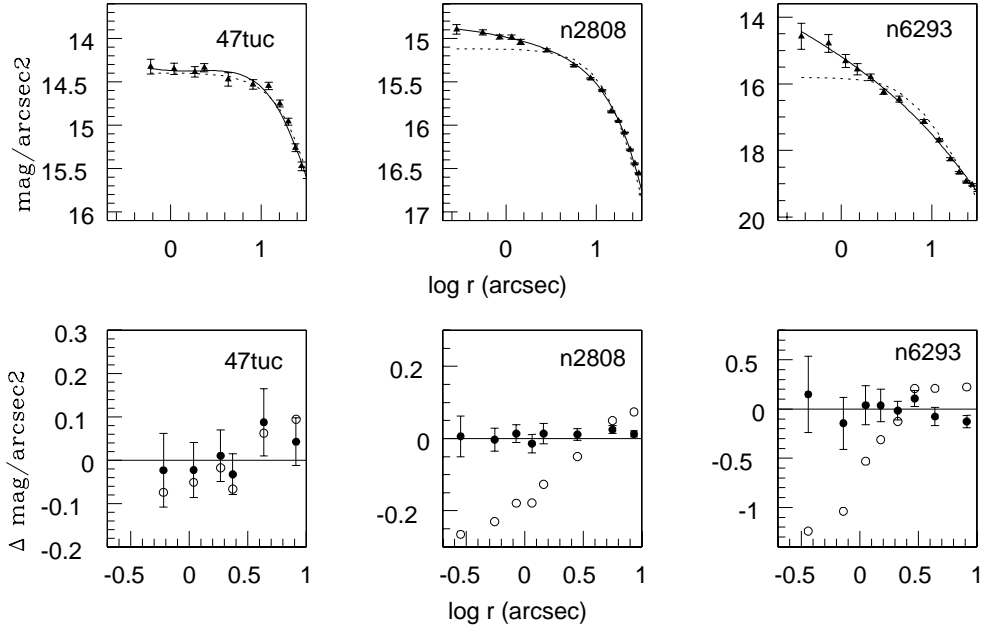


Figure 2.12 Representative single-mass King fits for 47Tuc, NGC 2808, and NGC 6293. The top panel shows the photometric points (triangles) along with our smooth fit (solid line) and a King fit (dotted line). The bottom panel shows the residuals for the smooth fit (solid points) and for the King fit (open points).

profile. We discuss the details for each object in Section 2.4.3.

All of the clusters previously reported as core-collapse show cusps, with the exception of NGC 6752, which shows a flat core. Only four of them (NGC 6652, M70 M15, and M30) show a  $\sim -1.6$  central logarithmic slope in luminosity density, which is normally assumed for objects in this state (Breedon et al., 1994). The rest have slopes between  $-1.2$  and  $-1.4$ . We consider all objects with luminosity density slopes more negative than  $-1.0$  to have ‘steep cusps’; they constitute 34% of the sample. 24% show weaker

cusps with luminosity density slopes between  $-0.2$  and  $-1.0$ ; many of these have been previously reported as flat cores or were marked as possibly core collapse on Trager’s catalog. We consider these objects to have ‘weak cusps’. Finally 42% of the objects in the sample show flat cores consistent with an isothermal distribution, even when their inner photometric points are brighter than previous measurements. If we group the weak cusps with the steep cusps, in total 58% of the sample do not show isothermal cores. The presence of so many non isothermal cores will have important consequences for the dynamical evolution of the clusters. No dynamical model or simulation predicts this distribution of slopes for GCs. Grillmair et al. (1995) make a detailed study of large radial structure for 12 galactic clusters. They obtain surface density profiles from star counts and find that most of the clusters depart from the King models previously fit to them because they contain stars in the extra tidal region. This result put together with the fact that more than half of the objects in our sample are not represented by isothermal cores leads us to think that King models do not describe well the surface density profile of many globular clusters.

Our measured errors for surface brightness slopes are on average 0.1 and the largest is 0.18. For the luminosity density slope the average is 0.28 and the largest error is 0.54. For the cases with steep cusps, the error is always under 0.35. Those with measured SB slopes under  $-0.2$  are all  $2\sigma+$  detections, implying that they show a deviation from an isothermal core. Assessing the uncertainties for the flat cases is particularly relevant since we want to evaluate the possibility of having positives slopes. Luminosity densities with a central minimum have been observed in a handful of galaxies (Lauer et al., 2002). These have been interpreted as two possible scenarios: one where a stellar

torus is superposed on a normal core due to a recent merger (this is quite unlikely in a globular cluster), and the other scenario where stars are depleted from the center due to a binary black hole interaction. Unfortunately, the uncertainty in our measurements for cores with positive slope is large enough to include zero slope.

For each profile on Figs 2.7-2.11, we mark both the core and the break radius. Seven of the steep cusp cases do not have a measured break radius because they do not show a clear turning point in the profile. We observe that for the rest of the sample these two radii do not always coincide. For all but six cases, the break radius is larger than the core radius, while for five cases the two are the same. The core radius that we report is a non-parametric fit as opposed to its historical value as one of the parameters for King fits.

We also check whether our limited spatial resolution (about  $0.3''$ ) has an effect on being able to resolve a core. We plot the ratio of our smallest resolution over the measured break radius against various properties; this ratio is always smaller than 0.2 implying we have at least five resolution elements inside the break radius for those clusters that have a turn-over in the light profile. We find no correlations; if all clusters have King-type profiles with small core radii, we would expect to see correlations.

#### **2.4.2 Slopes Distribution and Correlations**

Figures 2.13 and 2.14 show histograms of the surface brightness and luminosity density logarithmic slopes. There is no clear separating line for two classes of objects, so the sample cannot be cleanly divided into isothermal and core collapse profiles. Since our sample is only  $\sim 30\%$  of the full galactic globular cluster system, we have to determine potential biases. Trager et al.

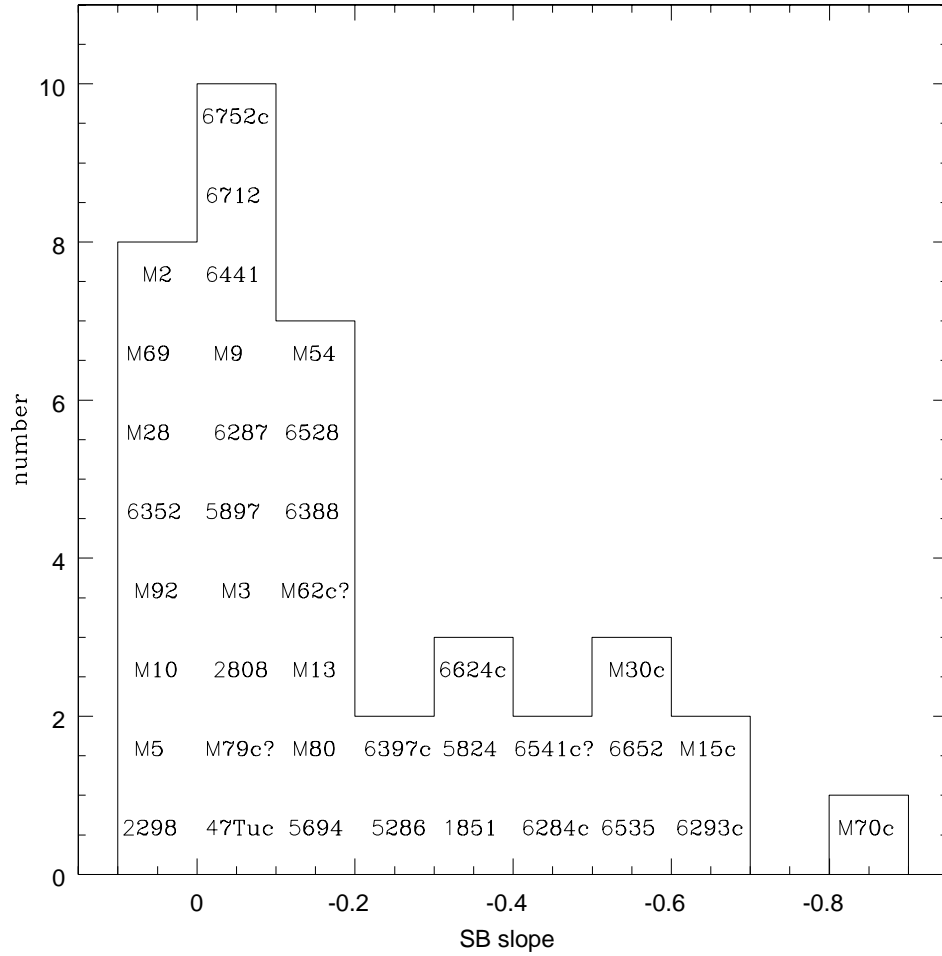


Figure 2.13 Histogram for surface brightness central logarithmic slopes. Individual clusters are shown in each bin. The name of the cluster is coded according to previously reported dynamical state in Trager's catalog. Marked with a 'c' for core collapse, 'c?' for possible core collapse and just the name for flat cores.

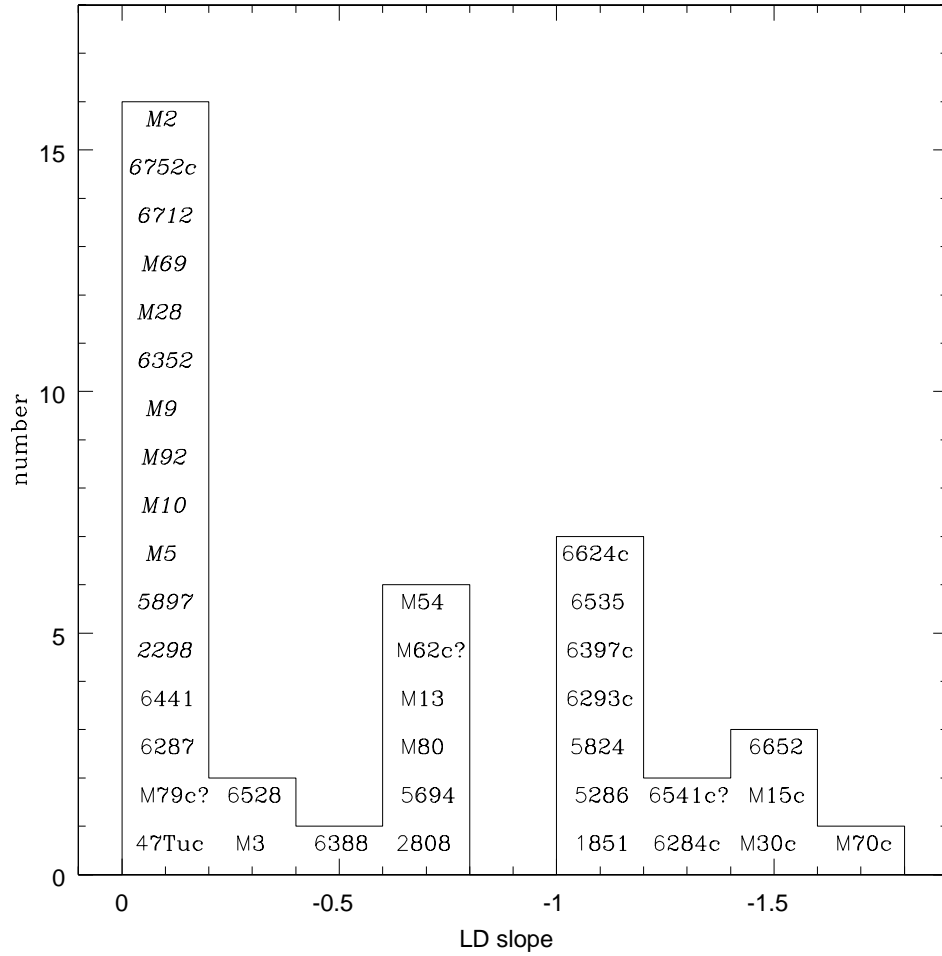


Figure 2.14 Histogram for luminosity density central logarithmic slopes. Cluster names are coded as in previous figure. Clusters in italics are those for which deprojection cannot be achieved due to diverging density profile near the center.

classify 16% of their sample as core collapse clusters and 6% as possible core collapse ('c' with a question mark in his catalog). Our subsample has 21% objects considered core collapse and 8% possible core collapse from Trager et al. Thus, our sample resembles the distribution for the full sample with a slightly larger number of core-collapse cases. All but one (NGC 6752) of the objects marked as core collapse fall in our 'steep cusp' category, while those clusters marked as possible core-collapse are found in all three categories. We find 17 objects previously classified as flat cores (i.e. classic King models) that are consistent with an isothermal profile. We can determine the fraction of clusters that have isothermal cores by comparing our SB histogram with that expected given our measurement uncertainties for the clusters that have nearly flat cores. Our average slope uncertainty is about 0.1. A Gaussian that contains 50% of the sample with mean 0 and sigma 0.06 (the average slope error for flat cores) matches the flat end of the slope distribution very well. The remaining population ( $\sim 50\%$  of the objects in the sample) shows a fairly uniform number of objects between slopes  $-0.2$  and  $-0.8$ . Thus, only half the objects in our sample are consistent with a King-type profile.

We plot logarithmic SB and LF central slopes against a variety of global properties of clusters taken from Harris' catalog or measured in this work. Figures 2.15 and 2.16 show these plots for both central slope values versus central surface brightness, total V magnitude, metallicity, logarithmic physical core radius, logarithmic physical break radius, logarithmic half-light relaxation time, velocity dispersion and age. Fig 2.15 also shows the relation between SB slope and LF slope. We observe some global trends. As it is to be expected, the clusters with steep profiles tend to have brighter central surface brightness values, although the very sparse cluster NGC 6535 is an outlier. There is an

indication that objects with steeper cusps are found in smaller objects (i.e. higher total magnitude); this trend is more clear for luminosity density slopes. Metallicity measurements do not appear to show any trend. The same is true for galactocentric distance, except that the objects with steeper cusps are all close to the center of the galaxy, but given the size of our sample this might just be a small number effect. Half-light relaxation time seems to be shorter for the steep cases. As it is to be expected, the core radius is smaller for clusters with steep profiles, while the break radius shows no correlation with slopes. Velocity dispersion and age show no correlation with slopes. Finally, the relation between surface brightness and luminosity density slope is not linear, as expected, and is similar to that observed for galaxies (Gebhardt et al., 1996).

The measured values for outer slopes range from  $-1.0$  to  $-2.5$  for the clusters in the sample. When we plot these outer slopes values versus global properties, and in particular versus either central SB slope or concentration, we find no correlations. So as far as this sample goes, we cannot distinguish between King-type or core-collapse objects from the outer slope of the profiles. This is illustrated on Figure 2.17 where we overplot all the observed profile, scaled in surface brightness and either their break radii (when they exist) or core radii (for the others). The profiles are color coded according to the classification given above for flat cores, weak cusps and steep cusps. It can be observed that although the different groups can be separated in the inner region, they do not seem to split into groups in the outer region. This figure confirms once again that the profiles cannot be clearly divided into flat cores and steep cusps, but that they span a continuous range of central profiles.



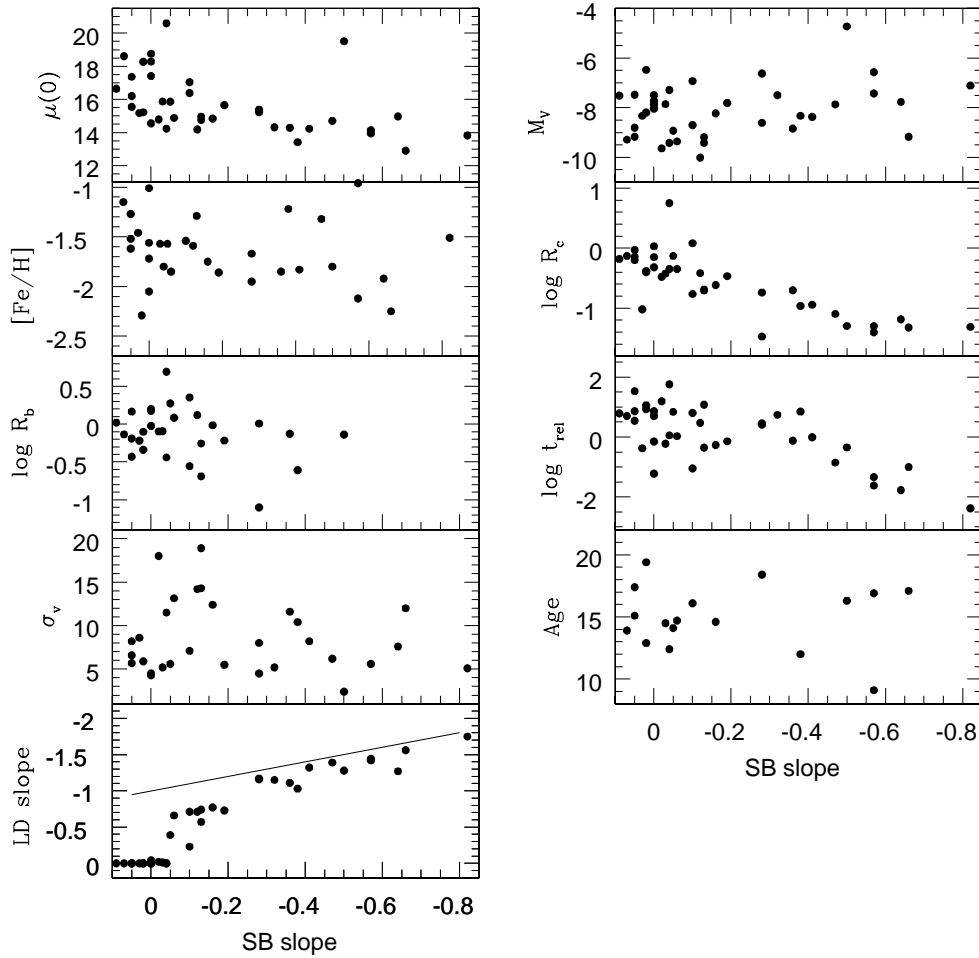


Figure 2.15 Surface brightness central logarithmic slope versus central surface brightness, absolute total V magnitude, metallicity, logarithmic core radius (in parsecs), logarithmic break radius (in parsecs), half light relaxation time, velocity dispersion, logarithmic age and luminosity density slope (the solid line represents ‘LD slope = SB slope + 1’). The distances to the clusters were obtained from Harris’ catalog. There is a trend between central surface brightness and slope (with one obvious outlier). There is also a trend with core radius and relaxation time.

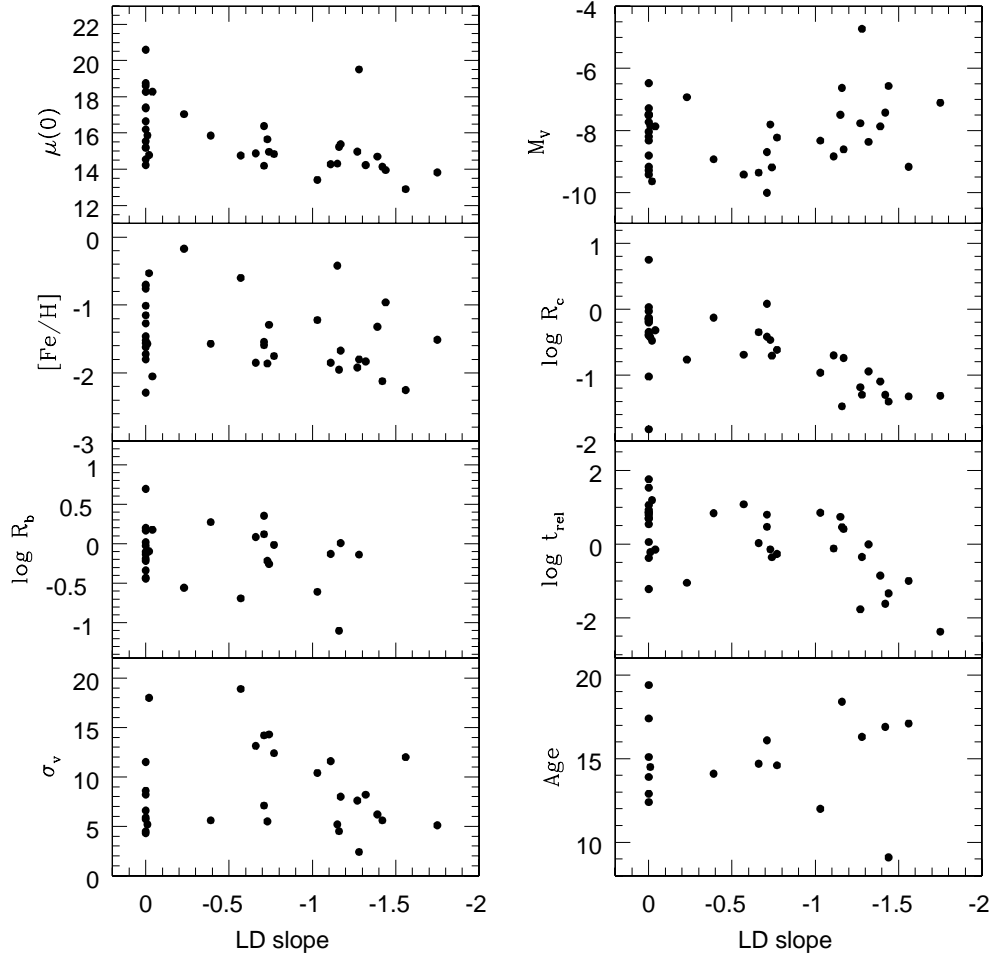


Figure 2.16 Luminosity density central slope versus central surface brightness, absolute total V magnitude, metallicity, logarithmic core radius, logarithmic break radius, half light relaxation time, velocity dispersion and logarithmic age.

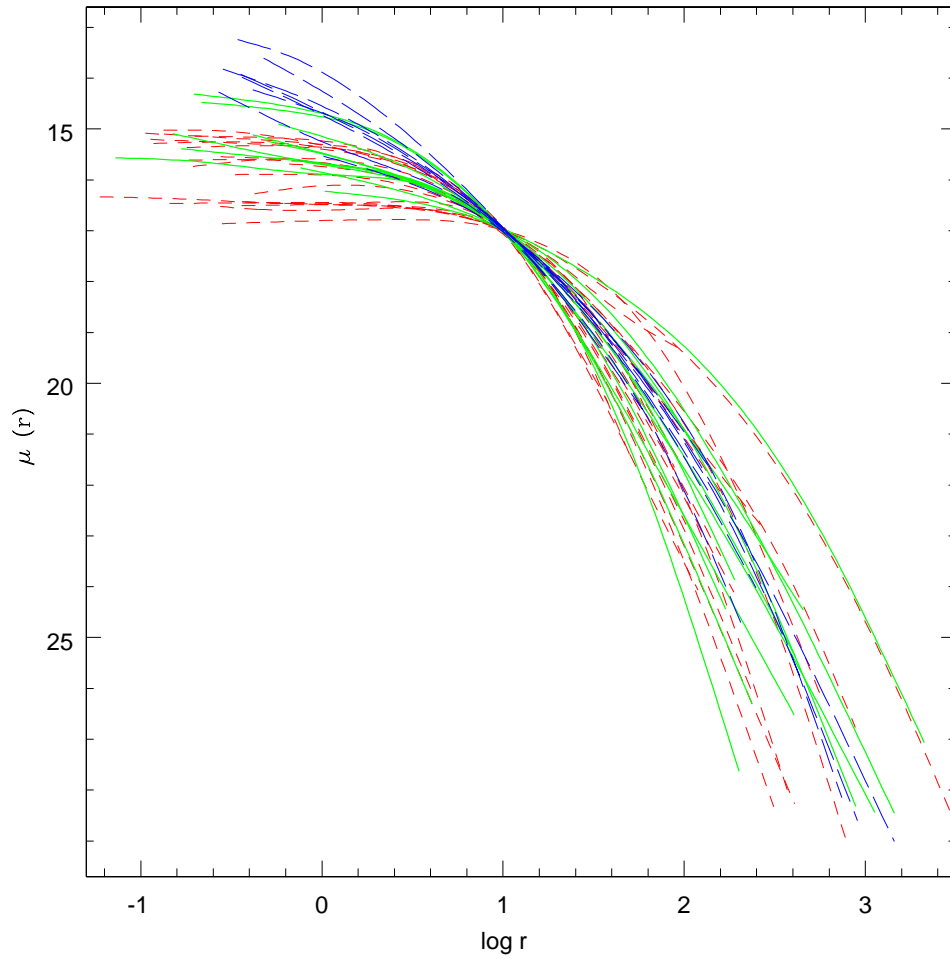


Figure 2.17 Surface brightness profiles for the entire sample. The profiles are normalized to a common point, therefore the units in the axis are arbitrary. Profiles are color coded according to their central slopes. Flat cores are shown in red (dashed lines), shallow cusps are shown in green (solid lines), and steep cusps are shown in blue (long dashed lines).

### 2.4.3 Individual objects

#### 2.4.3.1 NGC 6397

NGC 6397 is a peculiar object because it has always been considered to be in core collapse due to its steep inner profile, but unlike other objects considered to be in core-collapse, this one shows a sizable core. Lugger et al. (1995) report measuring a  $4 - 10''$  core. Our measurement for the break radius for this cluster is  $2.1''$ . We fit a power-law plus core function for the central region of the profile and we find that the fit with a  $4.5''$  core radius is a good fit, but only for the central  $10''$ . It could be the case of a partially resolved core. In previous studies the inner slope is measured in a radial range extending well beyond the measured core radius (as far as  $100''$ ). We measure inner slopes at the central few arcseconds for all objects in our sample, therefore our slope value for this object is much shallower than previous measurements. Our  $-0.37$  central slope value places this object in the weak cusp category.

#### 2.4.3.2 NGC 6535

NGC 6535 contains very few stars, therefore the image has low signal and the measured profile looks very noisy. We decided to include it in the sample because despite having so few stars, it shows a very steep central surface brightness profile. The photometric data shown in Trager's catalog for this cluster shows an important deviation ( $\sim 0.8$  mag) with respect to the Chebychev polynomial fit between  $2''$  and  $15''$ , where the photometric points are brighter than the polynomial fit. PSF effects might have been responsible for missing a cusp in this measurements.

### **2.4.3.3 NGC 6652**

NGC 6652 is not considered to be in core collapse, but it shows a very concentrated profile in our measurements. Trager et al. (1995) report a 4'' core for this object. Our power-law plus core fit finds a 1.15'' core and it is consistent with the photometry within the error bars. This could be another case of a partially resolved core. The central slope from the smooth profile is  $-0.57$ .

### **2.4.3.4 NGC 6752**

NGC 6752 has been subject to a number of studies. This is the only cluster in our sample for which we only analyzed the PC chip, without including analysis of the WF chips. Lugger et al. (1995) analyzed a ground-based U-band image of the cluster and conclude that the surface brightness profile does not present a core-collapse morphology. Ferraro et al. (2003) constructed a surface density profile for this cluster based on star counts. They fit the central region with two separated King models, which they interpret as the cluster being in post-core-collapse bounce. Our results indicate a flat core with a slope near zero for both the surface brightness and luminosity density profiles. Our difference from Ferraro et al. is likely due to noise in the star counts that they use.

### **2.4.3.5 M15**

There are a variety of WFPC2 images available for M15. For this reason we applied the exact same procedure to each of them in order to test the reliability of the profiles. We have a high signal-to-noise F555W image, a F336W image and a snapshot (60 sec) F555W image. In Figure 2.18 we

show our results for the inner part of the cluster, where we compare them with previously obtained profiles by Lauer et al. (1991), Guhathakurta et al. (1996) and Sosin & King (1997). Lauer et al’s analysis used a WFPC1 image, where they subtracted stars and measured the background starlight. Sosin & King’s curve comes from star counts in a narrow magnitude range and does not have any kind of smoothing applied to it, which is the reason why it looks much noisier than the other curves. Guhathakurtha et al’s curve comes from corrected star counts and includes smoothing. All three curves have an arbitrary vertical scaling. It can be seen that the profiles are consistent in shape through this radial range (inner 5 arcseconds), with the exception of Lauer’s profile, which appears flat toward the center. The center we measure is within 0.1 from that obtained by both Guhathakurta and Sosin & King, so we are confident that center estimation is not a problem for this highly concentrated object.

When measuring logarithmic inner slopes, the choice of the radial extent used for the slope measurement is crucial. Sosin & King measure a  $-0.7 \pm 0.5$  logarithmic slope by fitting a power-law over a large radial extent between  $0.3''$  and  $10''$ . Guhathakurta et al. report a slope of  $-0.82 \pm 0.12$ , again by fitting a power-law between  $0.3''$  and  $6''$ ; this power-law fits the star counts near  $6''$  but it is steeper than the points in the inner  $0.5''$ . We measure the slope only for the innermost points ( $< 0.5''$ ) where it is a constant and get a value of  $-0.62 \pm 0.06$ . If the same procedure is applied to Guhathakurta et al.’s profile, we get a shallower slope of  $-0.46$ .

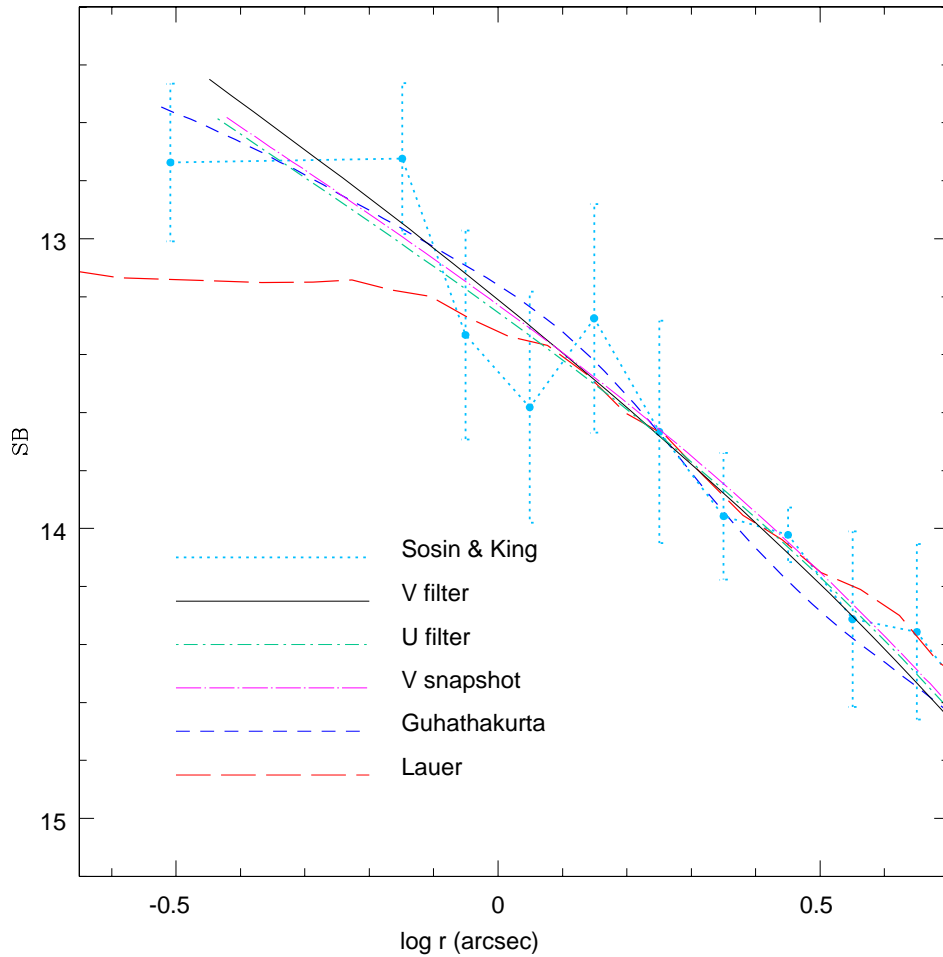


Figure 2.18 Surface brightness profiles for the central region of M15. Previously obtained profiles obtained by Guhathakurta (dashed dark blue), Sosin & King (dotted light blue) and Lauer et al. (long dashed red) are plotted with our results from various images: long exposure V image (solid black), long exposure U image (dotted -dashed green) and short exposure V (medium dashed magenta).

## 2.5 Summary

We obtain central surface brightness profiles for 38 galactic globular clusters from *HST*/WFPC2 images in various filters. Generally, we obtain reliable profiles into  $0.5''$ . Based on extensive simulations, we conclude that measuring integrated light with a robust statistical estimator is superior for estimation of the profiles compared to star counts when high signal to noise images are available. Profiles obtained from images taken with different filters are consistent and all are normalized to V-band by matching large radii results to profiles obtained from ground-based data.

When compared with previous ground based measurements, some of our profiles show different shapes for the inner regions. Most central surface brightness measured are brighter than previously reported with values up to two magnitudes brighter. The main reason for this difference is the increased spatial resolution of *HST*, but also because we use a non-parametric estimate as opposed to the traditional King model fits. The full distribution of central slopes is not consistent with that expected from evolution of isothermal cores. About half of our sample have a slope distribution consistent with King models (i.e. having a flat core) within our measurement uncertainties. The remaining 50%, however, have a distribution of surface brightness logarithmic slopes that are fairly uniformly distributed from  $-0.2$  to  $-0.8$ . Our direct deprojection of the SB profiles produces similar results for the luminosity density. About half of the sample have luminosity density logarithmic slopes that range from  $-0.4$  to  $-1.7$ .



Table 2.1. Milky Way Sample.

NGC	other name	filter	exp. time	image name	$\alpha$ center	$\delta$ center
104	47Tuc	F555	723	u5470112b	00:24:05.47	-72:04:52.16
1851	...	F439	1200	u2va0103b	05:14:06.95	-40:02:44.61
1904	M79	F555	306	u3ki0201b	05:24:11.03	-24:31:29.50
2298	...	F814	905	u3kt010gb	06:48:59.44	-36:00:19.52
2808	...	F555	314	u4fp0105b	09:12:03.09	-64:51:48.96
5272	M3	F555	1260	u4r00101b	13:42:11.33	28:22:37.81
5286	...	F555	530	u3um0201b	13:46:26.73	-51:22:28.77
5694	...	F555	310	u2y70105b	14:39:36.29	-26:32:20.19
5824	...	F555	320	u2y70205b	15:03:58.63	-33:04:05.59
5897	...	F555	608	u3kt0204b	15:17:24.50	-21:00:37.00*
5904	M5	F336	1200	u3ki0302b	15:18:33.36	02:04:55.19
6093	M80	F675	780	u3mu0104b	16:17:02.48	-22:58:33.18
6205	M13	F555	2056	u5bt0104b	16:41:41.05	36:27:36.19
6254	M10	F336	1500	u3ki0102b	16:57:08.9	-09:05:58.0*
6266	M62	F555	562	u67e0209b	17:01:12.96	-30:06:46.20
6284	...	F555	164	u2xx0302b	17:04:28.51	-24:45:53.54
6287	...	F555	3160	u37a0106b	17:05:09.13	-22:42:30.14
6293	...	F555	202	u2xx0202b	17:10:10.31	-26:34:57.77
6341	M92	F555	428	u2z50109b	17:17:07.34	43:08:10.08

Table 2.1 (cont'd)

NGC	other name	filter	exp. time	image name	$\alpha$ center	$\delta$ center
6333	M9	F555	2105	u28q030lb	17:19:11.26	-18:30:57.41
6352	...	F555	100	u2kl0205b	17:25:29.50	-48:25:19.65
6388	...	F336	1060	u63t0301b	17:36:17.18	-44:44:07.83
6397	...	F555	249	u33r010kb	17:40:41.57	-53:40:26.03
6441	...	F336	1060	u63t0401b	17:50:12.91	-37:03:06.67
6535	...	F555	1128	u3kt040gb	18:03:50.66	-00:17:53.03
6528	...	F555	814	u61v0101b	18:04:49.64	-30:03:22.55
6541	...	F555	596	u28q050hb	18:08:02.66	-43:42:52.92
6624	...	F555	1478	u28q0604b	18:23:40.22	-30:21:41.32
6626	M28	F555	1128	u3kt050gb	18:24:32.81	-24:52:11.20
6637	M69	F555	1690	u28q0704b	18:31:23.17	-32:20:54.59
6652	...	F555	1989	u3m8010ib	18:35:45.64	-32:59:26.99
6681	M70	F555	100	u24s0103t	18:43:12.83	-32:17:33.38
6712	...	F814	120	u2of0205t	18:53:04.30	-08:42:22.0*
6715	M54	F555	1850	u37ga40cb	18:55:03.29	-30:28:46.10
6752	...	F555	5246	u2hO010cb	19:10:52.237	-59:59:03.81
7078	M15	F555	400	u2hr0102b	21:29:58.40	12:10:00.26
7089	M2	F555	106	u67e0303b	21:33:27.00	-00:49:25.71
7099	M30	F555	1192	u5fw010nb	21:40:22.16	-23:10:47.64

Table 2.2. Measured parameters

NGC number	other name	$\mu_V(0)$ (mag/arcsec <sup>2</sup> )	$r_c$ (arcsec)	$r_b$ (arcsec)	SB slope logarithmic	error	LD slope logarithmic	error
104	47Tuc	14.35	20.9	16.4	0.00	0.04	0.11	0.15
1851	...	13.30	2.0	4.6	-0.38	0.11	-1.03	0.11
1904	M79	15.67	5.6	14.8	-0.03	0.07	-0.01	0.39
2298	...	18.72	16.3	17.4	0.00	0.07	<i>0.00</i>	...
2808	...	14.89	12.4	36.1	-0.06	0.07	-0.66	0.54
5272	M3	15.72	14.6	46.9	-0.05	0.10	-0.39	0.45
5286	...	15.19	4.2	25.1	-0.28	0.11	-1.17	0.30
5694	...	15.62	2.2	2.6	-0.19	0.11	-0.73	0.41
5824	...	14.17	1.4	4.0	-0.36	0.16	-1.11	0.36
5897	...	20.47	84.9	119.0	-0.04	0.03	<i>0.00</i>	...
5904	M5	16.13	25.7	18.1	0.05	0.07	<i>0.00</i>	...
6093	M80	14.56	4.5	6.1	-0.16	0.07	-0.77	0.28
6205	M13	16.41	34.4	79.4	-0.10	0.15	-0.71	0.32
6254	M10	17.68	43.4	22.4	0.05	0.07	<i>0.00</i>	...
6266	M62	14.78	6.6	13.8	-0.13	0.08	-0.74	0.40
6284	...	14.66	1.1	...	-0.55	0.14	-1.39	0.19

Table 2.2 (cont'd)

NGC number	other name	$\mu_V(0)$ (mag/arcsec <sup>2</sup> )	$r_c$ (arcsec)	$r_b$ (arcsec)	SB slope logarithmic	error	LD slope logarithmic	error
6287	...	18.32	11.3	34.4	0.00	0.07	-0.04	0.30
6293	...	14.43	1.0	...	-0.67	0.08	-1.27	0.18
6341	M92	15.29	11.0	17.15	-0.01	0.04	0.00	...
6333	M9	17.01	19.1	41.8	0.00	0.13	0.00	...
6352	...	18.31	23.2	24.0	0.02	0.17	0.00	...
6388	...	14.68	4.4	5.0	-0.13	0.07	-0.57	0.21
6397	...	15.29	3.7	2.7	-0.37	0.11	-1.16	0.20
6441	...	14.76	5.8	12.6	-0.02	0.12	-0.02	0.35
6535	...	19.35	1.7	21.2	-0.50	0.18	-1.28	0.38
6528	...	16.56	3.9	6.7	-0.10	0.14	-0.23	0.29
6541	...	14.38	2.0	...	-0.41	0.09	-1.32	0.22
6624	...	14.35	1.7	4.28	-0.32	0.16	-1.15	0.31
6626	M28	15.55	9.8	8.9	0.03	0.05	0.00	...
6637	M69	16.71	16.4	49.5	0.09	0.13	0.00	...
6652	...	13.93	1.2	0.7	-0.57	0.12	-1.44	0.20
6681	M70	13.68	1.1	...	-0.82	0.09	-1.75	0.10

Table 2.2 (cont'd)

NGC number	other name	$\mu_V(0)$ (mag/arcsec <sup>2</sup> )	$r_c$ (arcsec)	$r_b$ (arcsec)	SB slope logarithmic	error	LD slope logarithmic	error
6712	...	18.57	37.3	68.6	0.02	0.05	0.00	...
6715	M54	14.12	3.2	8.2	-0.12	0.07	-0.71	0.35
6752	...	14.56	6.53	3.2	-0.03	0.15	0.00	...
7078	M15	12.45	0.98	...	-0.66	0.11	-1.56	0.22
7089	M2	15.19	12.9	20.8	0.05	0.11	0.00	...
7099	M30	14.22	1.6	...	-0.57	0.11	-1.42	0.18

Note. — col 1-2 are NGC and other names, col 3 is central surface brightness in V, col 4 is core radius, col 5 is break radius (as defined on Section 2.3.4), col 6-7 are logarithmic central surface brightness slope and uncertainty, col 8-9 are logarithmic central luminosity density slope and uncertainty.

## Chapter 3

# Surface brightness Profiles for a sample of LMC, SMC and Fornax Dwarf galaxy Globular Clusters

### 3.1 Introduction

The observational study of internal dynamics of globular clusters (GCs) has benefited from imaging from space as well as enhanced spectroscopic capabilities in the ground. Noyola & Gebhardt (2006) (from now on called chapter 2) measured surface brightness profiles (SB) from *Hubble Space Telescope* (*HST*) images for a sample of 38 galactic globular clusters. The results from that work show that half of the objects in the sample are not consistent with having central flat cores, but instead, the distribution central surface brightness logarithmic slopes is continuous from  $-0.2$  to  $-0.8$ . The ages of the Galactic clusters are all confined to a narrow range older than  $\sim 10$  Gyr (Salaris & Weiss, 2002; De Angeli et al., 2005). It is desirable to measure central SB profiles of globular clusters with younger populations to find out if these central cusps are also observed in less evolved clusters. Globular clusters around Milky Way satellites are ideal targets for this task since they have a larger age range, they are relatively near, and most of them have been observed with *HST*.

Surface brightness profiles have been obtained for GCs in the Large Magellanic Cloud (LMC), Small Magellanic Cloud (SMC), and Fornax dwarf

galaxies in various studies using ground-based data. For the LMC clusters, star counts (Kontizas et al., 1987), aperture photometry (Mateo, 1987; Elson, 1991) and hybrid techniques (Elson et al., 1987) have been used to obtain surface density profiles for a variety of subgroups (rich, old, young, disk, and halo clusters). For the SMC clusters, only a few studies have measured density profiles from star counts (Kontizas & Kontizas, 1983; Kontizas et al., 1986). A couple of studies measured density profiles from aperture photometry for globular clusters around the Fornax dwarf galaxy (Smith et al., 1996; Rodgers & Roberts, 1994). All of these studies are very useful for studying SB profiles at large radius, but at small radius they suffer from the usual seeing and crowding problems associated with ground-based observations.

A large systematic study of surface brightness profiles obtained from space-based imaging was carried out by Mackey & Gilmore (2003b,a,c) (from now on collectively referred to as MAC03). They gathered a broad sample of LMC, SMC and Fornax galaxy GCs imaged with WFPC2. They obtained SB profiles by measuring star counts weighted by brightness from which they derived fundamental quantities like central density and core radius by fitting EFF profiles (Elson et al., 1987; Elson, 1991), which are power-law plus core profiles with three parameters: core radius, central surface brightness, and slope of the power-law. They determine that  $20\pm 7\%$  of the clusters in their sample are consistent with a post-core-collapse morphology, a similar number to the one found for Galactic clusters (Trager et al., 1995). When they compare their profiles with previous results obtained from ground based images, they find that important aspects of the nature of the profiles can be measured by improving the spatial resolution. McLaughlin & van der Marel (2005) (from now on called MVM05) combine the data from MAC03 with star count pro-

files from ground-based data in order to obtain a more accurate photometric normalization. They fit the re-normalized de-reddened resulting profiles with variety of models such as King fits (King, 1966), an alternate modified isothermal model by Wilson (1975), which has more extended envelopes than a King model, and a power-law plus core model like the one used in MAC03. They conclude that The Wilson fits provide the best description of the outer part of the clusters for both old and young populations.

Elson et al. (1989) and Elson (1992) found an interesting relation between core radii and age for a sample of LMC globular clusters in which the core radius seems to increase with ages between 1 Myr and 1 Gyr and then decreases again after that. Using *HST* data, de Grijs et al. (2002) explore the matter for a sample of rich LMC globular clusters and find that young clusters tend to have small core radii while older clusters have an increasingly large spread of core radii. MAC03 explored this relationship and found that the relation is also valid for globular clusters around other Milky Way satellites besides those in the LMC.

We concentrate in the central parts of the clusters because this is the region in which our technique has found differences in the SB shape when compared to profiles found by fitting parametric models containing flat cores (i.e. King (1966) models or other type of core profiles) for some clusters. Improving the measurements in this region and merging the results from our Galactic sample with those of this new sample, can help to understand the central region of globular clusters in order to understand their dynamical evolution. The LMC, SMC and Fornax galaxy globular cluster systems offer a unique window of opportunity to test if there are fundamental differences between systems due to their age.



## 3.2 Simulations

In chapter 2 we performed a large number of simulations in order to establish the best method for measuring surface brightness profiles from *HST* images and also to estimate the uncertainties of our measurements. Results from that paper indicate that the only way to measure reliable surface brightness profiles from integrated light is by using high signal to noise images. In order to evaluate how our findings for galactic GCs translate to clusters further away, we again perform extensive simulations, which we describe in detail in this section.

### 3.2.1 Image Construction

The way we create a simulated image is by adding synthetic stars on a background image using the task ADDSTAR in DAOPHOT (Stetson, 1987). The background image we use is a WFPC2 image of a very unpopulated field for which the few present stars have been cleanly subtracted. The input star lists are created in the same way as in chapter 2. With a given SB profile and a luminosity function, stars are generated randomly around a given center (the middle of the chip) following the two probability distributions, the surface brightness for radial distribution, and the luminosity function for the magnitude distribution. The supplied luminosity function comes from Jimenez & Padoan (1998) and it is corrected by the distance modulus of the LMC.

In chapter 2, we simulated SB profiles with the shape of various power laws. This gave us a good feel for our ability to recover a given central slope, but we could not test our ability to measure turnover radius. In order to better test our method this time we create a series of profiles formed by two power-laws joined at a break radius with a variable sharpness of break known as

Nuker profiles (Lauer et al., 1995). A Nuker profile is defined in the following way

$$I(r) = I_b 2^{\frac{(\beta-\gamma)}{\alpha}} \left(\frac{r}{r_b}\right)^{-\gamma} \left(1 + \left(\frac{r}{r_b}\right)^\alpha\right)^{\frac{(\gamma-\beta)}{\alpha}},$$

where  $r_b$  is the break radius,  $I_b$  is the surface brightness at the break radius,  $-\gamma$  is the asymptotic inner slope,  $-\beta$  is the asymptotic outer slope, and  $\alpha$  is the sharpness of break. By using these type of profiles we are capable of reproducing the characteristics of observed profiles for the sample. We create six different input profiles, whose parameters are summarized in Table 3.1. The radial extend of the simulated clusters is 400 pixels, which is equivalent to 18.4'' with the PC pixel scale (0.046 arcsec/pixel).

Once we have the input profiles we proceed to create multiple realizations of a given model including different numbers of stars. Using various DAOPHOT tasks we add synthetic stars onto the background image. We use as the input point spread function (PSF) the one calculated for the LMC cluster NGC 1835 with a PSF radius of 9 pixels. Judging by the number of found stars in the real data, we create images with three different amounts of input stars: 200,000 input stars, which yields  $\sim 10,000$  found stars; 50,000 input stars, giving  $\sim 6,000$  detected stars; and 10,000 input stars, for which we find  $\sim 2,000$  stars. The vast majority of the real clusters in the sample are comparable to the first two cases. The different realizations have the exact same input parameters but come from different, non-overlapping star lists. We create 10 realizations for the 200,000 input stars case, and 20 for the other two. It is worth noting that the number of found stars decreases with increasing input central slope for the same number of input stars. For the steepest central slope  $\sim 8,000$  stars are found compared to the  $\sim 10,000$  for the zero central

slope cases. To avoid confusion, we always refer to the simulated datasets by the number of input stars rather than the number of found stars.

### **3.2.2 Center Determination**

Having an accurate measure of the center is a key step to measuring an accurate density profile. Our technique for finding the center of a cluster is described in detail on chapter 2. We take a guess center, divide the image in eight sectors converging at that center, count the stars in each sector and calculate the standard deviation of those eight numbers. We change to a different guess center and perform the same operation. In the end we have a grid of guess centers with a standard deviation value associated to them. We fit a surface using a spline smoothing technique (Wahba, 1980; Bates et al., 1986) and choose the minimum of this surface as our center.

We test the accuracy of our center determination technique by applying it to these simulated images. Figure 3.1 shows the average measured center and the standard deviation of the measurements for different groups of simulations. The maximum deviation observed is of  $\sim 7$  pixels, which is equivalent to  $\sim 0.3''$ . These results are better than those in chapter 2. We believe the reason for this is that there are more stars enclosed in the same projected radius due to the distance difference, therefore the center estimation is improved.

### **3.2.3 Surface Brightness Profiles**

We compare the results of measuring the density profile from integrated light versus doing it using star counts. We refer the reader to the detailed discussion in section 2.4.1 about the strengths and weaknesses of each method. Results from that paper indicate that using a robust estimator to calculate

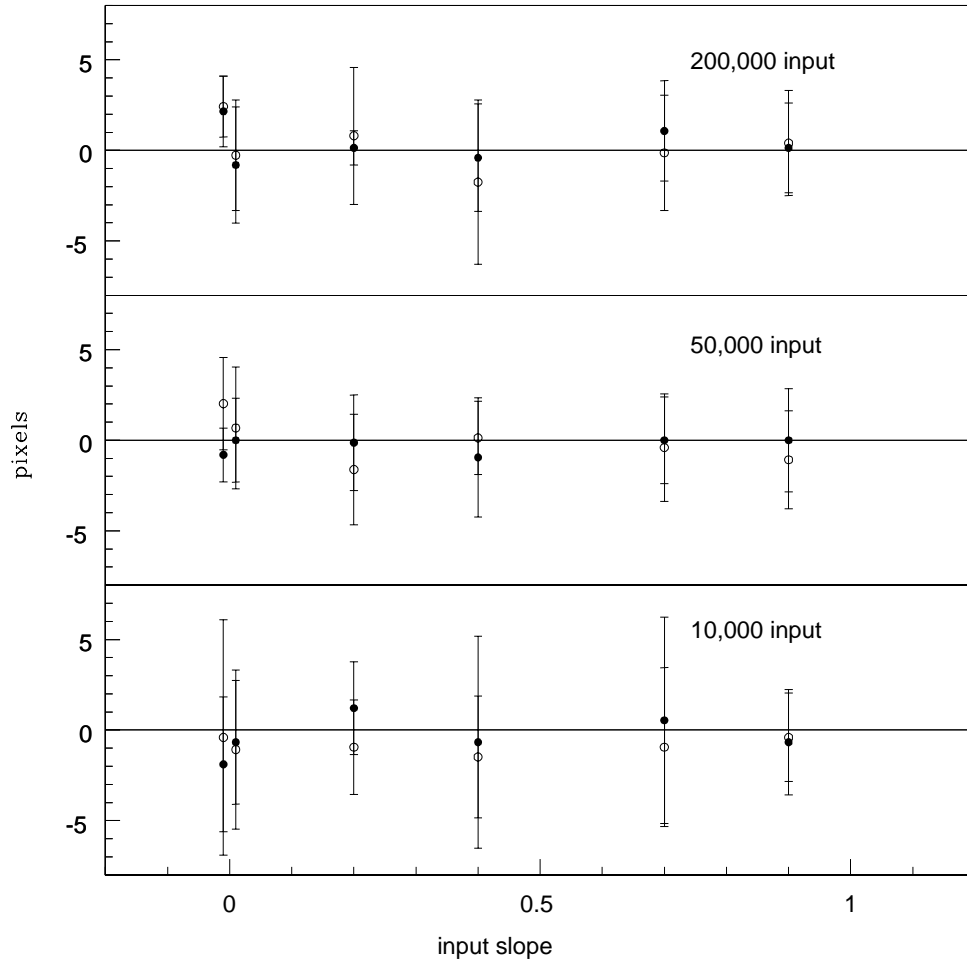


Figure 3.1 Comparison between the measured and input center for every set of simulations with different central slopes. The average distance between the actual and measured center is shown for the  $x$  (solid points) and  $y$  (open points) coordinates in pixels. A small horizontal offset is introduced for clarity for the two cases with central zero slope. Error bars are the standard deviation of the individual measurements for each case. Each PC pixel is  $0.046''$ .

the number of counts per pixel in a given area is the best way to recover the central part of the profile. For that reason we use the same robust estimator, the biweight (Beers et al., 1990), for our measurements in this work.

We measure the brightness of stars as well as their location from the constructed images. We use a series of DAOPHOT tasks to find stars and perform PSF fitting photometry with the same PSF that we used to construct the images. Since Poisson noise was included when constructing the images, this does not make the subtraction perfect. The process produces an image where all the stars have been subtracted and only the background light remains. We call these images ‘subtracted’, while we refer to the original unsubtracted image as ‘full’. We measure a surface brightness profile in concentric annuli from the center of the cluster by calculating the biweight of the counts in an annulus and dividing by the number of pixels. We use two sets of annuli for these measurements. The first set goes from 1 to 25 pixels in steps of 4 – 6 pixels, and the second set goes from 20 to 100 in steps of 20 pixels. The assigned radius of a given annulus is the average between the inner and outer radii. In chapter 2 we note that, for the input profiles with steep cusps, the subtracted images produce a flatter central profile than the input. This is because crowding produces and over subtraction after the PSF fitting process. As done in chapter 2, we decide to produce alternative images with only the 10% brightest stars PSF subtracted and an image where we mask the 2% brightest stars with a radius of 3 pixels to try to avoid the over subtraction problem.

Once we have the catalog of found stars we can compare it to the original input list and estimate how many of the input stars are found for different magnitude a radial bins. For the cases with 200,000 input stars We find that bright stars are found with an efficiency higher than 100%, meaning

that more stars are found to be in the brightest magnitude bin than the number of stars that were input for that same magnitude bin. This effect is more pronounced in the central part of the cluster, where crowding problems are worse. The effect is easy to explain since one or more faint stars are likely to fall within the PSF disk of the bright stars and their light is measured as if it was part of the bright stars. The difference between input and measured magnitudes is typically  $\sim 0.1$  mag, which is enough to make a number of stars from a fainter magnitude bin be measured in a brighter one. For intermediate-magnitude stars, the same effect happens, for the regions in and around the core; the efficiency for finding these stars falls to 50 – 70% depending on the case. The efficiency for finding the fainter stars is lower in any radial bin; it is a few percent in the center and up to 50% for the regions at large radii. As expected, these numbers become more extreme for the cases with steeper central slopes, since crowding is worse then. For the case with 50,000 input stars, the trends are similar, but the numbers are less extreme. Stars in the brightest magnitude bin are found with an efficiency close to 100% for the cases with flatter central slopes. The efficiencies for the cases with steeper central slopes are very similar to those with 200,000 input stars. Finally, for the cases with 10,000 input stars. The efficiencies for finding the input stars are all close to 100% except for the faintest stars in the central region of the cluster, which go from 70 – 80% depending on how steep the central slope is. The conclusion from this analysis is that when correction factors are calculated for star count measurements, the factors are dependent on the shape of the density profile and the number of existing stars. If one assumes the wrong shape or the wrong number of stars in the cluster, the correction factors will be wrong.

Stars are counted in and divided by the area of each annulus. The above discussion about the efficiency for finding stars suggests that the stars below a certain brightness are never found with 100% efficiency, therefore we exclude them from the star lists. We compare the obtained star count profiles with those obtained by measuring integrated light from the four different images (full, subtracted, 10% subtracted and 2% masked). Results from these measurements are shown in Figure 3.2 for the 200,000 input stars case and Figure 3.3 for the 50,000 input case. In both figures we are showing models 1, 4, and 5, which have central slopes of 0,  $-0.4$  and  $-0.7$  respectively. We find that, depending on the shape of the input model, the profile measured in the subtracted, partially subtracted, or masked images follow the input profile best. For the least concentrated cases, the measurements from the subtracted and 10% subtracted image seem to follow the profile best, but for the more concentrated cases, the subtracted and 10% subtracted cases tend to look flatter in the center than the input profile. For these cases, the profile from the masked image seems to be a better choice. The star counts profiles are always much noisier than the light profiles in the central regions and they show a consistent bias in the central regions for the cases with steep central slopes.

We test how well we recover the input central slope for the different shapes of input profiles and for the different measurement methods. Since we measure the central slope by taking a first derivative of the profile we need a smooth version of it. For this, we apply the one dimensional version of the spline smoother mentioned in section 3.2.2. This allows us to recover information from the profile without fitting any parametric model to the data. We exclude the star count profiles from these measurements because the central parts of the profiles are too noisy for the spline smoother to get a reasonable

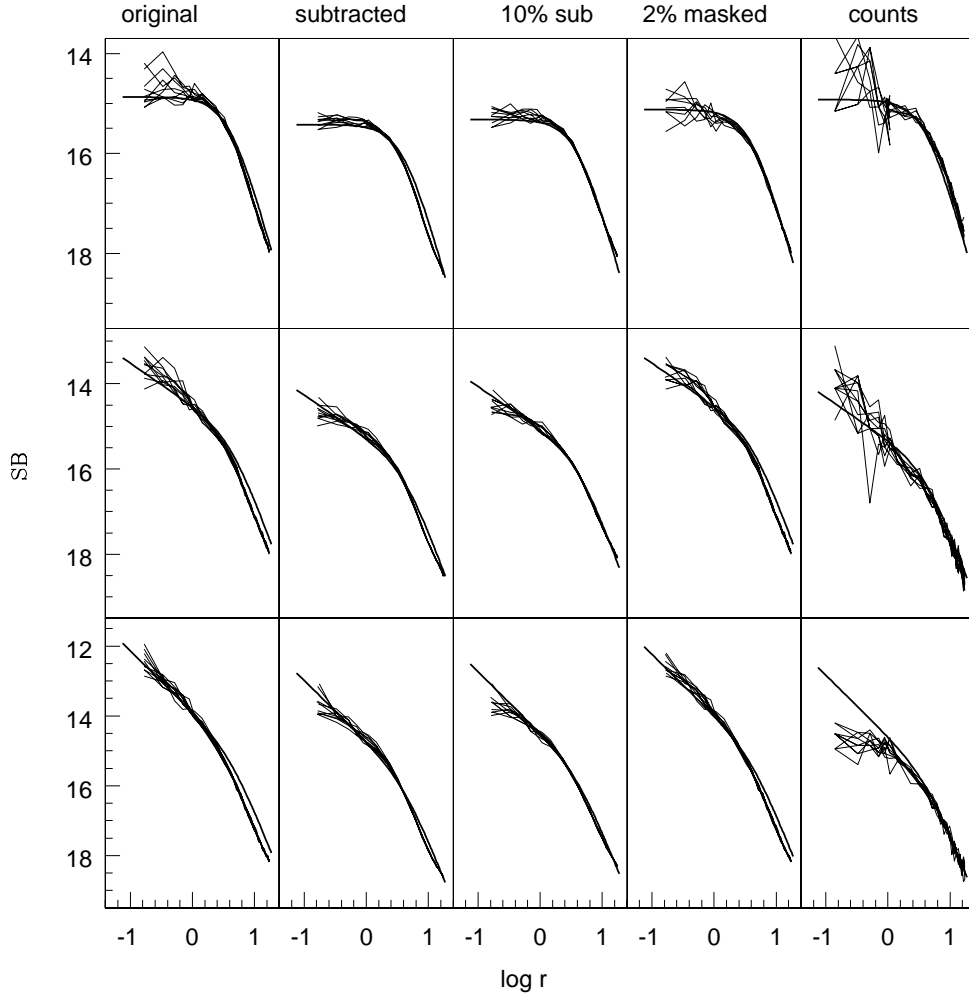


Figure 3.2 Surface brightness profiles for three groups of simulations with 200,000 input stars. For each case (models 1, 4, and 5) the measurements from individual realizations (thin lines) are plotted against the input profile (thick solid line). The profiles are measured from four different images: full, subtracted, 10% brightest stars subtracted and 3% brightest stars masked, and also from star counts. The vertical axis is on an arbitrary magnitude scale.



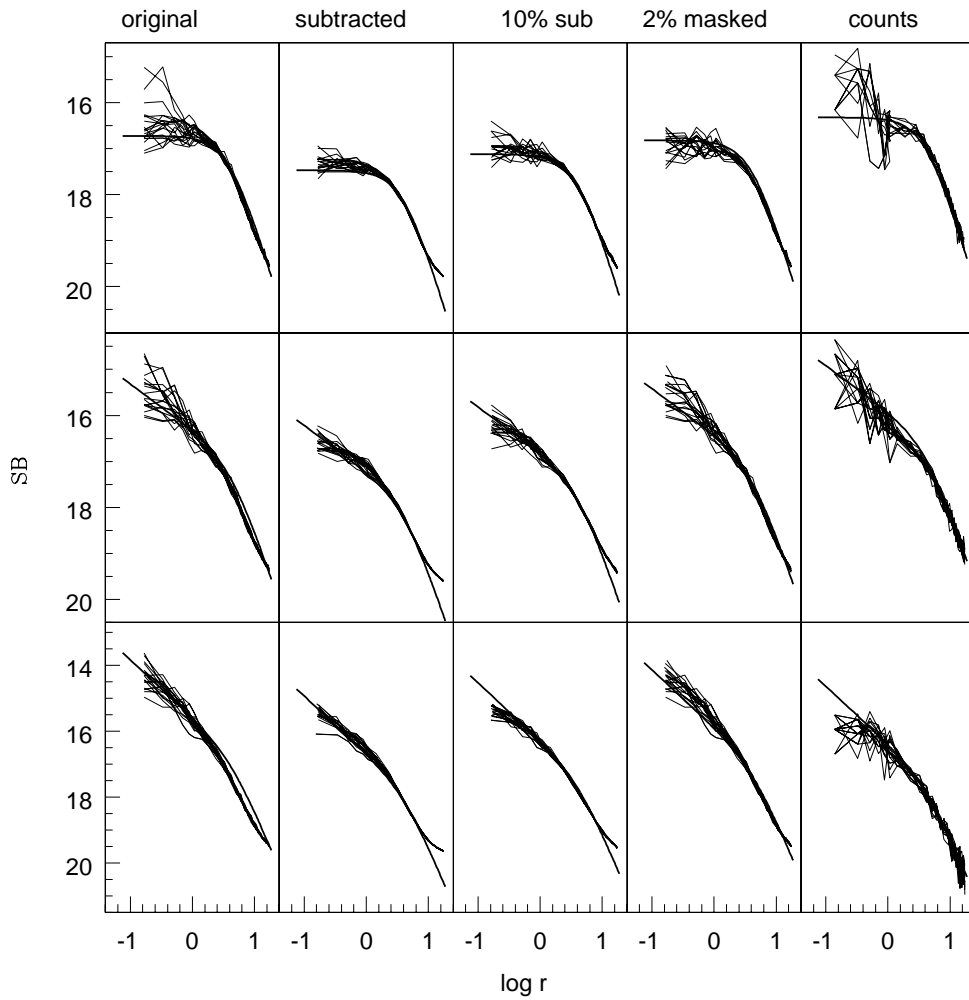


Figure 3.3 Same as previous figure but for simulations with 50,000 input stars.

profile. The first derivative of the smooth profile shows a section toward the center where it is constant; we take this constant value as the measured central slope. After measuring the central slope for the different realizations, we calculate the average and the standard deviation for each case. We show the input versus measured central slopes in Figure 3.4.

We observe that the uncertainty on the slope measurements increases as the number of input stars decreases. For the 10,000 input stars case, the profiles from the subtracted and 10% subtracted images yield smaller uncertainties. These two cases tend to underestimate the central slopes for the concentrated and rich (200,000 and 50,000 input stars) cases, while the slopes recovered from the masked images seem to follow the input better. For all the rich cases, the measurements for the model with the steepest central slope overestimate the slope, we think this can be due to the fact that so many stars are being input at the center that not enough stars are being input for the outer parts, which would explain the fact that we find fewer stars for this case.

We test our ability to measure the input break radius by measuring the minimum of the second derivative, which is the radius at which the curvature is maximum. Our results show that we can measure the break radii for the simulated clusters to within 10% accuracy. The majority (all except two) of the observed clusters have a reported core radius larger than the one for our simulations, so we are confident that we can measure such break radii.

### 3.2.4 Uncertainties

We refer the reader to the detailed discussion in section 2.2.4 of chapter 2 about the sources for uncertainty when measuring surface density profiles from integrated light versus measuring it from star counts. In order to prop-

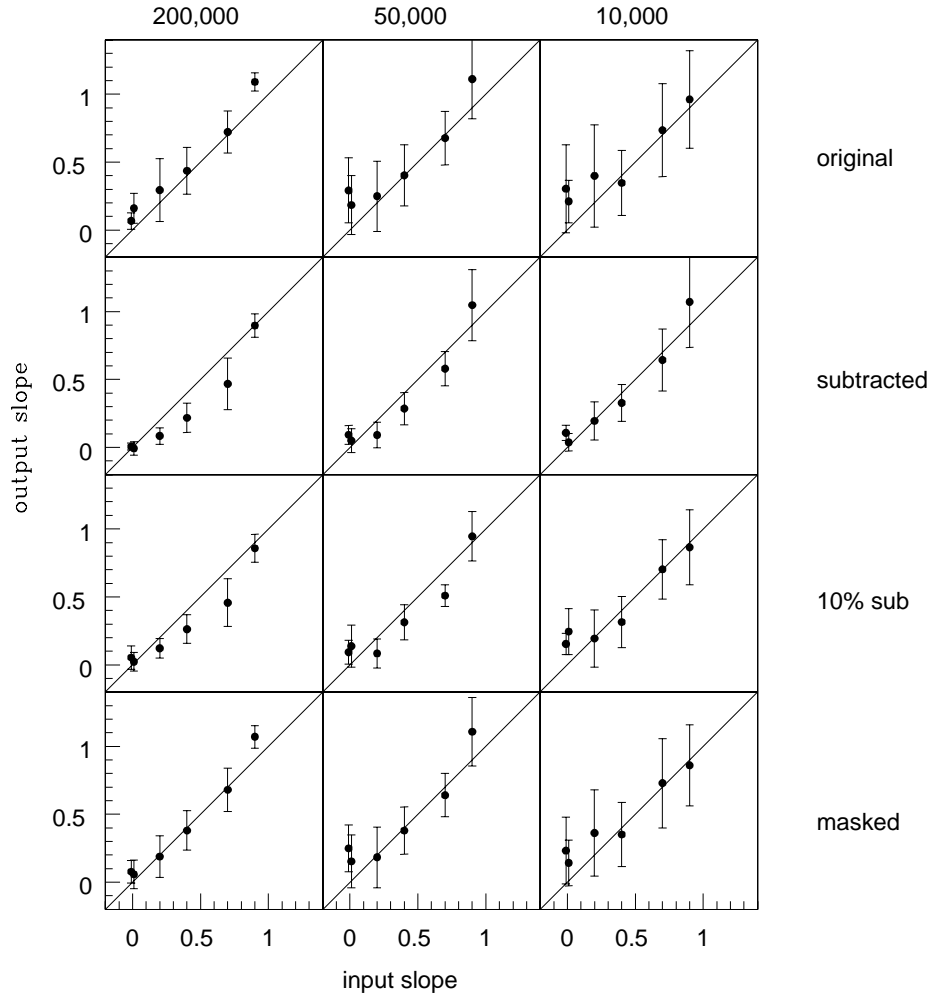


Figure 3.4 Input versus measured surface brightness slope for the different groups of simulations. A small horizontal offset is introduced for clarity in the case of the two models with central zero slopes. We show the average measured slope of the individual profiles for each case. Error bars represent one standard deviation for all the measurements.

erly estimate our uncertainties, we compare the photometric scatter between different realizations having identical input parameters with the biweight scatter estimate. In chapter 2 we find that the biweight scatter has to be scaled in order to match the photometric scatter measured from the different realizations. For these new simulations we find that the scaling factors change due to the differences in our input shapes and of simulating clusters at larger distances (the number of stars on a given annulus and differences in PSF). As done in chapter 2, we compare these scaling factors with those obtained for real data from an alternative method discussed in section 3.3.5.

We also estimate the error in our central slope measurements by comparing the scatter of measured slopes with the known input slope for every simulated cluster. The results are shown in Fig 3.4. We confirm what we learned from analyzing Figs 3.2 and 3.3. The slope uncertainties are smaller for the subtracted and partially subtracted cases, but they are biased low for the cases with steep cusps and large number of input stars. Also, the slope measurements are more uncertain for the clusters with 10,000 input stars. The figure suggests to take the measurements from the masked image for the cases with steep central profiles and the subtracted or 10% subtracted for the others. In the case of 10,000 input stars, the subtracted case always seems to be better and not biased.

### **3.3 Data and Analysis**

#### **3.3.1 Sample**

As mentioned in chapter 2, there are minimum requirements for an image to be suitable for measurements with our technique. The image needs to have a minimum number of counts, which we can obtain by having a large

number of stars present due to richness, high concentration, or by having long exposure times. We established that detecting stars six magnitudes fainter than the horizontal branch with a signal to noise of 20 is a minimum requirement for low-concentration clusters. This criterion can be relaxed for highly concentrated clusters and for those with a large number of stars ( $M_V < -7.5$ ). Taking into account these requirements, we gather 30 clusters from the *HST* archive. The sample contains 21 clusters in the LMC, 5 in the SMC and 4 in the Fornax dwarf galaxy. When images are available in two filters (F555W and F814W), we align and combine the images in order to improve signal to noise. We believe we are justified in doing this because the color gradients for the radial range that we are measuring are smaller than the photometric uncertainties. If no alternative image is available, we use the single F555W dataset. In general we analyze only the chip in which the center of the cluster lies, the only exception is the cluster Kron 3, for which we use all four chips. The size of one WFPC2 chip is large enough to contain a few core radii for every cluster in the sample. The scale of the CCD is  $0.1''/\text{pixel}$  for the WF chips and  $0.046''/\text{pixel}$  for the PC chip.

We use the WFPC2 associations from the Canadian Astronomy Data Center website<sup>1</sup>. These images are spatial associations of WFPC2 images of a given target. The raw data frames are processed through a standard reduction pipeline, grouped in associations and combined. The available data are a multi-group image with frames for the three WF and the PC chips. It is straightforward to align and combine two of these images from different filters if they belong to the same program, which is the case for every object with two images available in our sample.

---

<sup>1</sup><http://cadwww.dao.nrc.ca/>

### 3.3.2 Image Processing

We process the data in the same way we do for the simulated images. We choose the frame where the cluster center is located, this is usually the PC frame, but for a few cases, it is one of the WF frames. We trim the image in order to eliminate the noisy edges and then proceed to perform basic photometry with various DAOPHOT tasks. First, we use the “FIND” task to make a preliminary list of detected stars, then we perform aperture photometry with the task “PHOT” in order to choose candidates for PSF construction. We find that PSF stars have to be chosen by hand because a single bad PSF star can have an important effect in the PSF construction. Once we have a list of PSF stars, we perform an iterative procedure in which we subtract the neighbor stars to the PSF stars and then recalculate the PSF. In this way, the PSF construction is less affected by crowding. Using the final constructed PSF we subtract all the stars from the image, leaving behind an image containing only background light. We also create an image with the brightest 10% stars subtracted and another one with the brightest  $\sim 2\%$  stars masked.

Some of the data frames contain a small number (2 to 6) of very bright stars that appear saturated in the images. These bright stars are found at various locations on the image, but the closer they are to the center, the larger the effect they can have on our measurements by creating bumps in the profile. We decide to exclude these stars from our measurements by masking them with a larger masking radius than the one used for the 2% brightest stars. The clusters for which this extra step was taken are NGC 1818, NGC 1984, NGC 2100, NGC 2214, and NGC 330.

### 3.3.3 Center

As discussed in chapter 2, it is crucial to measure the center of the cluster accurately in order to measure a reliable surface brightness profile. We use the method outlined in section 3.2.2. Many clusters in the LMC are known to have an elliptical shape. Our method is not affected by this as long as the cluster is symmetric in two dimensions. The first guess center is always chosen by eye, and the radius for counting stars is chosen so that the circle lies entirely inside the image, therefore, it is larger if the center is closer to the middle of the chip. For one cluster (NGC 1868), the center of the cluster is very near the edge of one of the chips. In this case, we calculate the center from a different image with lower exposure time, but with the center located in the middle of the chip. We report our measured centers in table 3.2. We warn the reader that special care should be taken when using these coordinates. These centers are valid only using the world coordinate system (WCS) information contained in the header of each image. The WCS information for two different images can make the coordinates for same location vary by a few arcsec. The center is always measured on the primary dataset (the F555W image) when two images were combined.

### 3.3.4 Surface Brightness Profiles

Once we have measured a center, we calculate the surface brightness profile from the four different images of each cluster. We calculate surface brightness by estimating the biweight (as explained in section 3.2.3) of the number of counts per unit area in a series of concentric annuli. The choice of the size of annuli in which we measure the profile is given by a trade off between spatial resolution and noise. For images with very high signal to noise,

we can use smaller steps, while for more sparse cases, smoother profiles are obtained by increasing the size of the bins at the cost of decreasing the spatial resolution. We use three different sets of annuli, the first one goes from 1-25 pixels with steps of 4-6; the second goes from 20-100 pixels with steps of 12-15; and the third one from 100-380 pixels with steps of 40-60.

In section 3.2.3 we observe that for the simulated images the star counts profile tends to underestimate the profile at the center and it is noisier than the integrated light profile. For this reason, we decide not to calculate the star count profiles for these datasets. Also, we observe that the profiles coming from the unsubtracted image are always noisier than those obtained from the other images, so we never use the ‘full’ profile as our final result. For every set of simulations, the subtracted and 10% subtracted images always yield smoother profiles, unfortunately they show to be biased toward the center for the profiles with central slopes different than zero, so we can only use them when all four profiles are consistent with a central flat profile. If there are systematic differences between the original and masked profiles and the two subtracted ones in the sense that the first two are steeper than the latter two, then we use the profile from the masked image, since this is the one that traces the central cusp best.

In chapter 2 we find the photometric zero point by integrating our measured light profiles and comparing them to previously obtained profiles from ground based data. We cannot do the same thing here because our profiles have a smaller radial extent. For the cases in which our central profile differs significantly from previous measurements, the radial extent in which the two profiles agree is not large enough for us to make a meaningful comparison of enclosed light. We also observe that the differences in shape between our



measurements and those obtained by MAC03 are always inside the turnover radius. We therefore use the data points outside the core radius to normalize our profiles to the EFF fits by MVM05. We choose to normalize to these profiles because MVM05 use the MAC03 photometric points, but they re-normalized them using ground based data and they correct for reddening. This brings all our measurements to a common scale on  $V_{mag}/\text{arcsec}^2$ .

We want to make measurements of central and outer slopes, but our images are radially limited, so we construct radially extended profiles by using our measured profile inside  $\sim 10''$  and the MVM05 EFF fits outside that radius. We measure slopes by taking a first derivative of the profiles, which requires a smooth version of the profiles since noise is greatly amplified when taking derivatives. The smoothing is done by using the one dimensional spline mentioned in section 3.2.3 (Wahba & Wang, 1990). For most profiles, there is a region in the center for which the first derivative is constant. We take this value as the central slope. For the clusters that show a steep central cusps, the slope sometimes changes through the entire radial range. In this case we take the central most value of the derivative as the inner slope. Since we use EFF fits at large radius, we expect the first derivative to reach a constant value outside. The measured value is expected to coincide with the slope of the power-law for the EFF fits, which it indeed does. We take the value of the first derivative at the half-light radius as the outer slope. It is worth noting that the measured outer slope will be very different to that measured for Galactic clusters, since the profiles for those clusters are calculated from a King fit, which does not have a constant outer slope.

We deproject the profiles after smoothing in order to obtain a luminosity density (LD) profile for each cluster. For the clusters with flat central

profiles we often cannot obtain a proper deprojection due to noise, because the noise sometimes makes the central points be slightly fainter than the rest, which produces a positive slope in the smooth profile and that cannot be deprojected numerically. For the cases in which we do obtain a proper deprojection, we measure the central slope of the LD distribution in the same way as we measure the central SB slope, by taking a first derivative.

The traditional measurement of core radius as the radius for which the central luminosity value falls by half loses meaning when the central slope is not zero. If the central profile shows a cusp, then the core radius will be resolution-dependent. For this reason, we decide to measure what we call a break radius instead. The break radius is defined as the radius of maximum curvature, the one in which the second derivative reaches a minimum. This is a more systematic measure for a set of non-parametric profiles with different central slopes. Even after applying the smoothing procedure, there is still a certain amount of noise present in the second derivative, for this reason, we fit a high order polynomial and take the minimum of the fit instead of the minimum of the second derivative as our break radius. In chapter 2 we find that the core and break radius coincide for the clusters having a flat core, but they do not coincide for the cases presenting a cusp.

The difference in shape from our measurements and the parametric fits will affect the measurement of the half light radius. Since we are using EFF fits for the outer part, and these fits are formally infinite, we have to truncate them in order to measure the total enclosed light. We use the tidal radius measured by MVM05 as a truncation radius and measure the half light radius for our smooth profiles. Having an estimate of the total luminosity and using the M/L values calculated by MVM05 we can estimate the total mass of each

cluster and thus estimate the median relaxation time as described in Binney & Tremaine (1987)

$$t_{rh} = \frac{2.06 \times 10^6}{\ln(0.4M_t/\langle m \rangle)} \langle m \rangle^{-1} M_t^{1/2} r_h^{3/2}.$$

We assume a mean mass of  $0.5M_\odot$  as in MVM05. Results from these calculations are presented in table 3.3.

### 3.3.5 Data Uncertainties

We describe how we estimate uncertainties for the simulations in section 3.2.4. The method is based on different realizations for which shot noise from stars can be estimated directly. We use an alternative method to calculate the uncertainties for real data and we calibrate this method against that used for the simulations, as we did in chapter 2. We assume a smooth underlying stellar radial profile, so the uncertainties of the photometric points should reflect deviations from a smooth curve in a statistically meaningful way (i.e., have a Gaussian distribution around the mean value). We calculate the root mean square (RMS) difference between the smooth profile and the data points for the central region. The biweight yields an estimate for the central location (SB value) and scale (scatter); this scale value is divided by the square root of the number of sampled pixels and used as the initial uncertainty for individual photometric points. We then calculate the ratio of the biweight to the RMS, which should represent our lack of inclusion of shot noise from the stars. This ratio depends on the extent of the radial bins (i.e, the number of pixels used), therefore we use two different scalings for the different binning. We estimate this scale for the simulations using the different realizations, in order to make sure that these two scalings coincide. The average scaling for the inner points

is about 3 and about 10 for the outer points. These numbers are consistent with what we found in the simulations. Thus, we are effectively including shot noise from stars. The largest scalings occur for sparse clusters, as expected.

In the same way as in chapter 2, we calculate the uncertainties on slope measurements from a bootstrap technique. The bootstrap approach follows that in Gebhardt et al. (1996). From the initial smooth profile, a new profile is created by generating random values from a Gaussian distribution with the mean given by the initial profile and the standard deviation from the photometric uncertainties. A hundred profiles are generated in this way and the 16 – 84% quartiles are measured for the errors. These estimated errors are compared with the scatter measured for the simulated cases in fig 3.4 and the two independent error measurements agree quite well, which gives us the confidence that the uncertainties calculated with the bootstrap method are reliable. In chapter 2 we perform one more check on our slope uncertainties by measuring the effect of increasing the uncertainties on photometric points by a factor of two. From the bootstrap method, we find that the slope uncertainties increased by a modest factor, less than two, for most clusters. Thus, the slope uncertainties are not too sensitive to individual photometric errors.

## **3.4 Results and Discussion**

### **3.4.1 Surface Brightness**

The measured surface brightness profiles for the entire sample are shown in figs 3.5 to 3.9. For each cluster we show our normalized photometric points with error bars, and a smooth profile made from the combination of our photometric points inside  $\sim 10''$  and MVM05 EFF fits outside that radius. For comparison we show the MVM05 EFF fit and the central photometric point

used for that fit. We would like to stress that the photometric points at radii larger than  $\sim 10''$  do not participate in the construction of the smooth fit, instead the EFF fits are used in that region. For about half the sample (17 objects), the agreement between our measurements and the EFF fits of MVM05 is excellent, even for those cases in which the central photometric point by MAC03 is barely inside the turnover radius (such as Fornax 2) or it does not lie on top of the EFF fit (such as NGC 1651, NGC 1898, or 2100). There is only one case (NGC 1754) for which our photometric points are fainter than the EFF fit. For the remaining 12 objects, our photometric points are brighter than the EFF fit by more than  $0.5 \text{ mag/arcsec}^2$ , with three objects (NGC 2019, R136, and Fornax 3) having differences larger than  $2 \text{ mag/arcsec}^2$ .

MAC03 identify a few clusters that they think agree with the expected post core-collapse (PCC) morphology by showing a power-law cusp in their central profile. NGC 2005 and NGC 2019 are identified as clear cases of PCC morphology with central power-law slopes of  $-0.75$ . NGC 1835 and NGC 1898 are marked as good candidates for PCC morphology, but they measure lower power-law slopes of  $-0.45$  and  $-0.30$  for them. Three more clusters, NGC 1754, NGC 1786, and NGC 1916 have incomplete profiles and are classified as intriguing due to their small cores, but are not placed as firm PCC candidates. Fornax 5 is also considered a good candidate for a PCC cluster based on its small core and central profile shape. Our results for these seven clusters confirm the presence of a steep cusp for NGC 2005, NGC 2019, and NGC 1916; and a shallow cusp for NGC 1786. The rest of the cases all show flat central cores. Our reported values of the central slopes are different from the power-law slopes of MAC03, this makes sense since they are fitting a power-law to photometric points on a larger radial range than that

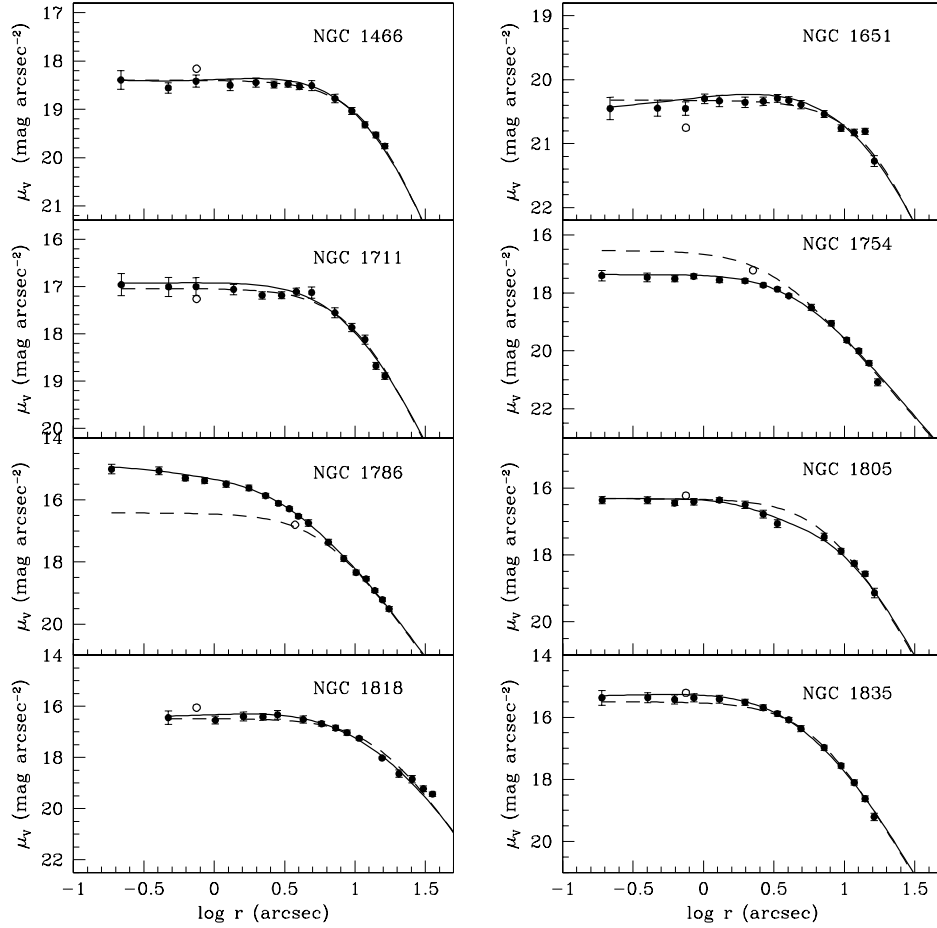


Figure 3.5 Surface brightness profiles for the LMC clusters. For each cluster we show our photometric measurements (solid points), our smooth profile (solid line), and the EFF fit by MVM05 (dotted line). The smooth profile comes from a fit to our photometric points inside  $\sim 10''$  and the EFF fit outside that region. For every panel the SB units are  $V \text{ mag/arcsec}^2$ .

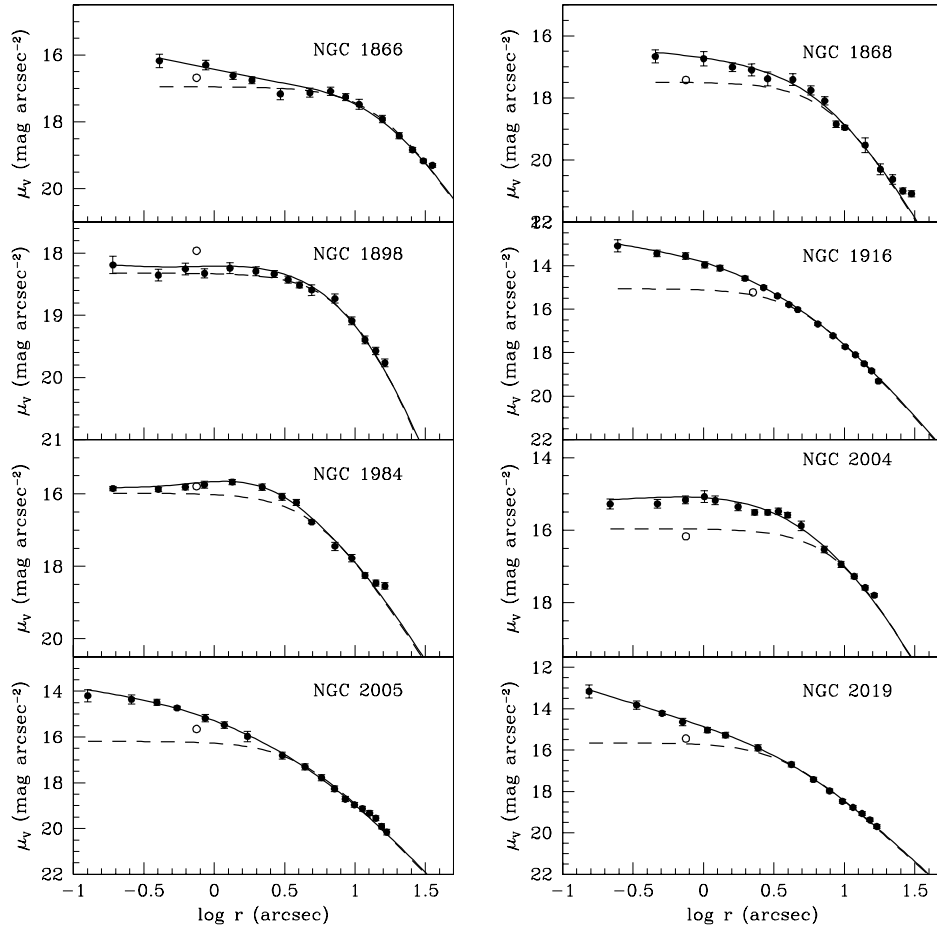


Figure 3.6 SB profiles continued.

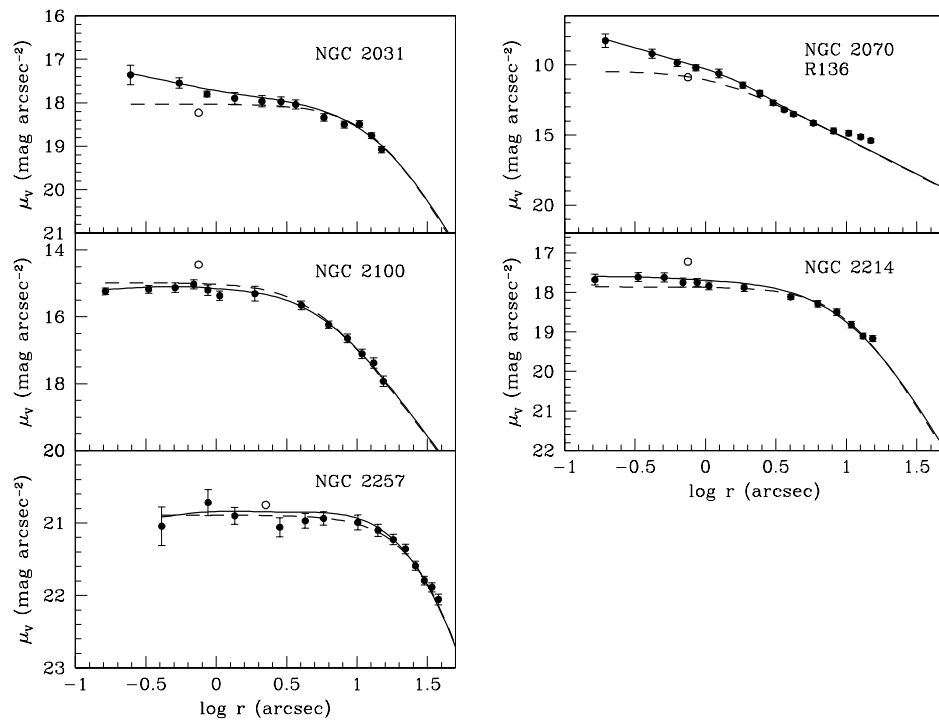


Figure 3.7 SB profiles continued.



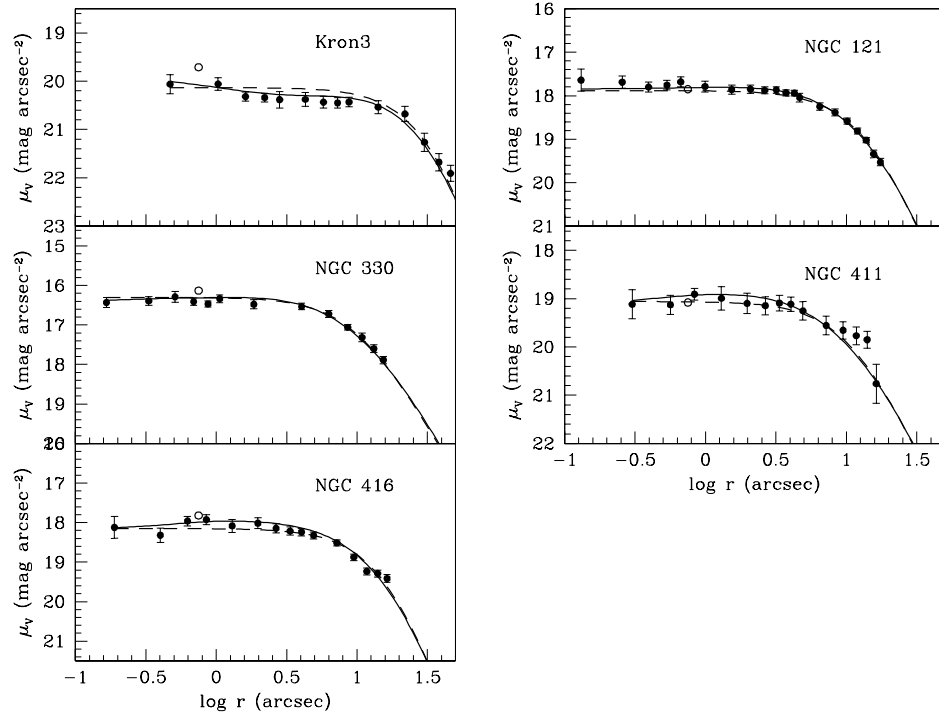


Figure 3.8 The same as in Fig 3.5 for the SMC clusters.

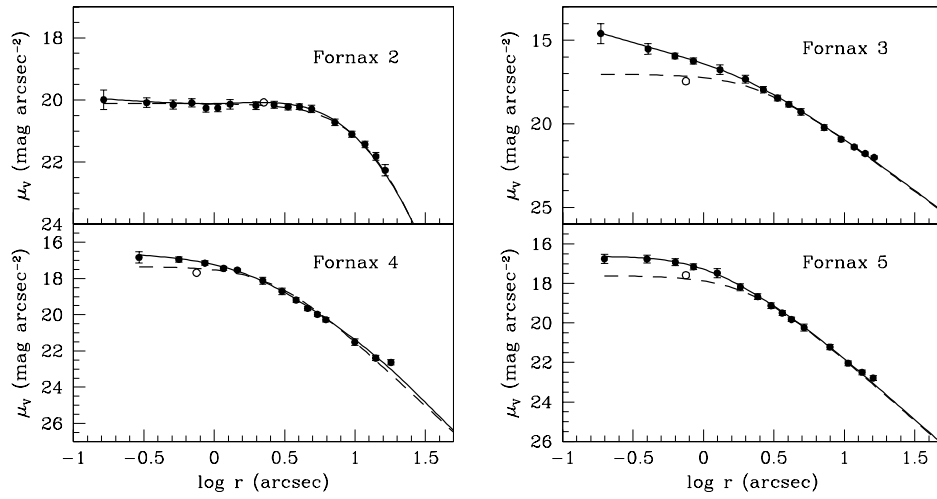


Figure 3.9 The same as in Fig 3.5 for the Fornax dwarf galaxy clusters.

in which we are measuring central slopes. We identify a few more clusters as having clear central cusps (with central slopes steeper than  $-0.20$ ) such as NGC 1866, NGC 2031, Fornax 3 and Fornax 4, and some showing shallow cusps (with central slopes flatter than  $-0.20$ ) such as NGC 1868, NGC 2214, and Fornax 2. When the luminosity density central slopes are taken into account, a similar classification arises, NGC 1866, NGC 1916, NGC 2005, NGC 2019, and Fornax 3 have steep cusps with LD logarithmic slopes steeper than  $-1.00$ , while NGC 1754, NGC 1868, NGC 2031, and Fornax 4 show shallow cusps with slopes between  $-0.2$  and  $-1.0$ . The cluster R136 is discussed in a separate section (3.4.2).

### 3.4.2 R136

R136 is known to be an extremely young object at the center of the 30 Doradus nebula in the LMC. It is considered to be a young version of a globular cluster due to its large content of O type stars. Main sequence star with masses as high as  $120M_{\odot}$  have been detected in it (Massey & Hunter, 1998). The estimated age for the most massive stars is  $< 1 - 2$  Myr and the mass function agrees very well with a Salpeter initial mass function (IMF). This makes R136 a unique and very peculiar object because it allows us to study star clusters in the way they looked just after formation. The surface brightness profile that we measure has a logarithmic central slope that is steeper than anything measured before for a globular cluster and steeper than anything predicted by dynamical models like core-collapse. This makes us suspect that we are not resolving a core or a turnover radius for this object and that our central slope measurement corresponds to the slope just outside the turnover radius for the other objects. We decide to include R136 in every systematic measure we

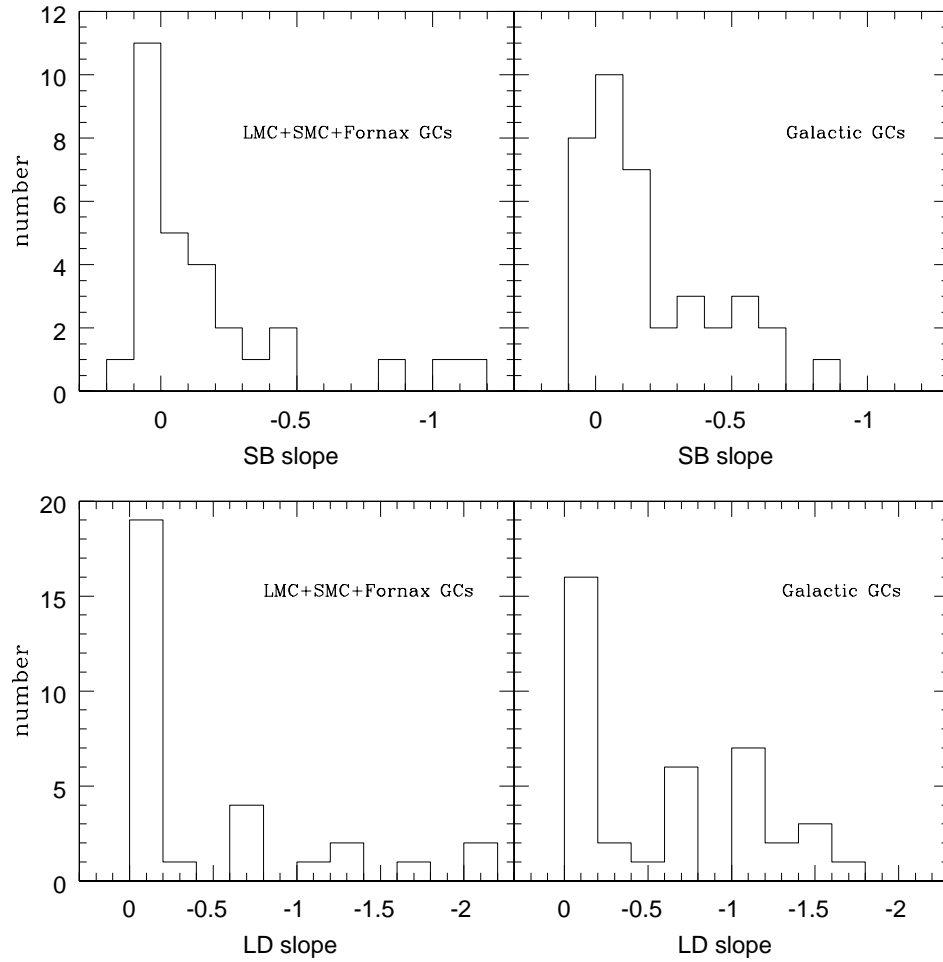


Figure 3.10 Histograms for surface brightness (top) and luminosity density (bottom) central logarithmic slopes for the LMC+SMC+Fornax sample (left panel) and the Galactic sample (right panel).

made for other clusters, but we caution the reader that its location in different distributions, particularly those dealing with central SB slope, should be taken with a grain of salt for this reason. The central surface brightness value for this object implies a central density of  $8 \times 10^6 M_{\odot}/pc^3$ .

### 3.4.3 Combining Two Samples

In order to explore possible correlations between physical quantities, we combine the results for this sample with those for the Galactic sample from Chapter 2. From now on, we will refer to the objects in the LMC, SMC, and Fornax dwarf galaxy as the ‘satellite sample’ or ‘satellite clusters’. We compare the central slope measurements for both samples by plotting the slope histograms side by side (Fig 3.10). We note that in both SB and LD central slopes, the satellite sample extends to steeper slopes than the Galactic sample. In total, 63% of the satellite sample is consistent with having flat cores, the remaining objects display a continuous distribution of central slopes between 0 and  $-1.4$  for surface brightness, and between 0 and  $-2.2$  for luminosity density. From Noyola & Gebhardt (2006), we know that 50% of the Galactic sample is consistent with having flat cores, a smaller fraction than for the satellite sample. For the Galactic sample we do not find any object with central slopes steeper than  $-0.8$  for SB or  $-1.8$  for LD, we find two objects (R136 and Fornax 3) steeper than that in the satellite sample. Even when these differences are taken into account, the main conclusion that the slope distributions are inconsistent with a bimodal distribution of flat and PCC cores is the same for both samples.

We plot a variety of physical quantities against each other in order to explore for possible correlations in both samples. We observe in Figure 3.11

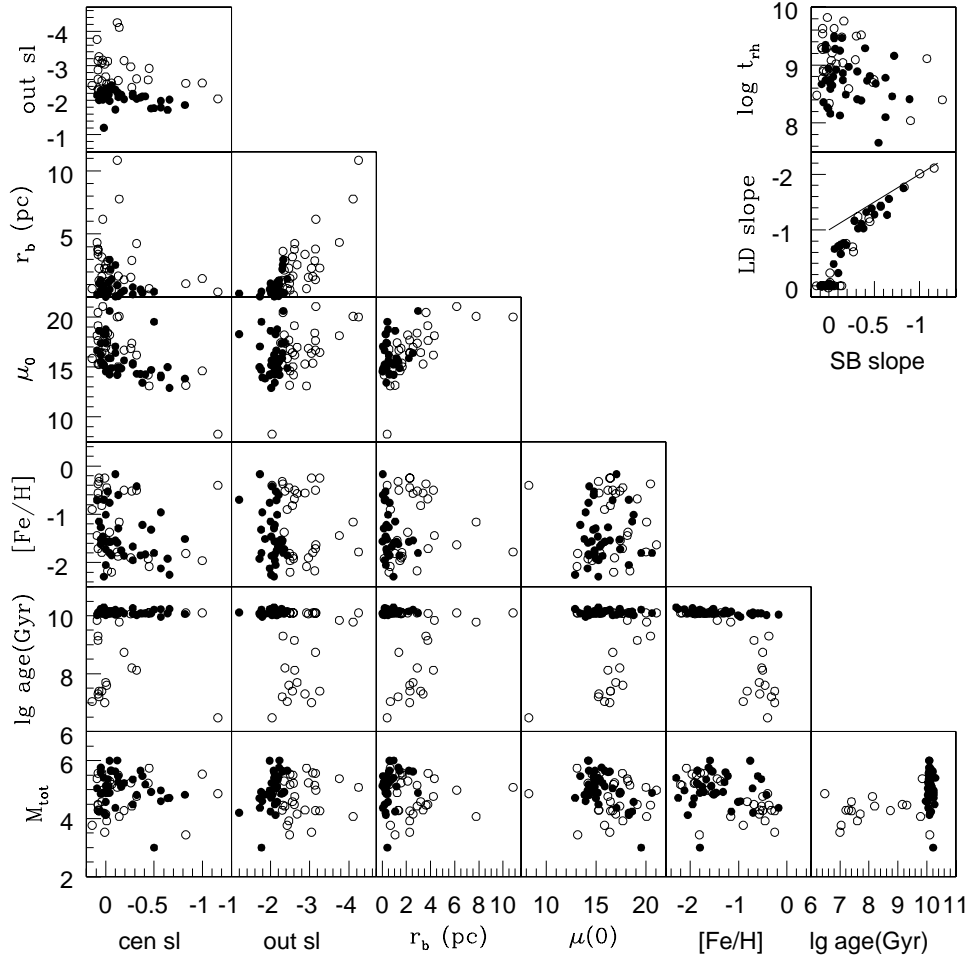


Figure 3.11 Surface brightness central and outer logarithmic slopes, logarithmic break radius (in parsecs), central surface brightness, metallicity, logarithmic age, and total mass plotted against each other for the LMC+SMC+Fornax sample (open points) and the Galactic sample (solid points). We also show on the top right corner two panels with SB slope versus half-light relaxation time and versus LD slope (the solid line represents ‘LD slope = SB slope + 1’). The distances to the clusters are assumed to be 45 kpc for the LMC, 60 kpc for the SMC and 140 kpc for the Fornax dwarf galaxy.

that the younger clusters, which belong to the satellite sample, have a narrower metallicity and total mass ranges ( $-1 < [\text{Fe}/\text{H}] < 0$  and  $3 \times 10^3 M_\odot < M_{tot} < 10^5 M_\odot$  respectively) than the old ones. Both metallicity and total mass do not show any clear correlations with other physical quantities. The outer slope shows weak correlations for the satellite sample in the sense that clusters with steeper outer slopes seem to be older, have fainter central surface brightness, and larger break radius. The Galactic clusters appear to have shallower outer slopes than the satellite ones, but this can be an effect of the different models fitted for the two samples (see section 3.3.4). We note that there seems to be a narrow range of outer slopes between  $-2$  and  $-3$  for the clusters with steep central slopes for both samples. There is a clear correlation of central slopes with the value for central surface brightness in which clusters with steeper central slopes have brighter central surface brightness values. Central surface brightness seems to be fainter for older clusters, but this is only observed for the satellite sample. Regarding the break radius, we should clarify that the lack of clusters with break radii larger than  $\sim 4$  pc in the Galactic sample is a selection effect due to the fact that we required the core radius to fit on the WFPC field of view. Since the satellite galaxies are  $4 - 14$  times further away than the average Galactic cluster, we can include clusters with larger break radius for the satellite sample. We note that all the clusters with a central surface brightness brighter than  $\sim 16$  mag/arcsec<sup>2</sup> have break radii smaller than  $\sim 2$  pc. Our measured break radius follows the same trend observed for core radius versus age by other authors Elson et al. (1989); Elson (1992); de Grijs et al. (2002). Clusters younger than 1 Gyr have break radii smaller than 4 pc, while older clusters span a wide range of break radii. We notice that every cluster with central SB slope steeper than  $-0.5$  has a half-light relaxation time shorter than 1 Gyr. Finally, the SB slope versus LD slope relation for

the satellite clusters lies right on top of the one observed for Galactic clusters, which in turn is similar to the one observed for galaxies (Gebhardt et al., 1996).

### 3.5 Summary

We obtain central surface brightness profiles for 21 clusters in the Large Magellanic Cloud, 5 in the Small Magellanic Cloud, and 4 in the Fornax dwarf galaxy. We construct and analyze a large number of simulated images in order to find the most suitable way to obtain surface brightness, as well as to estimate our uncertainties. The profiles are constructed by measuring integrated light with a robust statistical estimator. We combine *HST*/WFPC2 images in two filters (F555W and F814W) when available and present profiles normalized to V-band magnitudes.

When our results are compared with previous results that use different analysis techniques, we find very good agreement for  $\sim 60\%$  of the sample. For the remaining 40%, our central photometric points are brighter than previous measurements. For some objects, changes are observed in the shape of the central surface brightness profile making them no longer compatible with a flat core parametric fit. We confirm the existence of a steep central cusp for three clusters previously classified as post core-collapse. We also find a subpopulation of objects with shallow cusps with logarithmic central slopes between  $-0.2$  and  $-0.5$ . When we plot a variety of physical quantities searching for correlations, we find indications that the younger clusters tend to have smaller break radius, shallower outer slopes, and brighter central surface brightness. In particular, the youngest cluster in the sample, R136, shows the steepest central profile and the brightest central surface brightness. We also observe a



clear correlation in which the clusters with the steepest central slopes are the ones with the brightest central surface brightness.

Table 3.1. Simulations input.

model	inner slope $\gamma$	outer slope $\beta$	break radius (pixels)	hardness of brake $\alpha$
model 1	0.0	1.8	85	2
model 2	0.0	2.5	340	3
model 3	0.2	2.5	90	1
model 4	0.4	1.6	90	2
model 5	0.7	1.8	90	2
model 6	0.9	2.0	90	1

Table 3.2. LMC, SMC and Fornax Sample.

name	primary dataset	filter	exp. time (sec)	secondary dataset	filter	exp. time (sec)	$\alpha$ center	$\delta$ center
NGC 1466	U2XJ0105B	F555	3520	U2XJ0108B	F814	4520	03:44:32.75	-71:40:16.53
NGC 1651	U2S75801B	F555	1000	U2S75803B	F814	1000	04:37:31.95	-70:35:06.99
NGC 1711	U2Y80501B	F555	1520	...	...	...	04:50:39.95	-69:59:06.60
NGC 1754	U2XQ0103B	F555	1540	U2XQ0109B	F814	1860	04:54:18.35	-70:26:31.60
NGC 1786	U2XJ0205B	F555	3520	U2XJ0208B	F814	4520	04:59:07.58	-67:44:44.96
NGC 1805	U4AX0204B	F555	435	U4AX020AB	F814	960	05:02:21.48	-66:06:41.60
NGC 1818	U4AX3603B	F555	2500	U4AX3703B	F814	2500	05:04:10.58	-66:26:26.63
NGC 1835	U2XQ0203B	F555	1540	U2XQ0209B	F814	1860	05:05:06.97	-69:24:13.28
NGC 1866	U5DP020TB	F555	2512	U5DP020PB	F814	2620	05:13:29.00	-65:27:15.37
NGC 1868	U4AX5803B	F555	2500	U4AX5903B	F814	2500	05:14:34.53	-63:57:14.68
NGC 1898	U2XQ0303B	F555	1540	U2XQ0309B	F814	1860	05:16:41.92	-69:39:23.96
NGC 1916	U2XQ0403B	F555	1549	U2XQ0409B	F814	1860	05:18:37.79	-69:24:27.05
NGC 1984	U5AY0901B	F555	1410	U5AY0904B	F814	1410	05:27:39.97	-69:08:02.14
NGC 2004	U2Y80201B	F555	1520	U2Y80204B	F814	1510	05:30:40.24	-67:17:15.64
NGC 2005	U2XQ0503B	F555	1540	U2XQ0509B	F814	1860	05:30:10.32	-69:45:08.82
NGC 2019	U2XQ0603B	F555	1540	U2XQ0609B	F814	1860	05:31:56.47	-70:09:32.48
NGC 2031	U2Y80301B	F555	1520	U2Y80304B	F814	1510	05:33:40.70	-70:59:07.44
R136	U2HK030JB	F555	1211	U2HK0317B	F814	1205	05:38:42.52	-69:06:02.98
NGC 2100	U5AY0701B	F555	1410	U5AY0704B	F814	1410	05:42:07.66	-69:12:43.47

Table 3.2 (cont'd)

name	primary dataset	filter	exp. time (sec)	secondary dataset	filter	exp. time (sec)	$\alpha$ center	$\delta$ center
NGC 2214	U5AY1101B	F555	1410	U5AY1104B	F814	1410	06:12:56.92	-68:15:37.92
NGC 2257	U2XJ0505B	F555	3520	U2XJ0508B	F814	4520	06:30:00.89	-64:19:23.26
KRON 3	U26M0G02T	F555	300	...	...	...	00:24:46.03	-72:47:35.09
NGC 121	U3770501B	F555	1840	U377050BB	F814	2080	00:26:48.62	-71:32:09.10
NGC 330	U5AY1001B	F555	1410	U5AY1004B	F814	1410	00:56:18.41	-72:27:49.65
NGC 411	U26M0302T	F555	300	...	...	...	01:07:56.35	-71:46:01.59
NGC 416	U26M0502T	F555	200	...	...	...	01:07:59.30	-72:21:17.43
FORNAX 2	U30M020EB	F555	5640	U30M020IB	F814	7720	02:38:44.26	-34:48:27.11
FORNAX 3	U30M030EB	F555	5518	U30M030IB	F814	7720	02:39:48.22	-34:15:26.87
FORNAX 4	U2LB0203B	F555	2400	U2LB0205B	F814	2400	02:40:09.01	-34:32:19.81
FORNAX 5	U30M040EB	F555	5640	U30M040IB	F814	7720	02:42:21.14	-34:06:04.32

Table 3.3. Results

name	$\mu_V(0)$ (mag/arcsec <sup>2</sup> )	$r_b$ arcsec	$r_h$ arcsec	$lgt_{rh}$ years	SB slope logarithmic	error	LD slope logarithmic
NGC 1411	18.4	13.2	24.3	9.21	-0.02	0.18	0
NGC 1651	20.5	16.6	71.2	9.63	0.08	0.20	0
NGC 1711	17.0	11.7	30.7	8.96	0.00	0.18	0.00
NGC 1754	17.4	5.6	15.2	8.81	-0.01	0.12	-0.23
NGC 1786	15.0	7.6	14.9	9.04	-0.13	0.14	-0.70
NGC 1805	16.4	10.4	17.0	8.33	0.01	0.13	0.04
NGC 1818	16.4	10.5	26.9	8.92	0.07	0.14	0
NGC 1835	15.4	7.5	11.4	8.89	-0.04	0.16	0
NGC 1866	16.2	19.4	49.7	9.52	-0.32	0.12	-1.24
NGC 1868	16.7	6.3	16.2	8.59	-0.19	0.13	-0.76
NGC 1898	18.2	9.7	42.0	9.62	-0.04	0.13	0
NGC 1916	13.1	3.0	8.2	8.75	-0.45	0.16	-1.15
NGC 1984	15.8	3.1	18.4	8.48	0.14	0.08	0
NGC 2004	15.3	5.5	21.0	8.77	0.08	0.16	0
NGC 2005	14.2	0.7	10.6	8.80	-0.44	0.13	-1.21
NGC 2019	13.2	4.9	11.3	8.04	-0.83	0.15	-1.77
NGC 2031	17.4	13.3	59.6	9.50	-0.20	0.11	-0.61
R136	8.3	1.9	8.4	8.40	-1.16	0.21	-2.11
NGC 2100	15.2	6.0	25.6	8.89	0.07	0.14	0

Table 3.3 (cont'd)

name	$\mu_V(0)$ (mag/arcsec <sup>2</sup> )	$r_b$ arcsec	$r_h$ arcsec	$lgt_{rh}$ years	SB slope logarithmic	error	LD slope logarithmic
NGC 2214	17.7	10.4	42.6	9.08	-0.01	0.13	-0.06
NGC 2257	21.0	28.3	68.7	9.82	0.03	0.16	0
KRON 3	20.1	27.2	44.4	9.76	-0.14	0.17	0
NGC 121	17.6	13.3	23.2	9.54	0.08	0.14	0
NGC 330	16.4	11.1	29.4	9.29	0.04	0.12	0
NGC 411	19.1	13.2	30.1	0.27	0.08	0.25	0
NGC 416	18.1	15.1	18.1	9.30	0.09	0.24	0
FORNAX 2	20.0	16.0	12.4	9.48	-0.12	0.13	0
FORNAX 3	14.6	2.2	5.2	9.10	-1.00	0.19	-2.01
FORNAX 4	16.8	2.3	6.1	9.09	-0.26	0.13	-0.70
FORNAX 5	16.8	0.8	5.8	9.02	-0.06	0.10	0.00

## Chapter 4

# Possible Intermediate Mass Black Hole in Omega Centauri

*Now there's a look in your eyes  
like black holes in the sky*

DG, RW, RW.

### 4.1 Introduction

The globular cluster  $\omega$  Centauri (NGC 5139) is the largest and most massive member of the Galactic cluster system with a tidal radius of 69 parsecs (Harris, 1996), an estimated mass of  $5.1 \times 10^6 M_{\odot}$ , and a measured central velocity dispersion of  $22 \pm 4 \text{ km s}^{-1}$  (Meylan et al., 1995). The cluster shows global rotation, measured with radial velocities, of  $8 \text{ km s}^{-1}$  at a radius of 11 pc from the center (Merritt et al., 1997) and confirmed with proper motions (van Leeuwen et al., 2000), which makes it one of the most flattened galactic globular clusters (White & Shawl, 1987). A rotating flattened model including proper motion and radial velocity datasets by van de Ven et al. (2006) calculate total mass of  $2.5 \times 10^6 M_{\odot}$ , lower than previous estimates, and confirm the central line-of-sight velocity dispersion value of  $20 \text{ km s}^{-1}$ . They measure a dynamical distance of  $4.8 \pm 0.3 \text{ kpc}$ .  $\omega$  Centauri has a peculiar, highly bound retrograde orbit (Dinescu et al., 2001).

$\omega$  Centauri has a stellar population that makes it stand out from the

rest of the Galactic globular clusters due to its complexity. It shows a broad metallicity distribution (Bedin et al., 2004; Norris et al., 1996), as well as a kinematical and spatial separation between the different subpopulations (Pancino et al., 2003; Norris et al., 1997). All these results have led to the hypothesis that  $\omega$  Centauri is not a classical globular cluster but instead is the nucleus of an accreted galaxy (Freeman, 1993; Bekki & Freeman, 2003; Meza et al., 2005). The hypothesis of being the product a merger of two globular clusters (Icke & Alcaïno, 1988) and of self-enrichment (Ikuta & Arimoto, 2000) have also been proposed to explain the stellar populations.

The high measured velocity dispersion together with the possibility of being a stripped galaxy make  $\omega$  Centauri an interesting candidate for harboring a black hole in its center. The extrapolation of the  $M_{\bullet} - \sigma$  relation for galaxies (Gebhardt et al., 2000a; Ferrarese & Merritt, 2000; Tremaine et al., 2002) predicts a  $1.3 \times 10^4 M_{\odot}$  black hole for this cluster. The sphere of influence of such a black hole for a star cluster at the distance of  $\omega$  Centauri with a velocity dispersion of  $20 \text{ km s}^{-1}$  is  $\sim 5''$ , making it an excellent target for ground-based observations.

Two globular clusters have been suggested as harboring intermediate mass black holes in their nuclei. One is the galactic cluster M15 (Gebhardt et al., 2000a; Gerssen et al., 2002, 2003) and the other is G1, a giant globular cluster around M31 (Gebhardt et al., 2002, 2005). M15 is considered to be the proto-typical post-core-collapse cluster, but its dynamical state has been debated between harboring a black hole or containing a large number of compact remnants in its center (Baumgardt et al., 2003b,a). Unfortunately, observational constraints between these two hypothesis remain inconclusive (van den Bosch et al., 2006). G1 on the other hand, has a core with characteristics closer



to those of  $\omega$  Centauri, and observations support the black hole interpretation for G1. The G1 black hole models are preferred since the M/L profile is expected to be flat in its core, so any rise in the velocity dispersion is unlikely to be due to remnants that concentrated there from mass segregation. The situation is similar in  $\omega$  Centauri. In this paper we report photometric and kinematical measurements that suggest the presence of a central black hole in  $\omega$  Centauri.

## 4.2 Surface Brightness Profile

The surface density profile at large radii for  $\omega$  Centauri has been measured from a combination of star counts and aperture photometry from ground based images (Meylan, 1987; Trager et al., 1995; van Leeuwen et al., 2000). We measure the central part of the profile taking advantage of *Hubble Space Telescope* (*HST*) spatial resolution. We measure integrated light from an ACS F435W image (340 sec) applying the technique described in detail in Noyola & Gebhardt (2006), which uses a robust statistical estimator, the bi-weight, to calculate number of counts per pixel on a given annulus around the center of the cluster. As a test, we also measure the profile from a narrow-band H-alpha image from the Rutgers Fabry-Perot (Xie et al., 2006) with lower spatial resolution. Since both images have a limited radial coverage, we use the Chebychev fit of Trager et al. (1995) for the surface brightness profile to cover the full, radial extent of the cluster. All profiles are normalized to the Trager profile, which brings them to  $V$ -band mag/arcsec<sup>2</sup>.

Having accurate coordinates for the center of the cluster is crucial when measuring density profiles. Using the wrong center typically produces a shallower inner profile. We use a technique where we take an initial guess center,

divide the cluster in eight concentric sectors around this center, and calculate the standard deviation of the sum of stars for the eight sectors. The radius of the sectors is chosen to be as large as the image will allow, in this case it is  $\sim 2'$ . We repeat the procedure for a grid of center coordinates and use the one that has the minimum standard deviation. Details about the technique can be found in Noyola & Gebhardt (2006). The coordinates for our center are RA 13 : 26 : 46.043 and DEC  $-47 : 28 : 44.8$  on the ACS dataset J6LP05WEQ using its WCS zero point.

The measured profiles from the B-band and H-alpha images are consistent as can be seen on Figure 4.1. The H-alpha profile follows the turnover around the core radius very well up to  $100''$  and it also shows the rise toward the center, but it is noisier than the ACS profile. The solid line is a smooth fit made to the combination of the photometric points from ACS inside  $40''$  and Trager et al. Chebychev fit outside  $40''$ . For comparison, we include the Trager et al. (1995) photometric points in the plot. The surface brightness profile shows a continuous rise toward the center with a logarithmic slope of  $-0.08 \pm 0.03$ , which is in contrast to the common notion that  $\omega$  Centauri has a flat core. Van Leeuwen et al (2000) perform star counts for giant stars and notice that they are more concentrated than previously thought. Our result is consistent with their finding. Baumgardt et al. (2005) performed N-body models of star clusters with an initial King profiles and containing a central black hole. They predict the formation of a shallow cusp of  $-0.1$  to  $-0.3$  logarithmic slope after  $1.5 - 4$  relaxation times. Our observed surface brightness profile is intriguing considering these models, but of course, only kinematical measurements can determine the mass profile, including the existence of a central black hole.

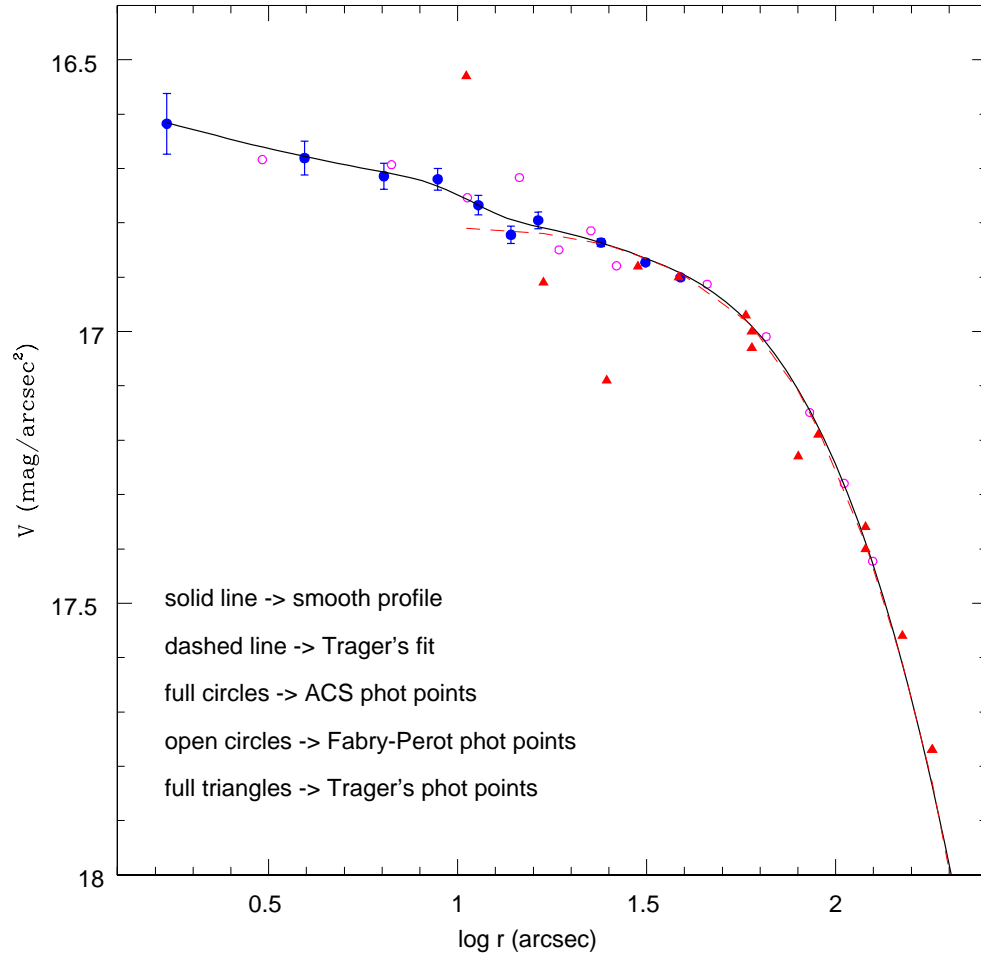


Figure 4.1 Surface brightness profiles for  $\omega$  Centauri. The circles show our measured photometric points from the ACS (filled) and H-alpha (open) images. The triangles show photometric points obtained from ground based images by Trager et al. The dashed line is Trager's Chebychev fit. The solid line is our smooth fit to the combination of the ACS points inside  $40''$  and Trager's Chebychev fit outside.

### 4.3 Kinematic Measurements

Obtaining kinematic information of the central regions of Galactic globular clusters is a challenging task since the brightest stars dominate with typical ground-based conditions and the extreme crowding produces confusion. Measuring individual radial velocities requires a spatial resolution that can only be achieved with adaptive optics or from space. On the other hand, measuring velocity dispersion from an integrated spectrum is subject to shot noise due to giant stars whose contribution dominates the light. Dubath et al. (1997) calculate the relative contribution to integrated light by different stellar groups. They find that the contribution from the few brightest stars is equal in weight to that of the much larger numbers of fainter stars. Therefore, the only way to obtain accurate radial velocity dispersion measurements from an integrated spectrum is if the participation of the brightest stars can somehow be avoided or at least minimized. One way to do this is by observing crowded regions with an integral field unit (IFU) which produces individual spectra of subsections in the region (typically  $\sim 0''.2$  in size). One can exclude the spectra affected by the brightest stars when measuring the integrated background light and thus decrease the shot-noise contribution to the uncertainty. The Gemini telescopes operate primarily using a queue scheduling, which makes them an excellent tool to measure integral field spectra of globular clusters since observing constraints (such as excellent seeing) can be specified in advance, and data are only taken when the required observing constraints are met.

As part of the Science Verification program for the Gemini GMOS-South IFU, we obtained nod-and-shuffle observations on February 29 2004 (program ID: GS-2003B-SV-208). We use the IFU in 2-slit nod-and-shuffle mode, which gives a field of view of  $5 \times 5$  arcsec, comprised of 700 individual

lenslets plus fiber elements, each of which covers approximately 0.2 arcsec on the sky. We use the R600 grating, yielding a resolving power  $R=5560$ , which we measure from the arclamp spectral lines, along with the Calcium Triplet filter to give a wavelength coverage of 7900-9300Å. Three fields are observed, each for a total integration time of 900 sec on source and 900 sec on sky. The observations are made using the nod-and-shuffle technique with 30 sec sub-integrations observed in a B-A-A-B pattern, where A is the on-source position and B is the sky position, located 498" away. The nod-and-shuffle technique improves the sky subtraction, especially in the presence of CCD fringing, by sampling the object and sky on exactly the same CCD pixels, with exactly the same light path, on timescales comparable to those of the sky emission line variability. The first of the three fields is located at the cluster center, and the second field is centered 14" away. The third field appears to have been pointing somewhere else but, despite much effort, we cannot determine exactly where the IFU observations are pointed (they do not match anything in the acquisition image for this field). The reconstructed IFU image for this third field contains fewer stars and the PSF is obviously broader than for the other two. It is clear that the exposure was taken during much worse seeing conditions than the other two fields, so shot-noise effects are likely to be important; for this reasons we exclude the third field from further analysis. Using the standard tasks from the IRAF-GEMINI package we sky subtract, flat-field, and extract the spectra for each fiber and apply a wavelength calibration.

The standard flat subtraction does not remove all of the fringing pattern in the image. As a result, a constant number of counts have to be subtracted from the data frames before flattening in order to reduce fringing problems.

Relative to the bias frame, the amount of additional counts from scattered light is about 8%. Even after this procedure, there is some residual fringing that can only be alleviated by combining individual fibers over the full field into one spectrum. To combine individual fibers we first divide by the continuum. The intention is to de-weight the bright stars with respect to the fainter ones, which helps to lessen the problems due to shot noise. For the continuum fit, we run a boxcar of dimension  $111 \times 1$  over the reduced image, and then divide the central pixel by the median of the pixels in the box. This procedure brings all spectra to the same continuum level. We then combine every individual fiber with the six adjacent ones, since this represents one seeing disk for the observations.

Figure 4.2 shows the reconstructed image from the IFU fibers for the central frame and the acquisition image as well as the same region on the ACS image. We also show a convolved image (with the reported seeing for the observations) of the ACS frame. The same match is performed for the field  $14''$  away (Fig 4.3). Both ACS fields contain  $\sim 100$  resolved stars. We construct a luminosity function for the detected stars for each field and compare it to the luminosity function of the entire cluster core. The luminosity function is consistent between the two fields. The brightest stars detected in both fields are two magnitudes fainter than the brightest stars detected in the core of the cluster. This excludes the possibility of the integrated spectra being artificially broadened by the presence of more blue straggler stars in the central field compared to the field  $14''$  away. Using the photometric measurements of individual stars together with the reported seeing, we calculate how many stars contribute to each fiber. Excluding the fibers which are dominated by a single star we estimate that the integrated spectrum of the background unresolved

light represent about 60 stars in both fields.

We focus on the Ca triplet region (8450Å-8700Å) for our analysis. We measure the relative velocities between each fiber for the two fields and obtain velocity distributions from the individual fiber velocities. We fit a Gaussian to the velocity distributions and observe that the one for the central field is clearly broader than for the one 14'' away. The largest relative velocity between two fibers is  $80 \text{ km s}^{-1}$  for the central frame, and  $60 \text{ km s}^{-1}$  for the other one. Using the dispersion of the individual fiber velocities as a measure of the cluster velocity dispersion will be biased. Since multiple stars, in general, provide light to an single fiber, the measured velocity in that fiber will be pulled toward the cluster mean as opposed to representing one star. Thus, the dispersions of the fiber velocities will be biased significantly low. This is what we find although the central frame does have a obviously larger spread in fiber velocities.

To properly estimate the velocity dispersion we have to rely on the integrated light, and require template stars in this case. Unfortunately, we do not have isolated stars that are free from the fringe problems mentioned earlier, so we cannot accurately use template stars observed with the same instrument. We rely on the template stars observed by Walcher et al. (2005), from VLT-UVES observations at around  $R=35000$ . We convolve the spectra to our measured resolving power. To extract the velocity dispersion from the integrated light we utilize the non-parametric, pixel-based technique as described in (Gebhardt et al., 2000b; Pinkney et al., 2003). We choose an initial velocity profile in bins, convolve it with the template (or set of templates), and calculate residuals to the integrated spectrum. The parameters for the line of sight velocity distribution (either velocity bin values or, if desired, a parametric

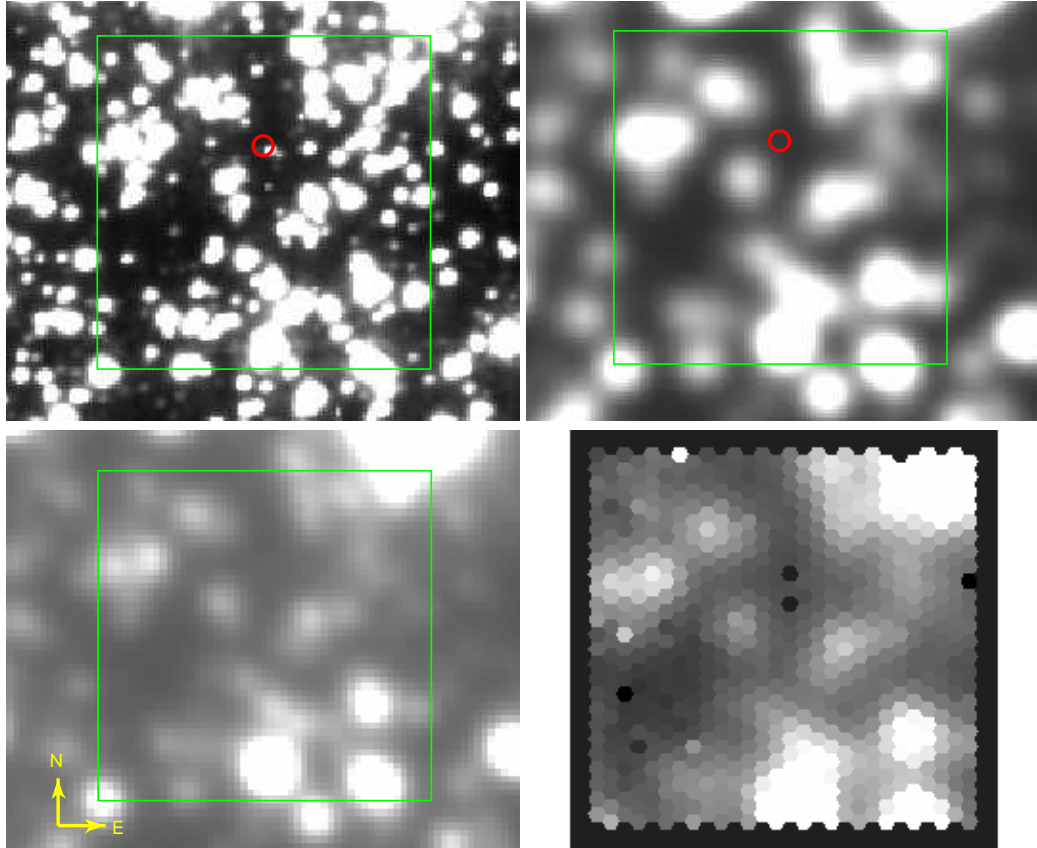


Figure 4.2 The central field observed with the GMOS-IFU. The green box represents the GMOS field of view. Top left: ACS image of the observed region. The red circle marks the center of the cluster. Top right: Convolved ACS image to reproduce the reported seeing during observations. Bottom left: GMOS acquisition image. Bottom right: Reconstructed GMOS-IFU image.



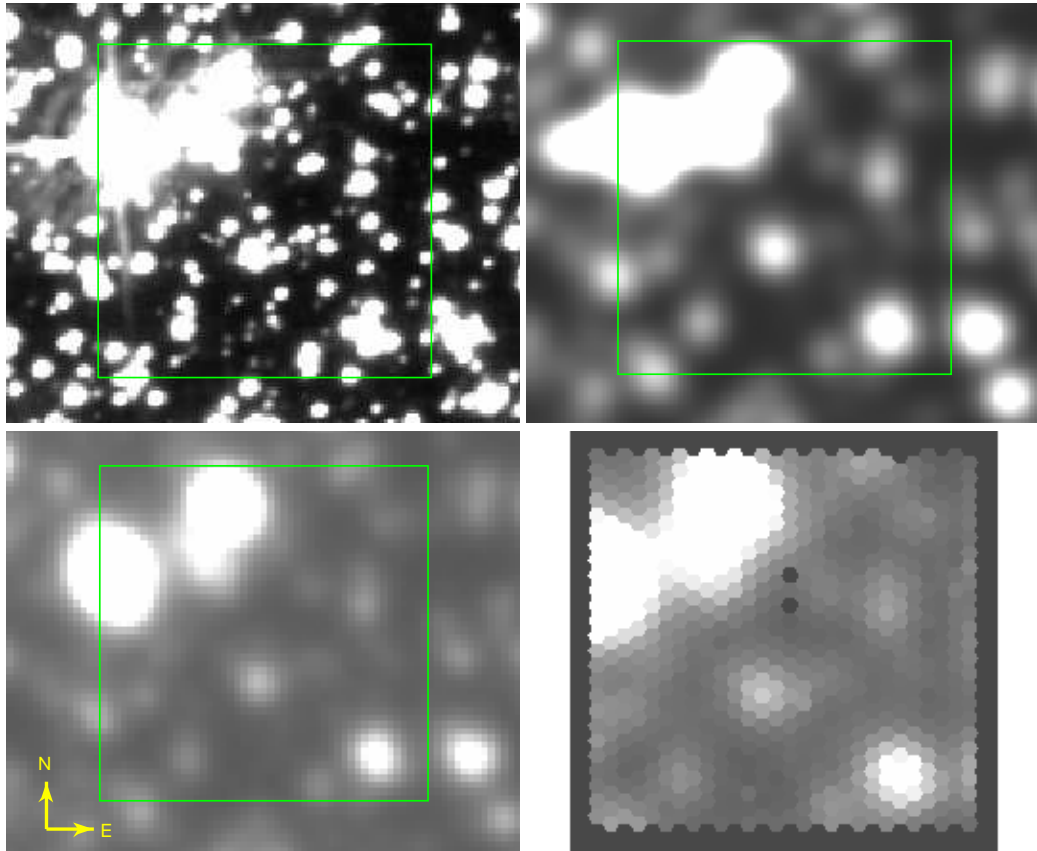


Figure 4.3 Same as fig 2 for the field 14'' away.

Gauss-Hermite expansion) are varied to provide the best match. Monte Carlo simulations determine the uncertainties, and use the measured noise in the spectrum.

The dispersion fitting routine allows for a mismatch in the equivalent width between the object and template. In this case, there is a 30% difference in the equivalent width of the calcium triplet lines. We do not know whether this is caused by the scattered light (unlikely given the amplitude), the specific templates we used,  $\omega$  Centauri's particular composition, or a combination of all three. We have run a variety of tests to determine whether stars of different equivalent widths would cause a bias in dispersions, and find no such bias. We have also measured the dispersions using template stars from the same IFU data, since there is at least one star that is fairly isolated. The uncertainties are larger due to the scattered light problems, but the value of the dispersion remains the same. Thus, we conclude that template issues are not a significant source of bias in the dispersion estimate.

We combine the spectra from individual fibers using a biweight estimator. Different sets of fibers for each frame are combined in order to test for consistency in our results. First, we combine every fiber on the frame, then we exclude the 25%, 50% and 75% brightest fibers. We measure the velocity dispersion for these four spectra for each frame. The measured velocity for the central frame is always higher than the one for the frame 14'' away for every equivalent pair of combined spectra. We measure velocity dispersions from 21.8 to 25.2 km s<sup>-1</sup> for the central field, and 18.2 to 19.1 km s<sup>-1</sup> for the field 14'' away. We adopt  $23.0 \pm 2.0$  km s<sup>-1</sup> for the central field and  $18.6 \pm 1.6$  km s<sup>-1</sup> for the other. The latter measurement coincides with the central velocity dispersion value measured for  $\omega$  Centauri by various authors. Van den

Ven et al. (2006) measure a line of sight velocity dispersion profile by combining various datasets (Suntzeff & Kraft, 1996; Mayor et al., 1997; Reijns et al., 2006; Xie et al., 2006). They use 2163 individual radial velocity measurements divided into polar apertures to obtain the final velocity dispersion profile. We use dispersion estimates as presented in their table 4. The average radius for the spectra that contribute to the central values is  $2''.5$  and  $14''$  for the second. Figure 4.4 presents the velocity dispersion data.

#### 4.4 Models

As discussed in Section 4.2, the central shape of the surface brightness profile of  $\omega$  Centauri resembles that found by Baumgardt et al. (2005) in star clusters harboring black holes. The presence of an IMBH at the center of this cluster is one of the possibilities for explaining the observed rise in velocity dispersion. In order to explore the effect of a central black hole inside  $\omega$  Centauri, we create a series of isotropic models using the non-parametric method described in Gebhardt & Fischer (1995). As a first step we apply a reddening correction to the observed surface brightness profile. Harris (1996) reports  $E_{B-V} = 0.1$  for this cluster. Applying an extinction correction is important for the proper  $M/L$  determination of the models. The extinction correction will only affect the  $M/L$  value of the models, but not the shape of the profiles. We deproject the surface brightness profile using Abel integrals assuming spheroidal symmetry. The integral involves a derivative of the profile, therefore, any amount of noise present is amplified. We apply a spline smoother to the surface brightness profile before deprojecting and thus obtain a luminosity density profile as discussed in Gebhardt et al. (1996); Noyola & Gebhardt (2006). By assuming a mass luminosity ratio, we calculate a mass

density profile, from which the potential and the velocity dispersion can be derived. We repeat the calculation adding a variety of central point masses ranging from 0 to  $7.5 \times 10^4 M_\odot$  while keeping the global  $M/L$  value fixed. Van de Ven et al (2006) measure a fairly constant stellar  $M/L$  profile for  $\omega$  Cen of  $2.5 \pm 0.1$  in the  $V$ -band. We find a constant mass luminosity ratio of 2.7, since this provides the best match to the observed velocity dispersion profile outside the core. The small discrepancy between the  $M/L$  values can be explained by the use of isotropic models versus anisotropic ones.

Figure 4.4 shows the comparison between the different models and the measured dispersion profile. The most relevant part of the comparison is the rise inside the core radius, in particular the rise between the two innermost measurements. As it can be seen, an isotropic model with no black hole present predicts a slight decline in velocity dispersion toward the center, instead we observe a clear rise. The predicted central velocity for the no black hole model is  $14.6 \text{ km s}^{-1}$  which is well below any line of sight velocity dispersion measured inside  $1'$ . The calculated  $\chi^2$  values for each model are plotted in Figure 4.5, as well as a line showing a  $\Delta\chi^2 = 1$ . The  $\chi^2$  curve implies a best-fit black hole mass of  $4_{-1}^{+0.75} \times 10^4 M_\odot$ . Even the original velocity dispersion profile without our two innermost measurement already points to an intriguing discrepancy, but the central measurements confirm an important rise in  $M/L$  from the core radius to the center of this cluster. The central  $M/L$  value is 6.7, which is a considerable rise from the value of 2.5 around the core. Our best fit model implies a central density of  $5.6 \times 10^7 M_\odot/pc^3$  the largest measured in a globular cluster.

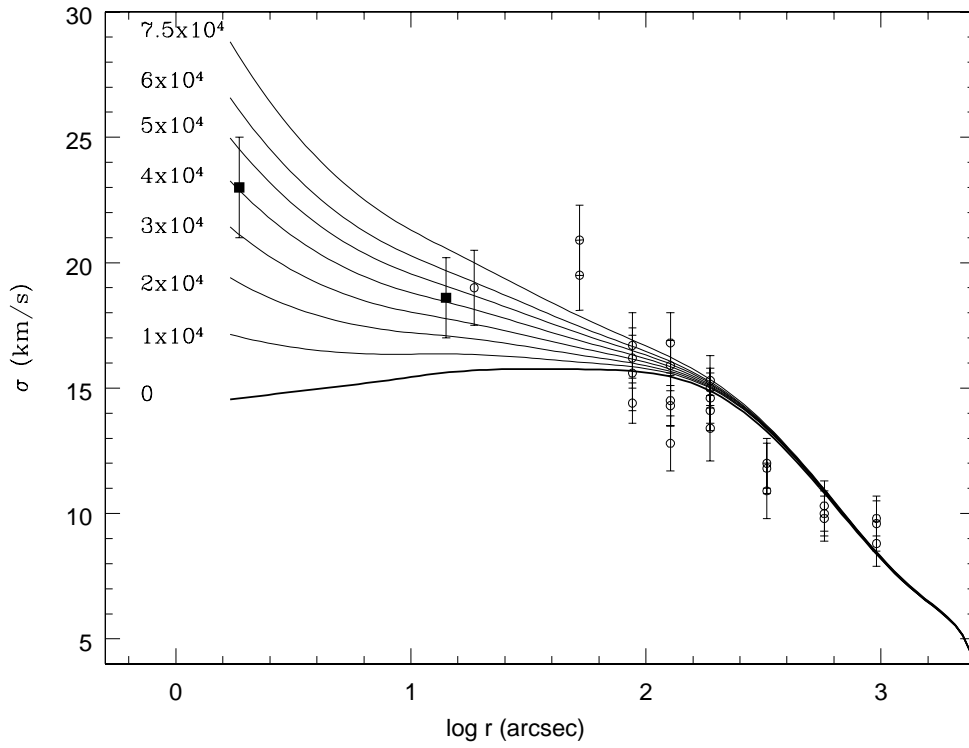


Figure 4.4 Velocity dispersion profile for  $\omega$  Cen with various central black hole models. Filled squares are the dispersions and uncertainties from the GMOS-IFU and open circles are from individual radial velocity measurements. A set of isotropic spherical models of varying black hole masses is shown for comparison. The thick line is the no black hole model and the thin lines represent models with black holes as labeled

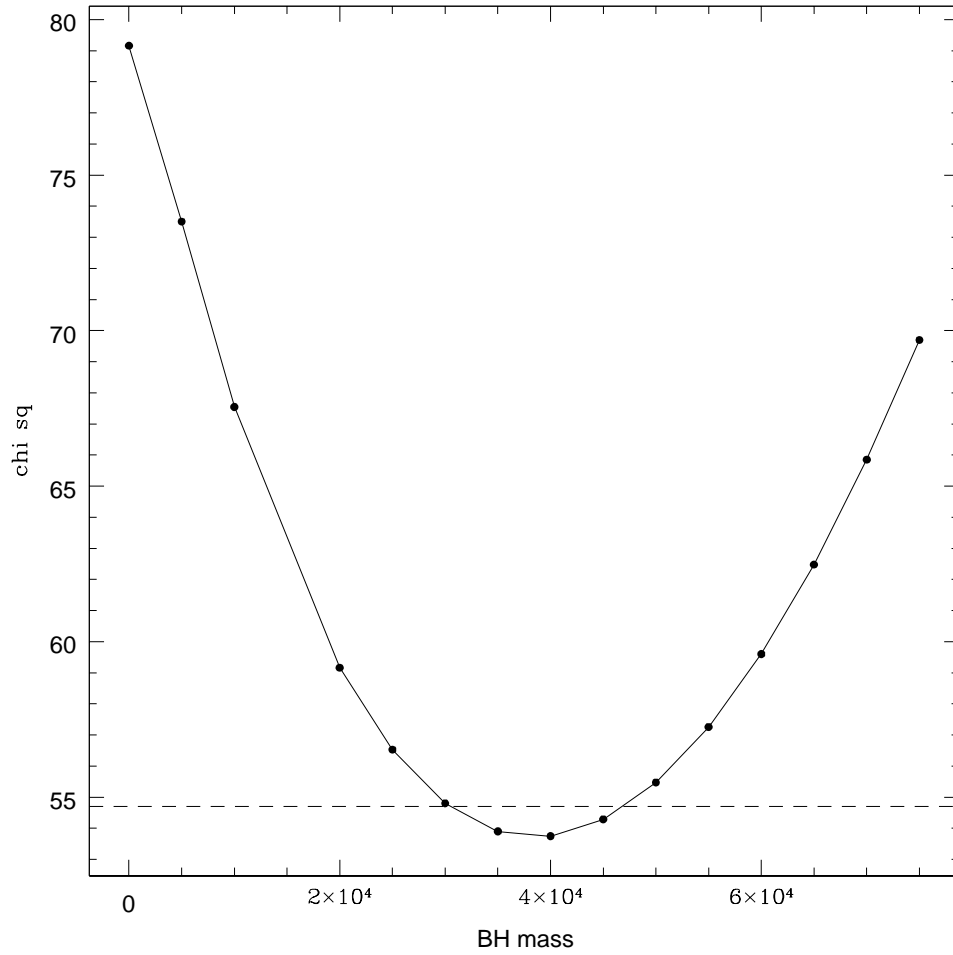


Figure 4.5  $\chi^2$  vs. black hole mass. The minimum is found for a black hole mass of  $4.0 \times 10^4 M_{\odot}$ , with 68% confidence limit at  $3$  and  $4.75 \times 10^4 M_{\odot}$  marked by the dashed line. For our model assumptions, the no black hole model is excluded at greater than the 99% confidence.

## 4.5 Discussion

We measure the surface brightness profile for the globular cluster  $\omega$  Centauri (NGC 5139) from an ACS image in the central  $40''$ . The profile shows a continuous rise toward the center with a logarithmic slope of  $-0.08 \pm 0.03$ , in contrast with previous measurements which found a flat core. The shape of the profile is similar to that obtained from numerical models of star clusters containing black holes in their centers. We measure a line of sight velocity dispersion for two  $5 \times 5''$  regions, one at the center of the cluster and the other  $14''$  away. We detect a rise in velocity dispersion from  $18.6 \text{ km s}^{-1}$  for the outer field to  $23 \text{ km s}^{-1}$  for the central one. We combine these two measurements with previously measured velocity dispersion at larger radii. When comparing the complete profile with a series of isotropic models we conclude that a black hole of  $4.0^{+0.75}_{-1.0} \times 10^4 M_{\odot}$  is necessary to match the observations.

$\omega$  Cen has a weak cusp in the central luminosity density profile, implying that the gravitational potential is very shallow inside the core and therefore mass segregation cannot be an important effect. Ferraro et al. (2006) confirm the lack of segregation by measuring the radial distribution of blue straggler stars, which are heavy stars and should sink to the center of the cluster if there is mass segregation. They find a flat radial distribution of blue stragglers with respect to lighter stellar populations. With this evidence in hand, there is no reason to expect a large variation of  $M/L$  inside the core due to stellar content, so a detected rise in  $M/L$  is likely to come from the presence of a concentrated massive object.

The central density as measured from the  $23 \text{ km s}^{-1}$  dispersion estimate at  $1.8''$ , using the dynamical distance of  $4.8 \text{ kpc}$ , is  $5.6 \times 10^7 M_{\odot}/pc^3$ . This is the largest measured for a globular cluster and it would be difficult to

maintain using stellar remnants. Obviously, if the density is due to solar mass remnants, over  $10^4$  remnants would be required inside of 0.05 parsecs. Using the arguments of Maoz (1998) and Miller (2006), this mass and density makes  $\omega$  Cen one of the better examples where stellar remnants can be ruled out due to evaporation. Maoz estimates that for these numbers, any cluster of remnants will have evaporated within  $10^{10}$  years.

Figure 4.6 shows the known  $M_{\bullet} - \sigma_v$  relation for black holes in elliptical galaxies and bulges. The galaxies used to determine the relation (Tremaine et al., 2002) are plotted along with objects containing smaller black holes in low luminosity quasars (Barth et al., 2005), two nearby low luminosity AGN (NGC 4395 and Pox 52), and three globular clusters (G1, M15 and  $\omega$  Cen). The black hole in  $\omega$  Cen lies above the relation, but it is consistent with the scatter observed a larger masses. The measured black hole mass is 1.6% of the total mass of the cluster, which is more than an order of magnitude larger than the canonical value of 0.1% for larger spheroids. If  $\omega$  Cen is indeed the nucleus of an accreted galaxy it is expected that it's original mass was considerably larger than what we measure now. Bekki & Freeman (2003) reproduce the current mass and orbital characteristics of  $\omega$  Cen with a model of an accreted  $10^7 M_{\odot}$  dwarf galaxy. A mass of  $4 \times 10^7 M_{\odot}$  for the original spheroid would put the black hole right on the 0.1% value.

The two pieces of observational evidence that  $\omega$  Cen has a central black hole come from the photometry and the kinematics. From the HST image of  $\omega$  Cen, we measure a central logarithmic surface brightness slope of  $-0.08 \pm 0.03$ . This value is very similar to that claimed by the N-body simulations of Baumgardt et al. (2005) that are most likely explained by a central black hole. Standard core-collapse does not lead to such a large core with a shallow



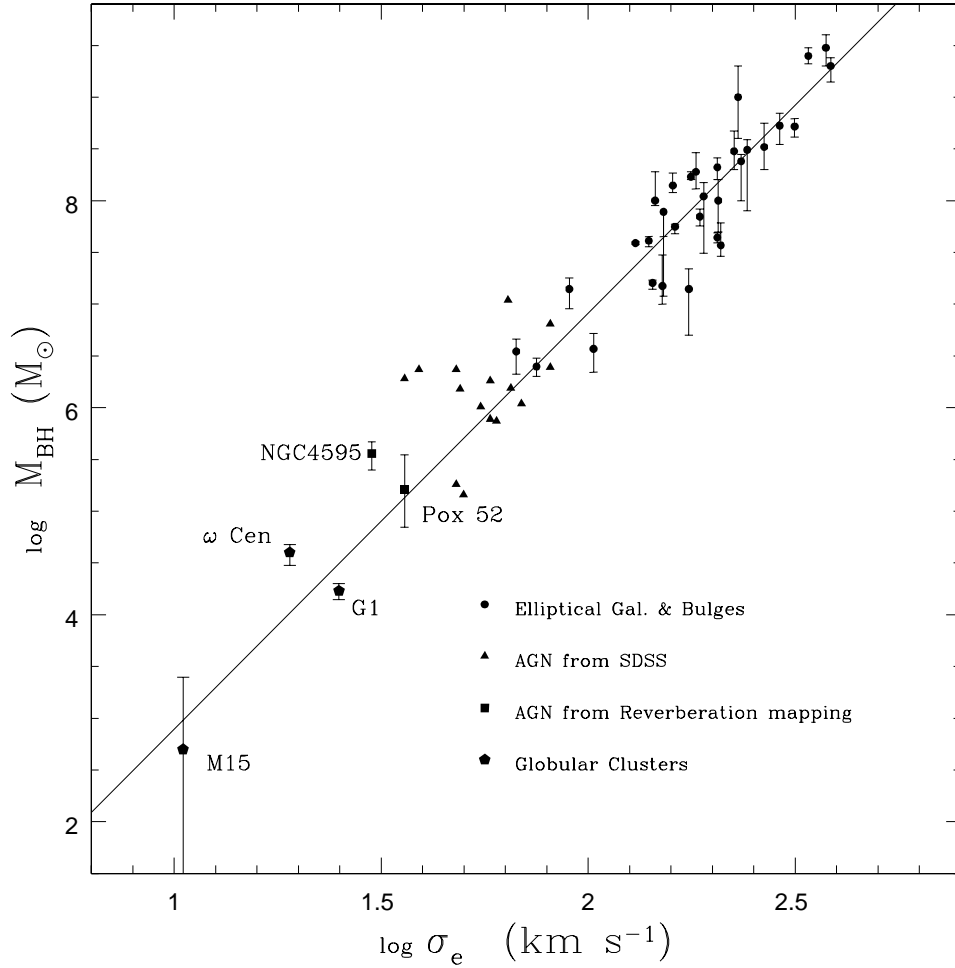


Figure 4.6  $M_{\bullet} - \sigma_{vel}$  relation for elliptical galaxies and bulges. The solid line is the relation in Tremaine et al. (2002).  $\omega$  Cen lies on the low mass extrapolation and suggests a similarity between it and the galaxies. Different types of systems such as star clusters and low luminosity AGN appear to populate the low mass end of the diagram.

central slope. Clusters with central slopes much steeper than this are thought to be undergoing core-collapse. The black hole tends to prevent core collapse while leaving an imprint of a shallow cusp. It will be important to run models tailored to  $\omega$  Cen to see if one can cause and maintain a shallow cusp without invoking a central black hole. However, the main observational evidence for the central mass comes from the increase in the central velocity dispersion, where we detect a rise from 18.6 to 23 km s<sup>-1</sup> from radii of 14 to 2.5". In fact, even excluding the Gemini data presented here, the previous ground-based data suggest a central mass concentration as well. The core of  $\omega$  Cen is around 155 " (about 2.5 '), so the dispersion rise is seen well within the core.

## 4.6 Summary

We measure the surface brightness profile for the globular cluster  $\omega$  Centauri (NGC 5139) from an ACS image in the central 40". The profile shows a continuous rise toward the center with a logarithmic slope of  $-0.08 \pm 0.03$ , in contrast with previous measurements which found a flat core. The shape of the profile is similar to that obtained from numerical models of star clusters containing black holes in their centers. We measure a line of sight velocity dispersion for two 5x5" regions, one at the center of the cluster and the other 14" away. We detect a rise in velocity dispersion from 18.6 km s<sup>-1</sup> for the outer field to 23 km s<sup>-1</sup> for the central one. We combine these two measurements with previously measured velocity dispersion at larger radii. When comparing the complete profile with a series of isotropic models we conclude that a black hole of  $4.0_{-1.0}^{+0.75} \times 10^4 M_{\odot}$  is necessary to match the observations.

## Chapter 5

### Discussion and Conclusions

With the goal of properly discussing the results presented in this dissertation, we summarize results for theoretical models and observations in order to make comparisons with analysis by other authors. At this point, both N-body and Monte Carlo simulations are starting to include a realistic number of particles when simulating star clusters, but the N-body models are still unable to include large numbers of binary systems, which are known to have important effects on the dynamical evolution of a cluster. Fokker-Planck (FP) simulations are still the main source for comparison with observations, particularly when dealing with core collapse. A few globular clusters have been studied using orbit-based Schwarzschild analysis, we discuss these cases as well. Since core-collapse and the presence of a central black hole are the two mechanisms that can dramatically alter the surface brightness profile and kinematics of a cluster, we discuss them in detail below.

#### 5.1 Core-collapse

In the past, globular clusters for which the central surface brightness profile departs from a King profile have been classified as being in a post-core-collapse state. Since close to 50% of the objects studied here show central SB profiles that depart from King profiles, it is very important to analyze in detail all the available information about core-collapse in order to make a

meaningful comparison. Fokker-Planck analysis can include a large number of stars as well as anisotropy by utilizing a statistical treatment. Issues like the inclusion of binaries or global rotation have proved to have an impact on the modeled evolution during and after core-collapse. For this reason, most of the theoretical knowledge that we have about core-collapse comes from Fokker-Planck analysis.

The first tool for comparison are the central logarithmic slopes of the measured luminosity density profiles. As mentioned in section 1.2 the observed surface brightness slope depends on the mass of the observed stars and on the mass of the heaviest stellar group that dominates the core. Previous studies have compared the observed surface brightness profile to detailed models in this context. In particular, detailed Fokker-Planck models have been constructed for m15 (Dull et al., 1997), NGC 6397 (Drukier, 1995), and M71 (Drukier et al., 1992). The first two cases are clusters considered to be in a post-core-collapse state because they show steep cusps in the central profiles. For both cases, it is concluded that the individual mass of the heavy dark stellar remnants in the core has to be around  $1.3M_{\odot}$  due to the central slope observed for the visible stars. For M71, a cluster showing a flat core with  $r_c = 38''$ , mass segregation measurements are compared with models. Measurements indicate a high degree of mass segregation and a very short relaxation time for this cluster, which suggests that it should have undergone core-collapse. The flat central slope can be consistent with the cluster undergoing gravothermal oscillations only if very heavy stellar remnants dominate the core. The analysis concludes that models with a large number of heavy remnants in the core are inconsistent with the observed degree of mass segregation and they predict an unacceptably high value for the central velocity dispersion. Although this de-

tailed models have only been carried out for a few clusters, it is worth pointing out that, for all of them, it has been ruled out that stars more massive than  $\sim 1.4 M_{\odot}$  dominate the core mass. In order to reproduce the shallow slopes observed in our sample by invoking a post-core-collapse state, the necessary mass of the dominant heavy stars is around  $12 M_{\odot}$ . This would require a top heavy initial mass function, a high retention factor of exploding stars, and it would also require a good explanation as to why other clusters would be so different from the three cases mentioned above.

The most detailed modeling of core collapse for an individual object has been carried out for the globular cluster M15. Dull et al. (1997) create FP models that they fit to the observed surface brightness, velocity dispersion profiles, and millisecond pulsar accelerations. They indicate that the observed population of blue stragglers appears to be too small for a cluster that just underwent core collapse. By comparing the observed surface brightness profile with various models, they conclude that M15 must be on a post-collapse bounce state intermediate between deep core-collapse and complete re-expansion of the core. Since M15 has one of the steepest profiles in our observed sample, it appears that even invoking this intermediate phase, it is unlikely to reproduce the full range of slopes that we observe.

The next tool for comparison is the observed ratio of the core radius to half-light radius. It has been known for some time that, as discussed in 1.2, core-collapse evolution will inevitably lead to gravothermal oscillations for clusters with more than 8000 member stars (Murphy & Cohn, 1988; Gao et al., 1991). This is due to binary heating in the core of the cluster and occurs both in the case when binaries are primordial or when they form by three body encounters during core collapse, although the timescales for core-collapse will

be very different for each case. The occurrence of the first core-collapse is delayed if primordial binaries are present in the cluster. All these studies find that, after the first collapse and during the successive bounces, the core only spends a small amount of time in a highly collapsed state. Most of the time the core is in an expanded post-collapse state. The average core radius during the oscillations is  $0.01 - 0.02r_h$  (Breedem et al., 1994). Makino (1996) perform N-body calculations with a maximum of 32,000 particles and compare with results obtained by FP models. They confirm that gravothermal oscillations do take place in clusters without primordial binaries, but they measure smaller core sizes during post-collapse bounce and notice that the core size is smaller for a larger number of stars in the simulation.

## 5.2 Black Holes

As discussed in section 1.3, the presence of an intermediate mass black hole at the center of a star cluster makes the density profile of a cluster depart from a flat core and develop a cusp. We observe central cusps with various slopes for an important fraction of the profiles in our samples. We need to explore the nature of these cusps in detail, both for surface brightness and luminosity density.

Every analytical study or simulation placing a black hole in the middle of a star cluster finds that a power-law density distribution is formed around the black hole (Bahcall & Wolf, 1977; Shapiro, 1977; Lin & Tremaine, 1980; Yuan & Zhong, 1990). The exponent of the power-law is always around  $-1.7$  for analytical calculations. Baumgardt et al. (2005) perform detailed numerical simulations of King-type clusters with a sizable initial core containing an intermediate-mass black hole in their center. Their results show that the three-

dimensional cusp has a power-law slope of  $-1.55$ , but the surface brightness profiles show shallow cusps with slopes around  $-0.25$ , clearly distinguishable from zero. There are a number of clusters in our samples whose central slopes are close to that value. Baumgardt et al. (2005) calculate which objects in our Galactic sample are compatible with their simulations. They base their comparison on the central slopes, relaxation times, concentration, and core radius to half light radius ratio. They find five clusters (NGC 5286, NGC 5694, M80, M62, and NGC 6388) that are compatible with their simulations, and therefore are possible hosts of an intermediate mass black holes.

There are evidences from X-ray observations for the existence of intermediate mass black holes inside star clusters. Ultra luminous X-ray sources (ULX) have been suggested to be produced from gas accretion by an IMBH. In particular, the X-1 source in the starburst galaxy M82 is considered to be the best candidate to host an IMBH due to its X-ray luminosity (Matsumoto & Tsuru, 1999; Matsumoto et al., 2001) and the high frequency radio variability (Strohmayer & Mushotzky, 2003). The position of the X-ray source has been shown to coincide with a young dense stellar cluster known as MGG-11 (McCradly et al., 2003). Portegies Zwart et al. (2004) perform N-body simulations which show possible formation scenarios for an intermediate mass black hole in MGG-11. They stress that the density distribution of the cluster is a crucial ingredient to achieve runaway formation of a black hole. If the cluster is not concentrated enough early in its evolution, it will not reach core-collapse fast enough and a black hole will not form. As expected, they report that the presence of primordial binaries and initial mass segregation have an impact on the estimated timescales. It is interesting that the youngest object in our Satellite sample, R136, is the one that shows the steepest central profile, with a central

luminosity density slope of  $-2.11$ . We find a trend for the satellite sample in which the youngest objects have the highest central surface brightness values (i.e. central density). Our observations seem to support the possibility that star clusters are born very concentrated and evolve toward less concentrated profiles.

Evidences for the presence of black holes in star clusters can also come from radio observations. Maccarone et al. (2005) estimate the intensity of radio and X-ray emission from an intermediate mass black hole embedded in the low gas density environment of a globular cluster. They argue that it is more likely to detect radio emission than X-ray emission for this low gas density regime. The best candidates for a radio detection are rich, nearby clusters. They warn that there are considerable uncertainties regarding the level of emission from these intermediate mass black holes, but the detection of radio emission at the center of a star cluster (as long as a pulsar can be ruled out as the source) would be very strong evidence for an intermediate mass black hole. These result stresses the importance of finding dynamical evidences for the presence of IMBHs in as many clusters as possible, since this would help to find the best possible targets for extended radio observations.

### 5.3 Stability

Just like we did with  $\omega$  Centauri, kinematical measurements can be used to constrain the enclosed mass of galactic nuclei and of star clusters in small spatial scales, but the question always remains if the mass concentration is compact, in the form of a black hole, or if it is spread as a cluster of dark remnants product of mass segregation. Maoz (1998) explores the stability of a cluster of heavy non-luminous remnants like those expected to form at the



center of deep potential wells with high density of stars. The type of objects expected to be in such a cluster are stellar-mass black holes, neutron stars, faint white dwarfs, and brown dwarfs. The evaporation time is calculated for a cluster of dark remnants expected to form in a variety of galactic nuclei. The calculated times are clearly shorter than the age of the observed object for a couple of cases. In these cases a cluster of dark remnants would evaporate before core collapse can occur at the center of the galactic nucleus, therefore ruling out the possibility of the central concentration being a cluster of dark remnants. In the case of star clusters, the timescale to reach core collapse can be extended by the presence of primordial binaries, so the same phenomenon could occur. Miller (2006) adds an extra ingredient to the argument by estimating the merging time of a cluster of dark remnants in cases where core-collapse is not halted by binary heating. He finds that these timescales can be even shorter than the evaporation timescales of Maoz (1998). In summary, a cluster of dark remnants is likely to be short lived either because it evaporates quickly or because it collapses into itself forming a massive black hole. This calculations are likely out to be very useful when trying to explore the nature of central concentrations in star clusters, just in the way we have done in this work with  $\omega$  Centauri.

## 5.4 Rotation

The central region of globular clusters is not expected to show rotation because that is the location in which the relaxation processes act on the shortest timescales. Any amount of rotation is expected to be quickly erased due to relaxation. For this reason, it is very important to review the cases for which rotation has been measured in globular clusters, in order to estimate

how dominant relaxation processes are. Global rotation has been measured for a few globular clusters. In particular 47 Tuc and  $\omega$  Centauri have been subject to many detailed studies (Meylan & Mayor, 1986; Anderson & King, 2003). Xie et al. (2006) use an imaging Fabry-Perot instrument to measure line of sight velocities for individual stars in various globular clusters. They detect a rise on  $v/\sigma$  inside  $\sim 0.1 R_h$  for 8 clusters in their sample. M15 and G1 are the two globular clusters with the most detailed central kinematical observations to date. As explained in detail on the sections below (5.5.1 and 5.5.2), they appear to rotate in the central regions. These results are hinting to the fact that relaxation might not be the dominant process for the central dynamics of some globular clusters. If relaxation is not the dominant process, then something else has to be able to imprint and maintain the observed rotation in such objects.

## 5.5 Individual objects

In order to better discuss the relevance of our results for  $\omega$  Centauri, below we summarize important results by other authors on kinematic measurements for some specific globular clusters.

### 5.5.1 G1

G1 is a very massive cluster in the halo the Andromeda galaxy. It is suspect of being the stripped core of an accreted galaxy. Gebhardt et al. (2002) produce a set of axisymmetric orbit-based models from observed surface brightness and velocity profiles. They find evidence for the existence of a  $2 \times 10^4 M_\odot$  black hole at the center of the globular cluster G1. This claim is contested by Baumgardt et al. (2003c) who match the observed profiles with

two different N-body models. The first model is of a single cluster evolved from a King model that reproduces only marginally well the observed velocity dispersion. The second model comes from merging two star clusters and this is the one that is able to reproduce the observed rotation and dispersion rise in the velocity profiles. It is worth pointing out the difficulty of forming a regular relaxed star cluster like G1 from the merger of two star clusters on a galactic halo with a velocity dispersion of the order of  $200 \text{ km s}^{-1}$ . The probability of two star clusters having a relative velocity low enough to allow them to merge is extremely small. Further modeling with improved photometric and kinematic measurements is consistent with a black hole mass of  $1.7 \times 10^4 M_{\odot}$  (Gebhardt et al., 2005) and is no longer consistent with the model by Baumgardt et al. (2003c). For this latest measurements, the velocity profile for this cluster shows a clear central rotation with a projected amplitude of about  $12 \text{ km s}^{-1}$  with a central measured velocity dispersion is  $30 \text{ km s}^{-1}$ . The importance of the comparison with this cluster comes from the fact that G1 is an M31 analogue of  $\omega$  Centauri in the sense that both clusters are suspect stripped galactic nuclei and show global flattening due to rotation.

### 5.5.2 M15

M15 has long been considered to be the prototypical post core-collapse globular cluster due to the steep central cusp observed in its surface brightness profile (Sosin & King, 1997; Guhathakurta et al., 1996). However, in the last few years, there have been suggestions of it harboring a central black hole (van der Marel et al., 2002; Gerssen et al., 2002). There has been a controversial argument since then inspiring different authors to propose alternative models that do not require a black hole (Baumgardt et al., 2003b; McNamara

et al., 2003). The most recent detailed dynamical analysis is done by van den Bosch et al. (2006), who construct orbit-based models using large kinematical datasets for both line of sight radial velocities and proper motions. They measure a mass of  $3400 M_{\odot}$  inside a radius of 0.05 pc, whose nature could be a cluster of compact objects, a central black hole, or a combination of both. The formal best fit value for the black hole is  $1 \pm 1 \times 10^3$ . When analyzing a smooth version of a WFFPC2 image, they observe a degree of ellipticity in the two dimensional light distribution for the central  $\sim 4''$  ( $\sim 0.2$  pc). The velocity distribution for individual stars in that region, both in proper motion and line of sight velocity shows an apparent rotation of  $10 \text{ km s}^{-1}$ . The position angle of the rotating component coincides with that of the flattened isophotes and not with the one of global rotation observed at large radius. This apparent ‘decoupled core’ is hard to explain in a post core-collapse scenario where the evolution is dominated by relaxation processes.

### 5.5.3 NGC 6752

NGC 6752 is a Galactic globular cluster which shows peculiar indications for the existence of one or two central black holes. The millisecond pulsar (MSP) population for this cluster is very unusual compared with that of other globular clusters (D’Amico et al., 2002). Three MSPs are found in the core of the cluster, of which two show very high negative spin derivatives. The measured accelerations imply a large central M/L value of 6-7, very high for a globular cluster (Ferraro et al., 2003). This M/L value in turn implies the presence of 1000–2000  $M_{\odot}$  of under-luminous matter within the central 0.08 pc. Furthermore, there are two MSPs found in the halo of the cluster, which is an unusual location. Colpi et al. (2003) explore the effect of a single or binary

mass concentration at the center propelling one of the MSPs to the halo of the cluster on a close gravitational interaction. They conclude that a single or a binary black hole with (combined) mass of  $200 - 500 M_{\odot}$  could place the observed MSP where it is detected today and would also be consistent with the acceleration of the MSPs in the core.

## 5.6 Discussion and Summary

In chapter 2, we measure surface brightness profiles for a sample of 38 Galactic globular clusters from WFPC2 images in various filters. The profiles are obtained by measuring integrated light using the bi-weight, a robust statistical estimator. Our results show that 50% of the objects in our sample are not consistent with King profiles. These clusters show central profiles that depart from flat cores with central logarithmic slopes from  $-0.1$  to  $-0.8$ . We numerically deproject the profiles by utilizing a non-parametric smoothing procedure. The central logarithmic slopes for the luminosity density profiles show a similar distribution, with 50% of the objects having values between  $-0.5$  and  $-1.75$ .

In chapter 3, we perform the same type of measurements for a sample of 30 globular clusters orbiting the Large Magellanic cloud, the Small Magellanic cloud, and the Fornax dwarf galaxy. We find that  $\sim 45\%$  of the surface brightness profiles are inconsistent with having a central flat core, showing central logarithmic slopes from  $-0.1$  to  $-1.2$ . We find indications that younger clusters have brighter central surface brightness and smaller break radius, which seems to indicate that clusters are more concentrated when they are formed. In view of these results, the comparison of our observed slope distributions with theoretical models for globular clusters yields puzzling conclusions.

When compared with previous ground based measurements, our profiles show different shapes for the inner regions. Most central surface brightness values change from previously reported ones with values up to two magnitudes brighter. The main reason for this difference is the increased spatial resolution of *HST*, but also because we use a non-parametric estimate as opposed to the traditional King model fits. For some of the observed profiles the departures from a flat core model are small, but significant. When this profiles are deprojected, the differences become more clear. This stresses the importance of using adequate models to fit surface brightness profiles, since the effects of small deviations in surface brightness are amplified for deprojected profiles.

As discussed in chapter 1, there have been two mechanisms explored for producing cusps in star clusters: core-collapse and the presence of an intermediate mass black hole in the center of the cluster. The range of 3-dimensional density slopes is wider for core-collapse than for black hole models, but they both center around the same value,  $\sim -1.65$ . However, only the four clusters with the steepest profiles in both our samples fall in this range. In the case of core-collapse, the slope depends on the mass of the stars used to measure the profile and of those that dominate the mass of the core, so this could extend the range toward shallower slopes. Another factor of uncertainty is the time dependence of the core-collapse model when the core goes through gravothermal oscillations. According to Fokker-Planck simulations, a star cluster will spend a considerable amount of time in between successive collapses, where the light profile resembles a King model with a flat core. Unfortunately, these models do not give enough details about the slope of the density profile during intermediate stages of post-collapse bounce, or about the time spent on intermediate stages, so it is difficult to say if the slopes of our weak cusp clusters

are consistent with this picture or if we need to invoke a new mechanism to explain this shallower but non-zero slopes. As mentioned before, Dull et al. (1997) model M15 as an intermediate stage of core-collapse, while this is one of the clusters with the steepest slopes in our sample.

It is worth noting that we carefully explored the possibility of the cores not being resolved due to lack of spatial resolution. We tried to fit core models to every cluster and we only found a good fit for two cases (NGC 6397 and NGC 6652). A number of the objects with non-zero central slopes have a clear turnover radius with constant slopes inside of that. These type of profile is very hard to reproduce with post core collapse models. The result from numerical modeling for clusters containing black holes (Baumgardt et al., 2005) might be able to explain some of the intermediate slope cases as discussed in section 5.2. We find it challenging to explain these slope distributions when we compare our results to existing dynamical models for globular clusters. Core-collapse models can accommodate the cases of intermediate slopes if we catch the clusters at the appropriate time, and it seems unlikely to find them in the high fraction that we measure. Only kinematic observations can confirm the different hypotheses.

The observed correlations with age observed for the younger objects in the Satellite sample (chapter 3) point out to the possibility of clusters having very concentrated profiles during early stages of their evolution. In particular the break radius-age relation observed here and by many authors tells us that the size of cores depends on the dynamical evolution of clusters. The input density profiles for various dynamical simulations have almost always been characterized by King or Plummer models. This could be biased toward large flat cores, when more concentrated profiles could be more appropriated. This

is true for core-collapse models, as well as models containing a central black hole.

In chapter 4 we measure the central surface brightness profile for  $\omega$  Centauri from an ACS image. The central profile shows a shallow cusp with central logarithmic slope of  $-0.08$ . We also measure a line of sight velocity dispersion for a  $5'' \times 5''$  containing the center of the cluster, as well as for a field of the same size  $14''$  away from the center. We detect a rise in velocity dispersion toward the center between these two pointings from  $18.6 \text{ km s}^{-1}$  to  $23.0 \text{ km s}^{-1}$ . We combine these two measurements with a velocity dispersion profile obtained from individual radial velocities. From the deprojection of the surface brightness profile, we construct spherical models containing central black holes of various masses and compare them with the observed velocity dispersion profile. We calculate  $\chi^2$  values for each models, and the  $\chi^2$  analysis yields a central black hole with mass  $4.0_{-1.0}^{+0.75} \times 10^4 M_{\odot}$ .

The star cluster  $\omega$  Centauri has a weak cusp in the central luminosity density profile, implying that the gravitational potential is very shallow inside the core and therefore, mass segregation cannot be an important effect. Ferraro et al. (2006) confirm the lack of segregation by measuring the radial distribution of blue straggler stars, which are heavy stars and should sink to the center of the cluster if there is mass segregation. They find a flat radial distribution of blue stragglers with respect to lighter stellar populations. Also, the detailed orbit-based model by van de Ven et al. (2006) yields a very flat  $M/L$  profile for this cluster. With this evidence in hand, there is no reason to expect a large variation of  $M/L$  inside the core due to stellar content, so a detected rise in  $M/L$  is likely to come from the presence of a concentrated massive object.



The central density as measured from the  $23 \text{ km s}^{-1}$  dispersion estimate at  $1.8''$  is  $5.6 \times 10^7 M_{\odot}/pc^3$ . This is the largest measured for a globular cluster and it would be difficult to maintain using stellar remnants. Obviously, if the density is due to solar mass remnants, over  $10^4$  remnants would be required inside of 0.05 parsecs. Using the arguments of Maoz (1998) and Miller (2006), this mass and density makes  $\omega$  Centauri one of the better examples where stellar remnants can be ruled out due to evaporation. Maoz estimates that for these numbers, any cluster of remnants will have evaporated within  $10^{10}$  years.

These results put together with the observed rotation at the center of some clusters and the unusual MSP population for NGC 6752 leads to the idea that relaxation is not the only process taking place at the center of globular clusters. Other effects must be taking place there, and only systematic detailed measurements of a large number of clusters will be able to unveil the dominant processes. Black holes could be responsible for some of the observations, but if they turn out not to be detected in many clusters, detailed dynamical models and observations are necessary to unveil the underlying causes. If black holes do happen to be present at the center of many clusters, and not only in the suspect stripped galaxy cores, it is crucial to investigate the demographics of the population. On one hand they could be important ingredients for the formation of supermassive black holes at the center of galaxies. On the other hand, they could turn out to be numerous sources for gravitational wave detectors.

## Bibliography

- Ambartsumian, V. 1938, *Ann. Leningrad State Univ.*, 22, 119
- Anderson, J., & King, I. R. 2003, *AJ*, 126, 772
- Bahcall, J. N., & Wolf, R. A. 1976, *ApJ*, 209, 214
- Bahcall, J. N., & Wolf, R. A. 1977, *ApJ*, 216, 883
- Barth, A. J., Greene, J. E., & Ho, L. C. 2005, *ApJL*, 619, L151
- Bates, D., Lindstrom, M., Wahba, G., & Yandell, B. 1986, Technical Report 775, University of Wisconsin, Madison
- Baumgardt, H., Heggie, D. C., Hut, P., & Makino, J. 2003a, *MNRAS*, 341, 247
- Baumgardt, H., Hut, P., Makino, J., McMillan, S., & Portegies Zwart, S. 2003b, *ApJL*, 582, L21
- Baumgardt, H., Makino, J., & Ebisuzaki, T. 2004, *ApJL*, submitted
- Baumgardt, H., Makino, J., & Hut, P. 2005, *ApJ*, 620, 238
- Baumgardt, H., Makino, J., Hut, P., McMillan, S., & Portegies Zwart, S. 2003c, *ApJL*, 589, L25
- Bedin, L. R., Piotto, G., Anderson, J., Cassisi, S., King, I. R., Momany, Y., & Carraro, G. 2004, *ApJL*, 605, L125
- Beers, T. C., Flynn, K., & Gebhardt, K. 1990, *AJ*, 100, 32
- Bekki, K., & Freeman, K. C. 2003, *MNRAS*, 346, L11
- Binney, J., & Tremaine, S. 1987, *Galactic dynamics* (Princeton, NJ, Princeton University Press, 1987, 747 p.)

- Breedem, J. L., Cohn, H. N., & Hut, P. 1994, *ApJ*, 421, 195
- Chandrasekhar, S. 1942, *Physical Sciences Data*
- Chernoff, D. F., & Weinberg, M. D. 1990, *ApJ*, 351, 121
- Cohn, H. 1980, *ApJ*, 242, 765
- Cohn, H. 1985, in *IAU Symposium*, ed. J. Goodman & P. Hut, 161
- Cohn, H., Hut, P., & Wise, M. 1989, *ApJ*, 342, 814
- Colpi, M., Mapelli, M., & Possenti, A. 2003, *ApJ*, 599, 1260
- D'Amico, N., Possenti, A., Fici, L., Manchester, R. N., Lyne, A. G., Camilo, F., & Sarkissian, J. 2002, *ApJ*, 570, L89
- De Angeli, F., Piotto, G., Cassisi, S., Busso, G., Recio-Blanco, A., Salaris, M., Aparicio, A., & Rosenberg, A. 2005, *AJ*, 130, 116
- de Grijs, R., Gilmore, G. F., Mackey, A. D., Wilkinson, M. I., Beaulieu, S. F., Johnson, R. A., & Santiago, B. X. 2002, *MNRAS*, 337, 597
- Dickens, R. J., & Woolley, R. v. d. R. 1967, *Royal Greenwich Observatory Bulletin*, 128, 255
- Dinescu, D. I., Majewski, S. R., & Girard, K. M., T. M. and Cudworth. 2001, *AJ*, 122, 1916
- Djorgovski, S. 1995, *ApJL*, 438, L29
- Djorgovski, S., & King, I. R. 1986, *ApJL*, 305, L61
- Drukier, G. A. 1995, *ApJS*, 100, 347
- Drukier, G. A., Fahlman, G. G., & Richer, H. B. 1992, *ApJ*, 386, 106
- Dubath, P., Meylan, G., & Mayor, M. 1997, *AAP*, 324, 505
- Dull, J. D., Cohn, H. N., Lugger, P. M., Murphy, B. W., Seitzer, P. O., Callanan, P. J., Rutten, R. G. M., & Charles, P. A. 1997, *ApJ*, 481, 267

- Eddington, A. S. 1916, MNRAS, 76, 572
- Elson, R. A. W. 1991, ApJS, 76, 185
- Elson, R. A. W. 1992, MNRAS, 256, 515
- Elson, R. A. W., Fall, S. M., & Freeman, K. C. 1987, ApJ, 323, 54
- Elson, R. A. W., Freeman, K. C., & Lauer, T. R. 1989, ApJL, 347, L69
- Ferrarese, L., & Merritt, D. 2000, ApJL, 539, L9
- Ferraro, F. R., Possenti, A., Sabbi, E., Lagani, P., Rood, R. T., D'Amico, N., & Origlia, L. 2003, ApJ, 595, 179
- Ferraro, F. R., Sollima, A., Rood, R. T., Origlia, L., Pancino, E., & Bellazzini, M. 2006, ApJ, 638, 433
- Freeman, K. C. 1993, in ASP Conf. Ser. 48: The Globular Cluster-Galaxy Connection, 608
- Fukushige, T., & Heggie, D. C. 1995, MNRAS, 276, 206
- Gao, B., Goodman, J., Cohn, H., & Murphy, B. 1991, ApJ, 370, 567
- Gebhardt, K., & Fischer, P. 1995, AJ, 109, 209
- Gebhardt, K., Pryor, C., O'Connell, R. D., Williams, T. B., & Hesser, J. E. 2000a, AJ, 119, 1268
- Gebhardt, K., Rich, R. M., & Ho, L. C. 2002, ApJ, 578, L41
- Gebhardt, K., Rich, R. M., & Ho, L. C. 2005, ApJ, 634, 1093
- Gebhardt, K., et al. 1996, AJ, 112, 105
- Gebhardt, K., et al. 2000b, AJ, 119, 1157
- Gerssen, J., van der Marel, R. P., Gebhardt, K., Guhathakurta, P., Peterson, R. C., & Pryor, C. 2002, AJ, 124, 3270

- Gerssen, J., van der Marel, R. P., Gebhardt, K., Guhathakurta, P., Peterson, R. C., & Pryor, C. 2003, *AJ*, 125, 376
- Gnedin, O. Y., Lee, H. M., & Ostriker, J. P. 1999, *ApJ*, 522, 935
- Grillmair, C. J., Freeman, K. C., Irwin, M., & Quinn, P. J. 1995, *AJ*, 109, 2553
- Guhathakurta, P., Webster, Z. T., Yanny, B., Schneider, D. P., & Bahcall, J. N. 1998, *AJ*, 116, 1757
- Guhathakurta, P., Yanny, B., Schneider, D. P., & Bahcall, J. N. 1996, *AJ*, 111, 267
- Gürkan, M. A., Freitag, M., & Rasio, F. A. 2004, *ApJ*, 604, 632
- Harris, W. E. 1996, *AJ*, 112, 1487
- Heggie, D. C. 1979, *mnras*, 188, 525
- Hénon, M. 1964, *Annales d'Astrophysique*, 27, 83
- Herschel, W. 1814, *Philosophical Transactions Series I*, 104, 248
- Howell, J. H., Guhathakurta, P., & Tan, A. 2000, *AJ*, 119, 1259
- Icke, V., & Alcaïno, G. 1988, *AAP*, 204, 115
- Ikuta, C., & Arimoto, N. 2000, *AAP*, 358, 535
- Jeans, J. H. 1913, *MNRAS*, 74, 109
- Jimenez, R., & Padoan, P. 1998, *ApJ*, 498, 704
- Kawakatu, N., & Umemura, M. 2004, *ApJ*, 601, L21
- King, I. R. 1966, *AJ*, 71, 276
- King, I. R., Sosin, C., & Cool, A. M. 1995, *ApJL*, 452, L33
- Kontizas, E., & Kontizas, M. 1983, *AAP*, 52, 143

Kontizas, M., Chrysovergis, M., & Kontizas, E. 1987, AAP, 68, 147

Kontizas, M., Theodossiou, E., & Kontizas, E. 1986, AAP, 65, 207

Lauer, T. R., et al. 1995, AJ, 110, 2622

Lauer, T. R., et al. 2002, AJ, 124, 1975

Lauer, T. R., et al. 1991, ApJL, 369, L45

Lin, D. N. C., & Tremaine, S. 1980, ApJ, 242, 789

Lugger, P. M., Cohn, H. N., & Grindlay, J. E. 1995, ApJ, 439, 191

Lynden-Bell, D. 1962, MNRAS, 124, 279

Maccarone, T. J., Fender, R. P., & Tzioumis, A. K. 2005, Ap&SS, 300, 239

Mackey, A. D., & Gilmore, G. F. 2003a, MNRAS, 338, 120

Mackey, A. D., & Gilmore, G. F. 2003b, MNRAS, 338, 85

Mackey, A. D., & Gilmore, G. F. 2003c, MNRAS, 340, 175

Makino, J. 1996, ApJ, 471, 796

Maoz, E. 1998, ApJ, 494, L181

Massey, P., & Hunter, D. A. 1998, ApJ, 493, 180

Mateo, M. 1987, ApJL, 323, L41

Matsumoto, H., & Tsuru, T. G. 1999, PASJ, 51, 321

Matsumoto, H., Tsuru, T. G., Koyama, K., Awaki, H., Canizares, C. R.,  
Kawai, N., Matsushita, S., & Kawabe, R. 2001, ApJ, 547, L25

Mayor, M., et al. 1997, AJ, 114, 1087

McCraday, N., Gilbert, A. M., & Graham, J. R. 2003, ApJ, 596, 240

McLaughlin, D. E., & van der Marel, R. P. 2005, ApJS, 161, 304

- McNamara, B. J., Harrison, T. E., & Anderson, J. 2003, *ApJ*, 595, 187
- Merritt, D., Meylan, G., & Mayor, M. 1997, *AJ*, 114, 1074
- Messier. 1784, *Connaissance des Temps*, 1784, 227
- Meylan, G. 1987, *AAP*, 184, 144
- Meylan, G., & Heggie, D. C. 1997, *AAP*, 8, 1
- Meylan, G., & Mayor, M. 1986, *A&A*, 166, 122
- Meylan, G., Mayor, M., Duquennoy, A., & Dubath, P. 1995, *AAP*, 303, 761
- Meza, A., Navarro, J. F., Abadi, M. G., & Steinmetz, M. 2005, *MNRAS*, 359, 93
- Miller, M. C. 2006, *MNRAS*, 367, L32
- Miller, M. C., & Hamilton, D. P. 2002, *MNRAS*, 330, 232
- Mouri, H., & Taniguchi, Y. 2002, *ApJ*, 566, L17
- Murphy, B. W., & Cohn, H. N. 1988, *MNRAS*, 232, 835
- Murphy, B. W., Cohn, H. N., & Hut, P. 1990, *MNRAS*, 245, 335
- Norris, J. E., Freeman, K. C., Mayor, M., & Seitzer, P. 1997, *ApJL*, 487, L187
- Norris, J. E., Freeman, K. C., & Mighell, K. J. 1996, *ApJ*, 462, 241
- Noyola, E., & Gebhardt, K. 2006, *AJ*, 132, 447
- Oort, J. H., & van Herk, G. 1959, *Bull. Astron. Inst. Netherlands*, 14, 299
- Pancino, E., Seleznev, A., Ferraro, F. R., Bellazzini, M., & Piotto, G. 2003, *MNRAS*, 345, 683
- Pickering, E. C., Bailey, S. I., Fleming, W. P., Leland, E. F., & Wells, L. D. 1898, *ApJ*, 7, 208
- Pinkney, J., et al. 2003, *ApJ*, 596, 903

- Piotto, G., et al. 2002, AAP, 391, 945
- Portegies Zwart, S. F., Baumgardt, H., Hut, P., Makino, J., & McMillan, S. L. W. 2004, Nature, 428, 724
- Reijns, R. A., Seitzer, P., Arnold, R., Freeman, K. C., Ingerson, T., van den Bosch, R. C. E., van de Ven, G., & de Zeeuw, P. T. 2006, AAP, 445, 503
- Rodgers, A. W., & Roberts, W. H. 1994, AJ, 107, 1737
- Salaris, M., & Weiss, A. 2002, AAP, 388, 492
- Searle, L., & Zinn, R. 1978, ApJ, 225, 357
- Shapiro, S. L. 1977, ApJ, 217, 281
- Silk, J., & Arons, J. 1975, ApJL, 200, L131
- Smith, E. O., Neill, J. D., Mighell, K. J., & Rich, R. M. 1996, AJ, 111, 1596
- Sosin, C. 1997, AJ, 114, 1517
- Sosin, C., & King, I. R. 1997, AJ, 113, 1328
- Spitzer, L. 1987, Dynamical evolution of globular clusters (Princeton, NJ, Princeton University Press, 1987, 191 p.)
- Spitzer, L. J. 1940, MNRAS, 100, 396
- Stetson, P. B. 1987, PASP, 99, 191
- Strohmayer, T. E., & Mushotzky, R. F. 2003, ApJ, 586, L61
- Suntzeff, N. B., & Kraft, R. P. 1996, AJ, 111, 1913
- Trager, S. C., King, I. R., & Djorgovski, S. 1995, AJ, 109, 218
- Tremaine, S., et al. 2002, ApJ, 574, 740
- van de Ven, G., van den Bosch, R. C. E., Verolme, E. K., & de Zeeuw, P. T. 2006, AAP, 445, 513



- van den Bosch, R., de Zeeuw, T., Gebhardt, K., Noyola, E., & van de Ven, G. 2006, ApJ, 641, 852
- van der Marel, R. P., Gerssen, J., Guhathakurta, P., Peterson, R. C., & Gebhardt, K. 2002, AJ, 124, 3255
- van Leeuwen, F., Le Poole, R. S., Reijns, R. A., Freeman, K. C., & de Zeeuw, P. T. 2000, AAP, 360, 472
- von Hoerner, S. 1960, Zeitschrift fur Astrophysik, 50, 184
- Wahba, G. 1980, Technical Report 595, University of Wisconsin, Madison
- Wahba, G., & Wang, Y. 1990, Communications in Statistics, Part A – Theory and Methods, 19, 1685
- Walcher, C. J., et al. 2005, ApJ, 618, 237
- White, R. E., & Shawl, S. J. 1987, ApJ, 317, 246
- Wilson, C. P. 1975, AJ, 80, 175
- Xie, B., Gebhardt, K., Pryor, C., & Williams, T. B. 2006, in prep
- Yanny, B., Guhathakurta, P., Schneider, D. P., & Bahcall, J. N. 1994, ApJL, 435, L59
- Yuan, Z., & Zhong, X. G. 1990, Ap&SS, 168, 233

## Vita

Eva Noyola was born in México City, México on 23 July 1975, the daughter of Antonio Noyola Rocha and Martha Loya Sepúlveda. She received a Physics degree from the Universidad Nacional Autónoma de México. She applied to the University of Texas at Austin for enrollment in their astronomy program. She was accepted and started graduate studies in August, 2000.

Permanent address: 5005 Martin Ave  
Austin, Tx, 78751

This dissertation was typeset with  $\text{\LaTeX}^\dagger$  by the author.

---

<sup>†</sup> $\text{\LaTeX}$  is a document preparation system developed by Leslie Lamport as a special version of Donald Knuth's  $\text{\TeX}$  Program.